



Università degli Studi Roma Tre

Dipartimento di Matematica e Fisica
Doctoral program in Physics – XXXIV cycle

A thesis presented for the degree of
Doctor of Philosophy in Physics

RECONCILING WEAK AND STRONG FIELD
REGIMES THROUGH SPACE MISSIONS

Author:

Lorenza Mauro

Supervisors:

Prof. Salvatore Capozziello

Prof. Wolfango Plastino

Doctoral Program Coordinator:

Prof. Giuseppe Degrassi

A.A. 2021/2022

List of publications and works

This thesis is mainly based on the results of the following research papers and works

1. S. Capozziello, O. Luongo, L. Mauro, *Traversable wormholes with vanishing sound speed in $f(R)$ gravity*, Eur. Phys. J. Plus **136**, 167 (2021).
2. R. Giambò, O. Luongo, L. Mauro, *Red and blue shift in spherical and axisymmetric spacetimes and astrophysical constraints*, Eur. Phys. J. Plus **137**, 612 (2022).
3. J. G. Williams, L. Porcelli, S. Dell’Agnello, L. Mauro, M. Muccino, D. G. Currie, D. Wellnitz, C. Wu, D. Boggs, N. H. Johnson, *Lunar Laser Ranging: Velocity Aberration and Diffraction Pattern*, in prep.
4. Calculation of the equations of motion in alternative theories of gravity.
5. Calculation of the Lense-Thirring precession in alternative theories of gravity.
6. Optical simulations of laser retroreflectors with Code V.
7. Laser Ranging data processing with Planetary Ephemeris Program.

Abstract

The main goal of this thesis is to test gravity theories through space missions in order to contribute to the discovery of the most reliable and consistent ones. The work is divided into two sections: the first analyzes theoretical models that will be examined for astrophysical and cosmological reasons; and the second explores experimental methods.

As starting point, the first results obtained with the so-called classical General Relativity tests are investigated. They established the theory's validity in the Solar System. However, recent discoveries on larger dimensions and in distinct gravitational regimes need the construction of new theoretical models. As a result, the Parametrized Post-Newtonian formalism is examined in detail. Indeed, it enables comparisons of General Relativity with alternative metric theories of gravity in the weak field regime. Limits on the Post-Newtonian parameters are then illustrated using data from the Laser Ranging missions. Due to the limitations of this formalism in stronger gravitational fields and on energy domains other than the Solar System, two more theoretical models are studied. The first step is to determine the blue and redshifts for metrics with particular symmetries, such as spherical and axial. In three different gravity regimes, low, intermediate and high, the findings of the Zipoy-Voorhees and Schwarzschild-de Sitter metrics are shown. The theoretical results obtained in the low gravity regime are compared to those predicted by the aforementioned Laser Ranging, as well as a hypothetical mission to Mars' satellite Phobos. Instead, in the other two regimes, the comparison is done by looking at the properties of a neutron star and a white dwarf. The strong field is the topic of the second theoretical model: a class of wormhole solutions in extended theories of gravity.

The second section of the thesis work examines the experimental setup of space missions that were used to constrain the free parameters of the previously described theories. LARES-2 and MoonLIGHT Laser Ranging exper-

iments are described in detail, with an emphasis on their optical characteristics. Then, plots from optical simulations of the laser retroreflectors used in these two missions are shown. This provides an overview of why and how new theories of gravity should be tested.

Contents

Introduction	6
1 Low gravity tests	10
1.1 The four classical tests of General Relativity	11
1.1.1 Perihelion precession of Mercury	11
1.1.2 Deflection of light by the Sun	17
1.1.3 Gravitational redshift of light	21
1.1.4 Shapiro time delay	24
1.2 The Parametrized Post-Newtonian formalism	28
1.2.1 Newtonian approximation	30
1.2.2 Post-Newtonian approximation	31
1.2.3 Post-Newtonian stress-energy tensor	36
1.3 PPN parameters in metric theories of gravity	37
1.3.1 Metric theories of gravity	39
1.3.2 Horndeski's theory	41
1.3.3 Vector Tensor theory	49
1.3.4 Final remarks	52
1.4 Equations of motion in the PPN formalism	52
1.4.1 Final remarks	63
1.5 The frame dragging	63
2 Astrophysical constraints of low and high gravity tests	67
2.1 The photon red and blue shift	68
2.1.1 Non rotating spacetime	73
2.2 Spacetime solutions	74
2.2.1 The Zipoy-Voorhees metric	74
2.2.2 Gravitational field sources for the Zipoy-Voorhees metric	78
2.2.3 The Schwarzschild-de Sitter metric	79

2.2.4	Gravitational field sources for the Schwarzschild-de Sitter metric	81
2.3	Results	82
2.3.1	High and intermediate gravity regimes	83
2.3.2	Regime of low gravity	89
2.3.3	Error analysis	98
2.3.4	Results for the Schwarzschild spacetime	100
3	High gravity tests	102
3.1	Wormholes solutions of Einstein's equations	102
3.1.1	$f(R)$ wormholes with rational shape reconstructions . .	104
3.1.2	The stability condition and the sound speed	113
3.1.3	The wormhole solutions	114
3.2	Theoretical considerations	117
3.2.1	Final remarks	118
4	Experimental tests of gravity	119
4.1	The Laser Ranging	120
4.2	Cube Corner Retroreflectors	122
4.3	Optical simulations with Code V	126
4.3.1	LARES-2	128
4.3.2	MoonLIGHT	134
4.4	Planetary Ephemeris Program	139
4.4.1	Installation and Big Test	139
4.4.2	PEP operational method	139
4.4.3	Results	141
	Conclusions	143
	Bibliography	147

Introduction

General Relativity (GR) is the most well-known theory of gravitational interaction. Einstein's theory, published in 1915 [1, 2], provided the best description of space, time and gravity so far. The main hypotheses of GR fully match experimental data, as shown from several gravitational phenomena. The so-called "three classical tests of GR", proposed by Einstein, certify the goodness of GR. He demonstrated how the theory could predict the $43''/\text{cy}$ observed by Le Verrier in Mercury's orbit precession but not explained by Newtonian theory. Another notable achievement of GR was the estimation of the light deflection by the Sun, which was confirmed by Eddington's measurement during the historic 1919 total eclipse [3]. Finally, Einstein's hypothesis of gravitational redshift was validated by tests conducted between 1959 and 1965 by Pound, Rebka, and Snider [4, 5, 6].

Even though these tests represented the beginning of a series of experimental triumphs of GR, in 1964, Shapiro determined the time delay that happens when a radar signal passes near a massive object. He discovered that a radar signal sent from Earth to a planet or a satellite travelling close to the Sun experiences a non-Newtonian delay in its round-trip travel time [7, 8]. The Shapiro time delay is also known as "the fourth classical test of GR". Other tests of GR's validity are ongoing or have been revealed recently. LIGO (Laser Interferometer Gravitational - wave Observatory) - VIRGO collaboration [9] was able to observe the gravitational waves of a binary black hole system merging to form a single black hole, one hundred years after Einstein's field equations and Schwarzschild's solution were published. Indeed, technological advancements have enabled scientists to conduct increasingly in-depth studies of the cosmos over the time. For instance, observations from Supernovae Ia (SNe Ia) [10], Cosmic Microwave Background radiation (CMB) [11, 12, 13], Large Scale Structure (LSS) [14], Baryon Acoustic Oscillations (BAO) [15] and weak lensing [16] provide information about the universe's

dynamics as well as its kinematics. Indeed, they suggest that small perturbations occurred in the early universe, and that the famous Friedmann Robertson Walker (FRW) metric perturbations formed cosmic structures; they also show an accelerated expanding universe, and with a flat spatial curvature. The only method to account for cosmic acceleration in the framework of GR is to modify the matter component of Einstein's field equations. This approach leads to Dark Energy (DE), which is an unclustered fluid with negative pressure. There are numerous ways to address the DE: one of them is to reintroduce the cosmological constant Λ ¹, as in the concordance Λ Cold Dark Matter (Λ CDM) model. There is, however, a discrepancy of about 120 orders of magnitude between the predicted value and the observational limits [17], since Λ is generally associated with the energy of the vacuum in quantum field theory (*fine-tuning problem*). Additionally, it is not clear why its current value is comparable to the matter density (*coincidence problem*). Then other models, such as those incorporating scalar fields, were proposed. The cosmological constant is treated as a fluid with a constant equation of state, i.e. $p_\Lambda = -\rho_\Lambda$. This is consistent with the Plank collaboration's data [18], assuming no temporal evolution throughout cosmic time. Nevertheless, if we want to relax this last hypothesis, we must use a different description that results in a time-varying equation of state, thus the scalar fields. Again, numerous examples exist, including quintessence, phantoms, K-essence, tachyon, ghost condensates and dilatonic dark energy [19]. Despite its success in fitting cosmic data, this approach to DE suffers from the coincidence problem, because DE and matter densities reach comparable values only for a brief period in the universe's history, corresponding with the present epoch. Finally, observational evidence for the Big Bang indicates a primordial cosmos characterized by high energy scales. Increase of gravitational energy could require the existence of a quantum theory of gravity [20, 21, 22]. But no conclusive approaches to quantum gravity exist yet, challenging the standard puzzle of unifying fundamental forces into a single scheme [23, 24, 25, 26]. Consequently, despite Einstein's famous remark "*feel sorry for the dear Lord, for the theory is correct!*", these experimental results today raise questions about the theoretical model that could best describe them. In other words, is general relativity the only theory that adequately accounts for gravitational interactions? Extensions and modifica-

¹Initially proposed by Einstein himself to describe a static universe and then eliminated after the discovery of Hubble, calling the constant his "biggest blunder".

tions of the Hilbert Einstein action may provide an answer to this question, allowing for the treatment of these observed phenomena as curvature effects [27, 28, 29, 30]. Probably the most well-known models of this approach are those that extend GR including higher order terms in curvature invariants (such as R^2 , $R^{\mu\nu}R_{\mu\nu}$, $R^{\mu\nu\alpha\beta}R_{\mu\nu\alpha\beta}$, $R\Box R$, $R\Box^k R$), generic functions of the Ricci scalar (e.g., $f(R)$), minimal or non-minimal couplings between scalar fields and geometry (such as $\phi^2 R$). For example, these *Extended Theories of Gravity* (ETGs) enable us to explain the accelerated expansion of the universe without considering DE and to justify the flatness of galaxies rotation curves without introducing Dark Matter (DM) [31]. We refer to *metric theories of gravity* (such as GR) when matter and other non-gravitational fields are coupled only to the metric, and they satisfy the Equivalence Principle by construction. In other words, the connection is metric compatible. But there are no theoretical reasons why connection and metric should not be independent variables. Palatini was the first to formulate this hypothesis, hence the name of the formalism [32]. By relaxing the torsionless and metric compatible connection hypotheses, which are both GR features, another class of theories is constructed. In *Einstein Cartan's theory*, the antisymmetric part of the $\Gamma^\alpha_{\mu\nu}$ connection is different from zero; on the other hand, in the *Teleparallel Equivalent to General Relativity* (TEGR) formalism, spacetime is characterized exclusively by the torsion T , while the curvature is zero, and the connection is that of Weitzenböck. However, we should specify that the teleparallel field equations are completely equivalent to Einstein's equations. This means that they are incapable of solving the cosmological and astrophysical issues discussed above unless a generic function of the torsion T is considered in the action, as is the case of the metric ETGs. The advantage of employing $f(T)$ rather than $f(R)$ is that the equations are of second order in the former and fourth order in the latter. These are undoubtedly only a few examples of theories that go beyond Einstein's theory. In any case, whatever the theory, to be correct, it must be *self-consistent*, *complete* and *in agreement with past experiment* [33]. To be precise, the theory must work well at all scales, at low and high energies, from quantum to cosmological, and, in terms of the gravitational field, in the weak and strong field regime; it must also reproduce Newtonian dynamics, pass the classical Solar System tests, and account for astrophysical and cosmological observations, from the Big Bang to the present (Fig.1). Thus, probing gravity theories with arbitrary accuracy at both short and long distances seems reasonable for ensuring their validity across a range of energy scales. Since the launch

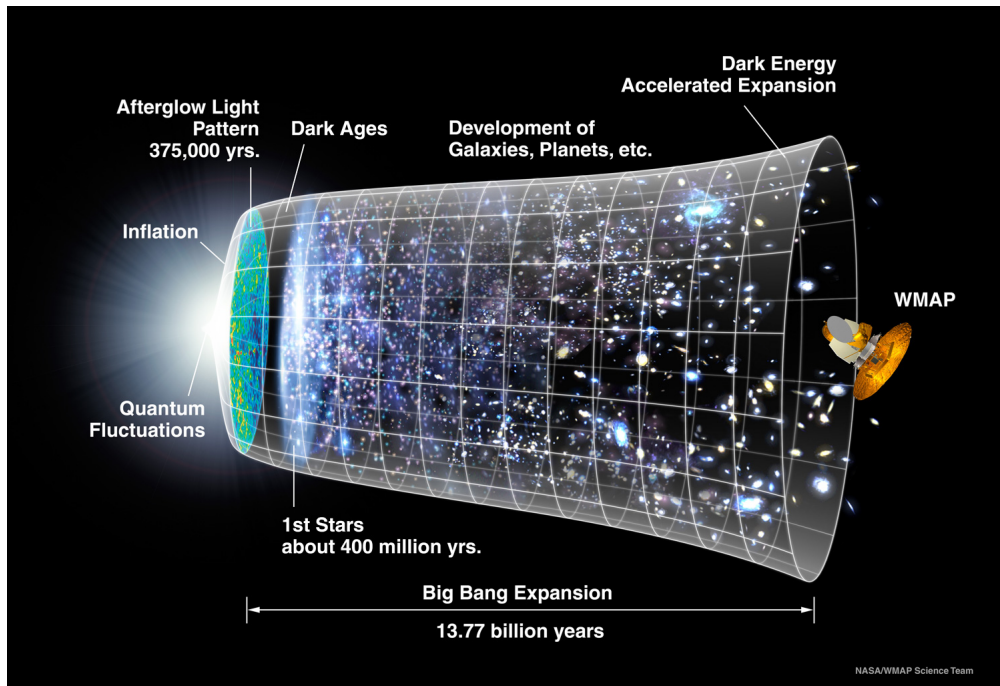


Figure 1: *Evolution diagram of the observable universe, from the Big Bang to the present. Credits: NASA/WMAP Science Team.*

of the first man into space (Russian astronaut Gagarin) 60 years ago, exploration of the universe has pushed the boundaries of deep space, reaching realms of the universe previously unimaginable. Lunar missions *Apollo* and *Lunokhod*, satellites *LARES* and *LAGEOS*, *Planck* spacecraft, Mars missions *InSight* and *Mars2020* represent only a small fraction of the space missions conducted during the last several years.

Throughout the text, we use units such that $c = G = 1$, unless differently specified.

Chapter 1

Low gravity tests

Reconciling high and low gravitational energy scales is one of the outstanding issues in modern physics. To achieve this ambitious goal, the first step is to determine the appropriate framework that will help to compare theoretical model with experimental data. We take into account the fact that the characteristics of the gravitational field change according to the energy scale. This translates into a different mathematical treatment: whereas in the weak field we can perform series developments, neglecting some terms due to their extremely low values, this is not allowed in the strong field, where all contributions must be included. This means that analyzing models in the Solar System is easier than, say, in the neighborhood of a black hole. Of course, the difficulty of the calculation also depends on the symmetries of the metric which describes the spacetime generated by the gravitational object under investigation. Theoretical model must accurately reproduce observations, not just in the simplest way feasible. In fact, too many simplifications may result in a theoretical model that does not match the real item. Once the theoretical background has been determined, we use experimental data from space missions to determine the value of the free parameters of the theory we would like to test.

The chapter is organized as follows. We begin by reviewing the classical Solar System tests of GR. Next, we introduce the Parametrized Post-Newtonian (PPN) formalism, which is ideal for describing the weak gravitational field, and then examine several alternative theories of gravity. Finally, we analyze the frame-dragging effect, a physical phenomenon predicted by Einstein's theory and extensively investigated in the Solar System via the Laser Ranging (LR) technique.

1.1 The four classical tests of General Relativity

The perihelion precession of Mercury, the deflection of light by the Sun, and the gravitational redshift of light represent the first evidence of the validity of Einstein’s theory of gravity. These are complemented by Shapiro’s calculation of the light travel time delay, and together they constitute the so-called “four classical tests” of GR. The theoretical formulation is presented in this section.

1.1.1 Perihelion precession of Mercury

When we consider an isolated two-body system in which one orbits around the other in Newtonian theory, the orbiting body follows an elliptical trajectory, whose focus is occupied by the system’s center of mass. The major axis is fixed in space, which means that the periapsis (the point of closest approach to the focus) is also fixed. However, due to the interaction with all of the other entities in the Solar System, Newtonian theory applied to the study of the motion of the planets around the Sun predicts a precession of the perihelion, that is, a rotation of the major axis around the center of mass, for each planet. In 1859, Le Verrier was the first to observe this physical phenomenon [34]. He measured the precession of Mercury’s perihelion, the planet closest to the Sun, finding a value that disagreed from the Newtonian prediction of $43''/\text{cy}$. Several solutions were proposed to explain this discrepancy. Le Verrier himself hypothesized the presence of another planet, Vulcan. Only Einstein, with the publication of GR theory, was able to definitively demonstrate the precession of Mercury’s perihelion [35]. To analyze Einstein’s result, we now look at the geodesics of massive particles in the Sun’s gravitational field described by the Schwarzschild metric [36]

$$ds^2 = - \left(1 - \frac{2M}{r}\right) dt^2 + \left(1 - \frac{2M}{r}\right)^{-1} dr^2 + r^2 d\Omega^2, \quad (1.1)$$

where $d\Omega^2 = d\theta^2 + \sin^2\theta d\varphi^2$. Let us denote by

$$\{u^\mu\} = \left\{ \frac{dt}{d\lambda}, \frac{dr}{d\lambda}, 0, \frac{d\varphi}{d\lambda} \right\}, \quad (1.2)$$

with λ the affine parameter, the four-velocity (or the tangent to the affinely parameterized geodesics) of a massive particle which travels in the equatorial plane (i.e. $\theta = \pi/2$). It satisfies the normalization condition

$$u^2 = -1. \quad (1.3)$$

This is a constant of motion; it does not depend on any symmetry of the metric (1.1) but it is a general property, related only to the geodesics affine parameterization. Specifically, Eq. (1.3) is

$$-\left(1 - \frac{2M}{r}\right) \dot{t}^2 + \left(1 - \frac{2M}{r}\right)^{-1} \dot{r}^2 + r^2 \dot{\varphi}^2 = -1, \quad (1.4)$$

where we used the dot to indicate the derivative with respect to λ .

On the other hand, the symmetries of the metric enable us to determine two additional constant of motion. Indeed, there are two Killing fields, $\partial/\partial t$ and $\partial/\partial\varphi$, because the coordinate components of the metric do not depend on t and φ . In general, given a Killing field ξ^μ and an affine parametrized geodesic, the scalar product $g_{\mu\nu}u^\mu\xi^\nu$ is constant along the geodesic itself. Therefore, in our case, we have

$$g_{\mu\nu}u^\mu \left(\frac{\partial}{\partial t}\right)^\nu = -\left(1 - \frac{2M}{r}\right) \dot{t} \doteq -E, \quad (1.5)$$

$$g_{\mu\nu}u^\mu \left(\frac{\partial}{\partial\varphi}\right)^\nu = r^2 \dot{\varphi} \doteq L. \quad (1.6)$$

By exploiting these two constants of motion, named E and L , into Eq. (1.4), we get

$$\dot{r}^2 + \left(1 - \frac{2M}{r}\right) \frac{L^2}{r^2} + \left(1 - \frac{2M}{r}\right) = \frac{E^2}{r^2}, \quad (1.7)$$

which determines the radial motion. If we divide all terms by a factor 2, we can rewrite Eq. (1.7) as the expression for the energy of a particle moving in a central field

$$\frac{1}{2} \dot{r}^2 + V_{\text{eff}}(r) = \frac{E^2}{2}, \quad (1.8)$$

where

$$\begin{aligned} V_{\text{eff}}(r) &= \frac{1}{2} \left(1 - \frac{2M}{r}\right) \left(\frac{L^2}{r^2} + 1\right) = \\ &= -\frac{M}{r} + \frac{L^2}{2r^2} - \frac{ML^2}{r^3} + \frac{1}{2}. \end{aligned} \quad (1.9)$$

Formally, Eq. (1.8) is the same as the classical one but the effective potential has additional terms. As a matter of fact, the first two terms in Eq. (1.9) are analogous to those contained in Newton's theory. In particular, $-M/r$ is the classical gravitational potential generated by a body of mass M ; while L^2/r^2 represents the centrifugal barrier, which occurs when the particle has a non-zero angular momentum. Instead, the last term in Eq. (1.9) is a constant and therefore has no physical meaning; the third is the relativistic correction. Let us see how this potential varies as a function of the radial coordinate r . First of all we observe that it depends on the value of the angular momentum L . For this reason, we have two plots for V_{eff} , Fig. 1.1. Let us first analyze the case A, Fig. (1.1a). The potential is monotone, it vanishes in $r = r_s$ and it tends to $1/2$ at infinity. What kind of motions does V_{eff} describe? Depending on the value assumed by $E^2/2$, there are four possibilities.

For $E^2/2 > 1/2$

1. if $\dot{r} > 0$, the particle moves indefinitely away without going back (this is the case of a particle that, ejected from the Sun, travels towards the infinity);
2. if $\dot{r} < 0$, the particle moves towards the center of the gravitational field and falls into the origin of the coordinate system (this is the case of a particle that comes from infinity and collapse on the Sun).

On the contrary, for $E^2/2 < 1/2$

1. if $\dot{r} > 0$, the particle first moves away from the center of mass, reaches a point where the motion reverses and then falls to the origin (this is the case of a particle ejected from the Sun with a speed too low to escape towards the infinity, so it reaches a maximum distance and then falls again on the Sun);
2. if $\dot{r} < 0$, the particle proceeds directly towards the origin of the coordinate system (this is the case of a particle that falls on the Sun).

From this analysis we understand that none of these motions describe that of a planet. Let us now examine the case B, Fig. (1.1b).

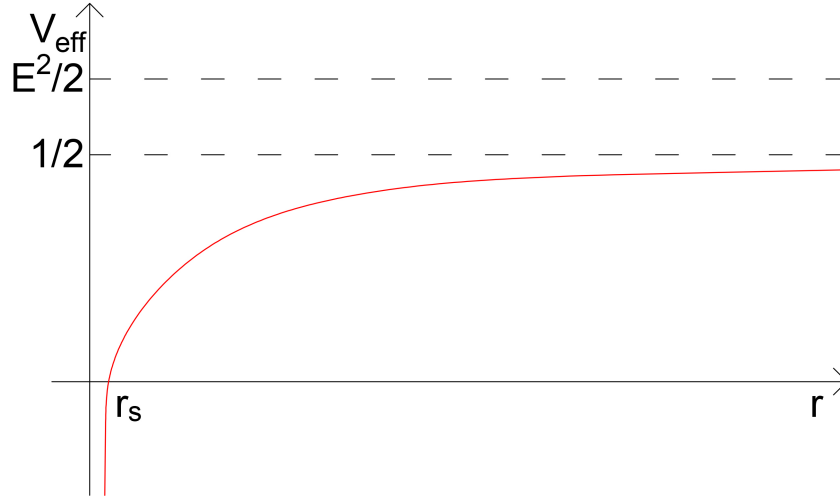
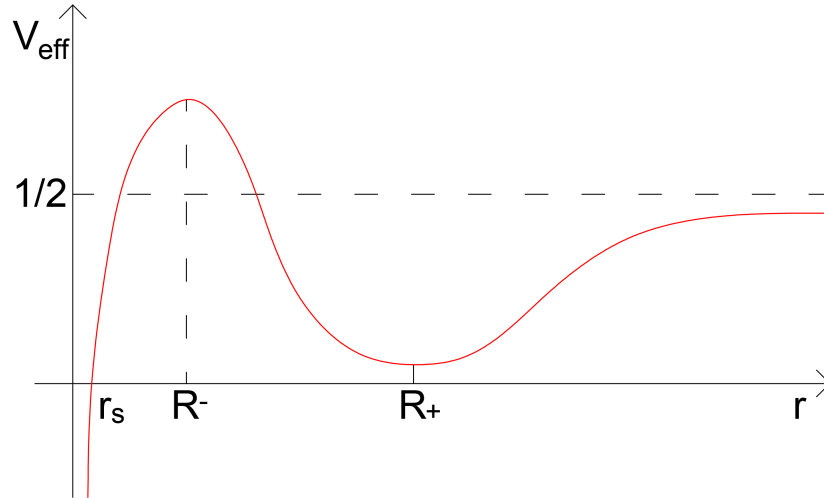

 (a) Case A: $L^2 < 12M^2$.

 (b) Case B: $L^2 > 12M^2$.

 Figure 1.1: Effective potential V_{eff} for time-like geodesics as a function of the radial coordinate r .

By studying the first and second derivatives of the effective potential, Eq. (1.9), we obtain R_+ and R_-

$$R_{\pm} = \frac{L^2 \pm \sqrt{L^4 - 12L^2M^2}}{2}, \quad (1.10)$$

which are a local minimum and maximum, respectively (see Fig. xx). At $r = R_+$, there are stable circular orbits (i.e. $\dot{r} = 0$), whereas at $r = R_-$, there are unstable circular orbits. Again, depending on the value of $E^2/2$, we have different possibilities. For $E^2/2 > 1/2$, the particle travels from infinity to the center of the gravitational field, reverses its motion, and returns to its original location (being a non-periodic motion, it could describe, for example, that of a non-periodic comet). For values of $E^2/2$ greater than the maximum of the potential, we have either a particle that falls on the Sun or a particle that is ejected from the Sun and goes towards infinity. As a result, none of these scenarios describes the motion of a planet. An interesting situation is the following

$$V_{\text{eff}}(R_+) < \frac{E^2}{2} < \frac{1}{2}. \quad (1.11)$$

In this case, we have periodic motions, in the sense that the radial coordinate periodically oscillates between two points that coincide with its minimum value, the perihelion, and its maximum value, the aphelion. Therefore we have finally found the range of values for $E^2/2$ that can be used to describe the motion of the planets.

Now let us study the orbits of these planets. When we combine Eq. (1.6) and Eq. (1.8) together, we get

$$\frac{dr}{d\varphi} = \pm \frac{r^2}{L} \sqrt{E^2 - 2V_{\text{eff}}}, \quad (1.12)$$

which integrated gives r as a function of φ . In the case of a two-body interaction in which the effective potential is Newtonian, the integration of Eq. (1.12) results in an elliptical orbit, that is a closed curve in the equatorial plane in which the radial coordinate varies in a limited interval. Instead, when incorporating the relativistic correction, as in Eq. (1.9), the orbits are no longer closed: instead of being fixed in space as predicted by Newton's theory, the perihelion moves in the direction of the planet's motion (*perihelion precession*). It is worth noting that in Newtonian theory orbits are closed only in the two bodies approximation. However, when we examine the planetary orbit while also incorporating the planet's interactions with other bodies in the Solar System, the effect of perihelion precession appears. Instead, in GR, it is the shape of the potential that is modified, and this alone causes the precession, not the interaction with other planets. Furthermore, because the relativistic correction to V_{eff} goes like $1/r^3$, the potential exercises a greater influence on the planets closest to the Sun. For this reason,

Mercury is an excellent candidate for testing this physical phenomenon. We are unable to calculate the integral of Eq. (1.12) analytically (in terms of elementary functions¹), due to the complexity of Eq. (1.9) which describes the effective potential. It is, nevertheless, possible to perform a perturbation analysis. Let us consider that the orbits of the planets in the Solar System have a small eccentricity (they are almost circular). This means that the radial coordinate varies in a small range in proportion to its average value, and the energy is just above the potential's minimum. In other words, r oscillates in a small neighborhood of R_+ , and in this neighborhood, we can develop V_{eff} in Taylor series, stopping at the second order

$$V_{\text{eff}}(r) \simeq V_{\text{eff}}(R_+) + \frac{1}{2}V_{\text{eff}}''(R_+)(r - R_+)^2, \quad (1.13)$$

valid for $|r - R_+|/R_+ \ll 1$. From Eq. (1.9), we get

$$V_{\text{eff}}(R_+) = -\frac{M}{R_+} + \frac{L^2}{2R_+^2} - \frac{ML^2}{2R_+^3} + \frac{1}{2}, \quad (1.14)$$

$$V_{\text{eff}}''(R_+) = \frac{M}{R_+^3} \left(\frac{R_+ - 6M}{R_+ - 3M} \right). \quad (1.15)$$

Consequently, Eq. (1.8) of the radial motion becomes that of the harmonic motion

$$\frac{1}{2}\dot{r}^2 + \frac{1}{2}\omega_r^2 (r - R_+)^2 = \text{const}, \quad (1.16)$$

where $\omega_r^2 = V_{\text{eff}}''(R_+)$ is the angular velocity. Furthermore, since $\omega_r = 2\pi/\tau_r$, the period τ_r of the motion is

$$\tau_r = 2\pi \sqrt{\frac{R_+^3 R_+ - 3M}{M R_+ - 6M}}. \quad (1.17)$$

To establish whether the planet's orbit closes or not, we calculate the angle covered by the vector radius in a time interval equal to τ_r

$$\Delta\varphi = \dot{\varphi}\tau_r. \quad (1.18)$$

Because the orbit is almost circular, taking into account Eq. (1.6), we have that $\dot{\varphi} = L/R_+^2$ is constant, hence

$$\Delta\varphi = 2\pi \frac{L}{R_+^2} \sqrt{\frac{R_+^3 R_+ - 3M}{M R_+ - 6M}}. \quad (1.19)$$

¹It can be solved analytically but in terms of elliptic functions.

Moreover, from the condition

$$V'_{\text{eff}}(R_+) = 0, \quad (1.20)$$

we can determine L^2 in terms of R_+

$$L^2 = \frac{MR_+^2}{R_+ - 3M}. \quad (1.21)$$

Thus, Eq. (1.19) becomes

$$\Delta\varphi = 2\pi \sqrt{\frac{1}{1 - \frac{6GM}{c^2 R_+}}}, \quad (1.22)$$

where we reintroduced the constants c and G . We can easily see that, for $c \rightarrow \infty$, $\Delta\varphi = 2\pi$: when the radial coordinate makes a complete oscillation, the vector radius describes a turn angle, and the orbit is closed. Otherwise, since the denominator is smaller than 1, we have that $\Delta\varphi > 2\pi$: the perihelion shifts and the orbit is not closed.

Finally, $\frac{6GM}{c^2 R_+}$ is a very small number because it is $3r_S$, with r_S the Schwarzschild radius (which for the Sun is $\simeq 2.95$ km), divided by the mean radius of the planetary orbit (which is of the order of hundreds of millions of km). Ergo, the square root in Eq. (1.22) can then be approximated, yielding

$$\Delta\varphi \simeq 2\pi + \frac{6\pi GM}{c^2 R_+}. \quad (1.23)$$

As already mentioned, we can easily see that the effect is less for planets with larger orbits since R_+ is in the denominator of Eq. (1.23). Let us calculate $\Delta\varphi$ for Mercury. From Eq. (1.23) we get

$$\Delta\varphi \simeq 4.90 \cdot 10^{-7} \text{ rad}, \quad (1.24)$$

which is in perfect agreement with the value measured by Le Verrier [34]

$$\Delta\varphi_{\text{obs}} \simeq 5.00 \cdot 10^{-7} \text{ rad} = 43''/\text{cy}. \quad (1.25)$$

1.1.2 Deflection of light by the Sun

We want to study the propagation of a light ray in the gravitational field of the Sun [36]. The equations we will employ are the same as in Sec. (1.1.1),

with the main difference that, instead of considering massive particles and hence the normalization condition given by Eq. (1.3), this time we will look at a null geodesic, which satisfies the following condition

$$u^2 = 0. \quad (1.26)$$

Radial motion is always described by Eq. (1.8) but with the effective potential

$$V_{\text{eff}} = \frac{L^2}{2r^3} (r - r_S), \quad (1.27)$$

where $r_S = 2M$ is the Schwarzschild radius of the Sun.

Before going any further, let us introduce the *apparent impact parameter*, b

$$b \doteq \frac{L}{E}, \quad (1.28)$$

to simplify the notation. It is the distance between the point $r = 0$ and that of closest approach.

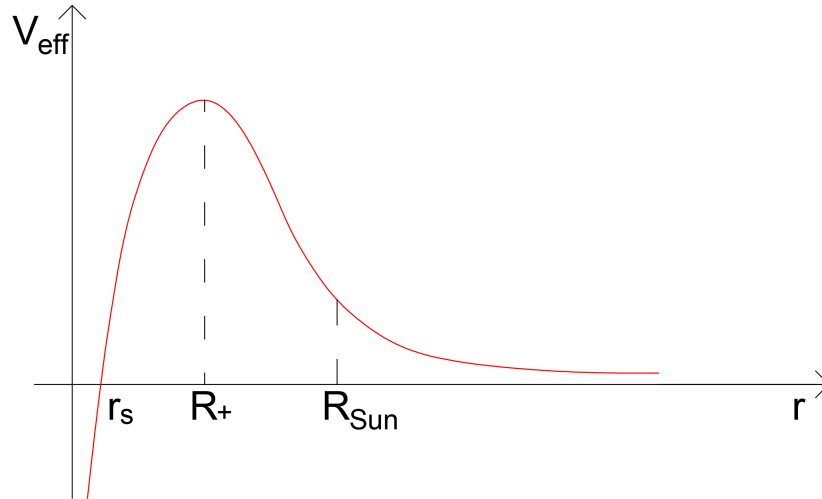


Figure 1.2: Effective potential V_{eff} for null geodesics as a function of the radial coordinate r .

We can now analyze the plot of the effective potential, see Fig. 1.2. First, we can see that as r increases, V_{eff} tends to zero as $1/r^2$, while it diverges as $-1/r^3$. Furthermore, the potential has one maximum at $r = R_+$

$$R_+ = \frac{3}{2}r_S. \quad (1.29)$$

R_+ is much smaller than the solar radius R_{Sun} , therefore it falls inside the Sun. The plot on the left of R_{Sun} is of no physical interest.

The type of orbits is determined by the impact parameter's value. We denote with b_c the critical value of the impact parameter corresponding to a circular orbit around R_+ . To determine b_c , we use Eq. (1.8) with the condition $\dot{r} = 0$, that means

$$\frac{1}{2b_c^2} = V_{\text{eff}}(R_+), \quad (1.30)$$

from which we derive

$$b_c = \frac{3\sqrt{3}}{2}r_S. \quad (1.31)$$

A light beam characterized by this impact parameter value describes an unstable circular orbit. In fact, if we take a value of b slightly less than b_c , the light ray is either ejected from the Sun and travels to infinity or falls on the Sun. On the other hand, if we choose a value of b much smaller than b_c , we have the case of a light ray that comes from infinity, moves towards the Sun and reaches the solar disk because the minimum distance between the ray and the Sun is lower than the solar radius. Consequently, a light beam that grazes the Sun without impacting with it must have a large enough impact parameter. For this reason, we are going to determine the trajectories in the case $b > b_c$. By scaling the affine parameter by a multiplicative factor

$$\lambda \rightarrow \lambda L = \lambda', \quad (1.32)$$

we can rewrite Eq. (1.8) as

$$\frac{1}{2}\dot{r}'^2 + \tilde{V}_{\text{eff}}(r) = \frac{1}{2b^2}, \quad (1.33)$$

with $\tilde{V}_{\text{eff}}(r) = \frac{1}{2r^3}(r - r_S)$. Then, considering that, with the new parameterization, $\dot{\varphi} = 1/r^2$, we get

$$\frac{d\varphi}{dr} = \pm \frac{1}{r^2 \sqrt{\frac{1}{b^2} - \frac{1}{r^2} \left(1 - \frac{r_S}{r}\right)}}, \quad (1.34)$$

where the $+$ sign refers to a ray that moves away from the center of the gravitational field, vice versa for the $-$ sign. It is easy to show that Eq. (1.34) is that of a straight line in the non-relativistic case, as expected: light propagates along a straight line in a flat spacetime.

Now we want to determine the solid angle described by the light beam during its path, in order to calculate its deflection. To achieve this, we integrate Eq. (1.34) by multiplying it by a factor of 2

$$\Delta\varphi = 2 \int_{R_0}^{\infty} \frac{bdr}{r^2 \sqrt{\frac{1}{b^2} - \frac{1}{r^2} \left(1 - \frac{r_S}{r}\right)}}. \quad (1.35)$$

Here, R_0 is the minimum value of the radial coordinate, i.e. the point where the ray's motion is reversed. Therefore, R_0 is the solution of Eq. (1.33) when $\dot{r} = 0$

$$1 - \frac{b^2}{R_0^2} \left(1 - \frac{r_S}{R_0}\right) = 0, \quad (1.36)$$

or, equivalently

$$\left(\frac{R_0}{b}\right)^2 = 1 - \frac{r_S}{R_0}. \quad (1.37)$$

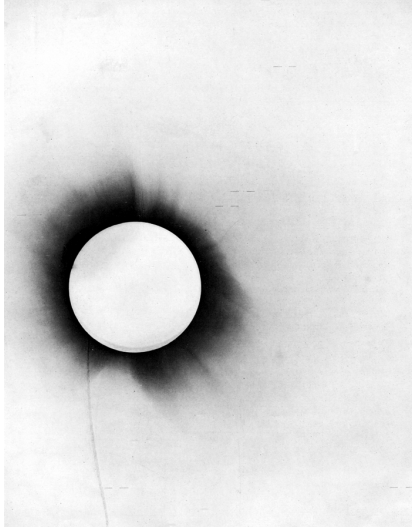
Obviously $R_0 > R_{\text{Sun}}$, otherwise the light beam would hit the solar disk, preventing us from seeing it. The integral of Eq. (1.35) is convergent but it cannot be calculated exactly. However, it is possible to do a series expansion of r_S/R_0 , being a very small quantity. As a result of the integral calculus, we get

$$\Delta\varphi = \pi + 2\frac{r_S}{R_0}. \quad (1.38)$$

Finally, the *deflection of light by the Sun* is

$$\delta\varphi = \Delta\varphi - \pi = \frac{4GM}{c^2 R_0}, \quad (1.39)$$

Figure 1.3: *Photograph taken by Eddington during the 1919 solar eclipse and published in his famous paper [37] in 1920.*



where we reintroduced the constants c and G . As we can see, the deflection is a relativistic effect (it tends to zero

for $c \rightarrow \infty$), and the smaller the R_0 , the greater the deflection, implying that the deflection increases as the light ray approaches the Sun. It is therefore necessary to consider rays that pass very close to the Sun in order to observe the phenomena of deflection. This is why it is preferable to perform the measurement during an eclipse (see Fig.1.3), as Eddington demonstrated for the first time in 1920 [37]. For a ray that grazes the Sun, Eq. (1.39) provides $\delta\varphi \simeq 1.75''$. Einstein was the first to calculate this correct light bending value [35].

1.1.3 Gravitational redshift of light

The gravitational redshift prediction was verified only after Einstein's death, with the famous Pound, Rebka, and Snider experiments [4, 5, 6].

Let us consider the gravitational field generated by a spherically symmetrical body of mass M . This time-independent field is described by the Schwarzschild metric, Eq. (1.1).

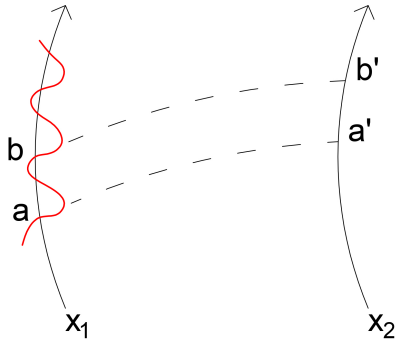


Figure 1.4: *The spacetime diagram shows the world lines of the emitting atom and the observer, both stationary in the gravitational field.*

The (constant) spatial coordinates of a stationary atom placed in this gravitational field are denoted by $x_1 = (r_1, \theta_1, \varphi_1)$. This atom emits radiation corresponding to one of its spectral lines. The radiation is detected by a stationary observer \mathcal{O} , who lies in the same field and whose spatial coordinates² are $x_2 = (r_2, \theta_2, \varphi_2)$. Let ν_1 be the frequency relative to the spectral line of the emitted radiation. What is the value ν_2 of the frequency seen by the observer \mathcal{O} ? We should first note that the frequency of the emitted radiation is a characteristic of the atom, not of its position in the gravita-

²Like the atom, the observer's spatial coordinates are constant since it is stationary. Furthermore, in both cases, the relevant coordinate is the radial one.

tional field. In other words, gravity does not modify the atom's spectrum; rather, observing the radiation in a different reference system than the emitter detects a different frequency, which would not happen if the observer was in the same system reference as the atom. To determine the frequency, we assume the atom being the source of a light vibration characterized by specific period τ_1

$$\nu_1 = \frac{2\pi}{\tau_1}. \quad (1.40)$$

In general, the vibration period τ_1 is not equal to the coordinate time interval t_{ab} between events a and b (see Fig. 1.4). τ_1 is, in fact, a proper time, related to t_{ab} through

$$\tau_1 = \int_a^b dt \sqrt{-g_{\mu\nu} \frac{dx^\mu}{dt} \frac{dx^\nu}{dt}} = \int_a^b dt \sqrt{-g_{00}(x_1)} = \sqrt{1 - \frac{2M}{r_1}} t_{ab}. \quad (1.41)$$

This light radiation travels at the speed of light towards the observer. We are not interested in determining the shape of the wave fronts that characterize the radiation; instead, we want to note that the wave front emitted along the atom's world line at event b is simply translated in the temporal direction by a quantity equal to t_{ab} with respect to that emitted at event a . Since the gravitational field is static, this time interval is constant along the wave front. Then we can deduce that the time interval along the observer's world line corresponding to events a and b of the atom's world line is

$$t_{a'b'} = t_{ab}. \quad (1.42)$$

Therefore, the proper time interval for the observer is

$$\tau_2 = \sqrt{1 - \frac{2M}{r_2}} t_{a'b'} = \sqrt{1 - \frac{2M}{r_2}} t_{ab}, \quad (1.43)$$

and the associated frequency is

$$\nu_2 = \frac{2\pi}{\tau_2}. \quad (1.44)$$

At this point, we can easily calculate the ratio between the two frequencies

$$\frac{\nu_2}{\nu_1} = \frac{\tau_1}{\tau_2} = \frac{\sqrt{1 - \frac{2M}{r_1}}}{\sqrt{1 - \frac{2M}{r_2}}}. \quad (1.45)$$

We can see from Eq.(1.45) that the frequencies ν_1 and ν_2 do not coincide if the atom and the observer occupy different positions in the gravitational field. If $r_2 > r_1$ (as in the case of an atom on the Sun's surface with an observer placed on Earth), $\nu_2 < \nu_1$ and the frequency of the observed radiation appears to be "red-shifted". The fractional shift in frequency is commonly used instead of Eq.(1.45)

$$\frac{\Delta\nu}{\nu} = \frac{\nu_2 - \nu_1}{\nu_1} = \frac{\sqrt{1 - 2M/r_1}}{\sqrt{1 - 2M/r_2}} - 1. \quad (1.46)$$

Because the speed of light appears in all of these equations, this is a relativistic effect. In fact, if we assume c infinite, it vanishes. Furthermore, since Maxwell's equations do not couple the electromagnetic and gravitational fields, this effect does not occur in classical theory.

As already anticipated, Pound and Rebka experiment [4, 5], performed on Earth, provided the first confirmation of this prediction, improved a few years later by Pound and Snider [6]. They considered an emitter atom and an observer inside a tower of height $h \simeq 23$ m. Indicating with M_T and R_T the mass and the radius of the Earth respectively, we have

$$\begin{aligned} \frac{\Delta\nu}{\nu} &= \sqrt{\frac{1 - 2M_T/R_T}{1 - 2M_T/(R_T + h)}} - 1 \simeq \sqrt{\frac{1 - 2M_T/R_T}{1 - \frac{2M_T}{R_T} \left(1 - \frac{h}{R_T}\right)}} - 1 \simeq \\ &\simeq \left(1 - \frac{M_T}{R_T}\right) \left(1 + \frac{M_T}{R_T} - \frac{M_T h}{R_T^2}\right) \simeq -\frac{M_T h}{R_T^2}. \end{aligned} \quad (1.47)$$

During the calculation, we performed series developments, taking into account that $h \ll R_T$, and $2M_T/R_T \ll 1$. The numerical values of Earth's mass and radius, $M_T \simeq 5.97 \cdot 10^{24}$ kg and $R_T \simeq 6.371$ km, are then substituted in Eq.(1.47), giving

$$\frac{\Delta\nu}{\nu} \simeq -2.30 \cdot 10^{-15}. \quad (1.48)$$

Pound and Rebka considered the highly sharp spectral lines due to the nuclear transitions of the iron isotope ^{57}Fe , which emit gamma rays with an energy of 14 keV, because the effect was too weak to observe (we are talking about a fractional shift of one part in 10^{15}). They achieved this by using the characteristics of a previously discovered effect known as *the Mössbauer effect*. After emitting a γ photon, the iron atom recoils, resulting in a Doppler

effect on the emission that is substantially bigger (about 6 – 7 orders of magnitude) than the redshift. In the Mössbauer effect the recoil is negligible. The primary reason for this is that the atom is thought to be in a crystal. As a result, the photon's momentum is transferred to the entire crystal, and what recoils is no longer the single atom but the entire crystal of which the atom is a part. Because the crystal's mass is macroscopic, the recoil velocity caused by photon emission in this situation is several orders of magnitude lower than that of the single atom. The primary source of spectral line broadening is therefore eliminated. In practice, Pound and Rebka employed an iron crystal that released photons that were collected by identical crystal placed above. They then measured how many times the photons were absorbed by this second crystal. If there were no redshift due to the gravitational field, each emitted photon would be collected by resonant absorption. In fact, the probability P of absorption is

$$P \simeq \frac{\Gamma^2}{\Delta\nu^2 + \Gamma^2}, \quad (1.49)$$

where Γ is the natural width of the spectral line, and $\Delta\nu$ the gravitational redshift.

1.1.4 Shapiro time delay

In his work of 1964 [7], Shapiro predicted the time delay of a radar signal sent from Earth to one of the inner planets (Mercury or Venus), travelling close to the Sun, then returning back to be detected again on Earth. To better understand Shapiro's result, let us start with the Schwarzschild metric, Eq. (1.1), to represent the Sun's gravitational field while ignoring the Earth's motion between pulse transmission and its reception. In order to achieve the desired result, we can examine the physical phenomena in the equatorial plane (i.e. $\theta = \pi/2$), by using a suitable coordinate system, without losing generality. Consequently, the metric becomes

$$ds^2 = - \left(1 - \frac{2M}{r}\right) dt^2 + \left(1 - \frac{2M}{r}\right)^{-1} dr^2 + r^2 d\varphi^2. \quad (1.50)$$

Having fixed the geometric background, we now study the photon motion from Earth to the inner planet. As shown in Fig. 1.5, we indicate the Earth's position with respect to the Sun with r_1 and the planet's one with

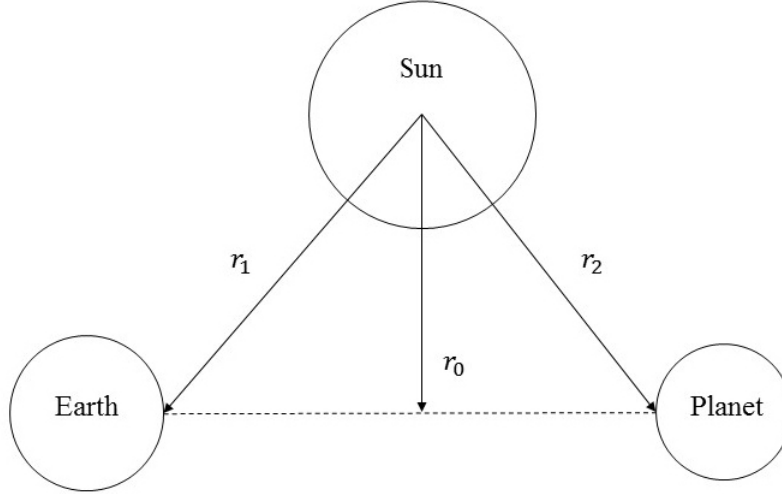


Figure 1.5: *Schematic representation of the positions of Earth and of the inner planet relative to the Sun.*

r_2 ; instead, we denote the so-called *closest approach* distance of the light beam from the Sun with r_0 . By definition, r_0 is the value of the ray that makes $\dot{r} = 0$, that is to say

$$\dot{r}_0 = 0. \quad (1.51)$$

The condition we have to consider for the photon motion is that of null geodesics, $ds^2 = 0$, therefore Eq. (1.50) gives

$$\left(1 - \frac{2M}{r}\right) dt^2 = \left(1 - \frac{2M}{r}\right)^{-1} dr^2 + r^2 d\varphi^2. \quad (1.52)$$

By introducing the affine parameter λ and dividing each term by $d\lambda^2$, we may rewrite Eq. (1.52) as

$$\left(1 - \frac{2M}{r}\right) \left(\frac{dt}{d\lambda}\right)^2 = \left(1 - \frac{2M}{r}\right)^{-1} \left(\frac{dr}{d\lambda}\right)^2 + r^2 \left(\frac{d\varphi}{d\lambda}\right)^2 \quad (1.53)$$

or

$$\left(1 - \frac{2M}{r}\right) \dot{t}^2 = \left(1 - \frac{2M}{r}\right)^{-1} \dot{r}^2 + r^2 \dot{\varphi}^2. \quad (1.54)$$

If we evaluate Eq. (1.54) in r_0 , taking Eq. (1.51) into account, we get

$$\left(1 - \frac{2M}{r_0}\right) \dot{t}^2 = r_0^2 \dot{\varphi}^2. \quad (1.55)$$

We denote with $\{u^\mu\} = \{\dot{t}, \dot{r}, 0, \dot{\varphi}\}$ the four-velocity of the photon travelling in the equatorial plane. Here, the dot indicates the derivative with respect to the affine parameter λ . Let us observe that there are two constants of motion associated with the photon since metric components are independent from t and φ , the total energy E and the angular momentum L

$$E = \left(1 - \frac{2M}{r}\right) \dot{t}; \quad (1.56)$$

$$L = r^2 \dot{\varphi}. \quad (1.57)$$

By substituting Eqs. (1.56) - (1.57) into Eq. (1.55) we obtain

$$\frac{L^2}{E^2} = \frac{r_0^2}{1 - 2M/r_0} \quad (1.58)$$

which relates E and L with r_0 . Now, we employ Eqs. (1.56) - (1.58) to reduce Eq. (1.54) to the following

$$\left(\frac{\dot{r}}{\dot{t}}\right)^2 = \left(1 - \frac{2M}{r}\right)^2 - \left(1 - \frac{2M}{r}\right)^3 \left(1 - \frac{2M}{r_0}\right)^{-1} \left(\frac{r_0}{r}\right)^2, \quad (1.59)$$

and finally to get

$$\frac{dr}{dt} = \pm \left(1 - \frac{2M}{r}\right) \sqrt{1 - \left(\frac{r_0}{r}\right)^2 \frac{1 - 2M/r}{1 - 2M/r_0}}. \quad (1.60)$$

We need to integrate this differential equation, that is to solve

$$\int_{t_0}^t dt' = \pm \int_{r_0}^r \frac{dr'}{\left(1 - \frac{2M}{r'}\right) \sqrt{1 - \left(\frac{r_0}{r'}\right)^2 \frac{1 - 2M/r'}{1 - 2M/r_0}}}. \quad (1.61)$$

Depending on whether we are dealing with $t > t_0$ or $t < t_0$, we will use the + or - sign, respectively. We will now analyze the case $t > t_0$ and, as a result, we will consider the + sign. Since $2M \ll 1$ along the entire photon's

worldline, we can develop in Taylor series with respect to M and in $M = 0$ the integrand on the right-hand side of Eq. (1.61), up to the first order. In this way, Eq. (1.61) becomes

$$\int_{t_0}^t dt' = \int_{r_0}^r \frac{r'}{\sqrt{r'^2 - r_0^2}} \left[1 + \frac{M(3r_0 + 2r')}{r'(r_0 + r')} \right] dr', \quad (1.62)$$

whose solution is

$$t - t_0 = F(r), \quad (1.63)$$

where

$$F(r) \equiv \sqrt{r^2 - r_0^2} + M\sqrt{\frac{r - r_0}{r + r_0}} + 2M \log \left(\frac{r + \sqrt{r^2 - r_0^2}}{r_0} \right). \quad (1.64)$$

Finally, we have all of the instruments necessary to determine the photon's round trip time from Earth to the planet and back, which is

$$\Delta t = 2[F(r_1) + F(r_2)], \quad (1.65)$$

specifically

$$\begin{aligned} \Delta t = & 2 \left(\sqrt{r_1^2 - r_0^2} + \sqrt{r_2^2 - r_0^2} \right) + 2M \left(\sqrt{\frac{r_1 - r_0}{r_1 + r_0}} + \sqrt{\frac{r_2 - r_0}{r_2 + r_0}} \right) + \\ & + 4M \log \left[\frac{\left(r_1 + \sqrt{r_1^2 - r_0^2} \right) \left(r_2 + \sqrt{r_2^2 - r_0^2} \right)}{r_0^2} \right]. \end{aligned} \quad (1.66)$$

Here,

$$\Delta t_N \doteq 2 \left(\sqrt{r_1^2 - r_0^2} + \sqrt{r_2^2 - r_0^2} \right) \quad (1.67)$$

is the Newtonian term, while

$$\begin{aligned} \Delta t_d \doteq & 2M \left(\sqrt{\frac{r_1 - r_0}{r_1 + r_0}} + \sqrt{\frac{r_2 - r_0}{r_2 + r_0}} \right) + \\ & + 4M \log \left[\frac{\left(r_1 + \sqrt{r_1^2 - r_0^2} \right) \left(r_2 + \sqrt{r_2^2 - r_0^2} \right)}{r_0^2} \right] \end{aligned} \quad (1.68)$$

is the *Shapiro time delay*. Let us make some considerations. First of all, we determined the Shapiro delay through the geodetic approach, that is, we considered the fact that the photon follows a geodesic in the spacetime. However, a less precise approximation in which the photon travels in a straight line (hence the name “straight path approximation”) is also conceivable. In this case, the first term in Eq. (1.68) becomes

$$-2M \left(\frac{\sqrt{r_1^2 - r_0^2}}{r_1} + \frac{\sqrt{r_2^2 - r_0^2}}{r_2} \right). \quad (1.69)$$

Some authors (Misner et al [33], Ohanian & Ruffini [38]) claim that the two procedures provide the same result at first-order. Last we recall that, in his original paper [7], Shapiro estimated the time delay in the straight path approximation and in terms of the x coordinate related to the radial one through $x_i^2 = r_i^2 - r_0^2$, with $i = 1, 2$, providing

$$\begin{aligned} \Delta t_d = & -2M \left(\frac{x_2}{\sqrt{x_2^2 + r_0^2}} + \frac{2x_1 + x_2}{\sqrt{x_1^2 + r_0^2}} \right) + \\ & + 4M \log \left(\frac{x_2 + \sqrt{x_2^2 + r_0^2}}{-x_1 + \sqrt{x_1^2 + r_0^2}} \right), \end{aligned} \quad (1.70)$$

where he also considered the fact that time dilation caused by the Sun’s gravitational field affects the overall transit time as measured by a clock on Earth.

The value of the time delay predicted by Shapiro (and then experimentally verified) for a radar signal that starts from the Earth, travels towards Venus approaching the Sun, and comes back, when this three-body system is in the best possible alignment position, is $\sim 200\mu s$.

1.2 The Parametrized Post-Newtonian formalism

In the previous sections we analyzed the classical tests of GR, all based on the Schwarzschild solution. However, the non-linearity of Einstein’s field equations makes it difficult to find exact solutions, unless particular symmetries are imposed, such as time independence and/or spherical symmetry of

the Schwarzschild metric. The PPN formalism arises from the necessity to determine solutions that are not strictly exact but rather do not depend on such symmetries [39].

In the Solar System [33], gravity is weak and the potential becomes Newtonian

$$|\phi| = |\phi_N| \lesssim 10^{-6}, \quad (1.71)$$

and the matter that generates the gravitational field moves with a very low velocity v (relative to the center of mass of the Solar System)

$$|v^2| \lesssim 10^{-7}. \quad (1.72)$$

Furthermore, the ratio between the stress energy tensor T_{jk} and the rest-mass density ρ_0 is

$$|T_{jk}|/\rho_0 \lesssim 10^{-6}, \quad (1.73)$$

and the internal energy per unit of baryon mass

$$\Pi = (\rho - \rho_0)/\rho_0 \lesssim 10^{-6}. \quad (1.74)$$

As a result, the theoretical analysis of the Solar System can be performed, without significant loss of accuracy, by taking into account series development in the parameters $|\phi|$, v^2 , $|T_{jk}|/\rho_0$ e Π . This approach gives the flat and empty spacetime at zero order, the Newtonian description of the Solar System at the first order and the post-Newtonian one at the second order. *Post Newtonian approximation* or *PPN formalism* is the ensemble of Newtonian formalism and post Newtonian corrections.

There are two possible formulations of the post Newtonian approximation

1. the Eddington-Robertson-Schiff (ERS);
2. the Will-Nordtvedt (WN).

In the formulation 1, spacetime is spherically symmetric and static, with the Sun as a massive particle and planets as test particles. There are only two parameters in the ERS approach [33, 40, 41]: γ , and β . It is therefore a rough approximation which is not properly suited to the treatment of post-Newtonian dynamics.

The best method to compare theoretical models with observations is through the approach 2. In fact, the WN formulation [35, 41, 42] treats the planets of the Solar System as objects with finite volume and density; in other words,

it is fluid-based rather than point particle-based.

In this section we analyze this PPN formalism, starting with the first order of the expansion, i.e. the Newtonian approximation, and then arriving at the complete formulation with the post-Newtonian (second) order.

1.2.1 Newtonian approximation

A gravitational system can be accurately described by Newtonian theory only in the limit of weak gravity and low velocity. The conditions for this to happen are

1. individual velocities of all system bodies with respect to the system's center of mass must be much smaller than the speed of light

$$v \ll 1; \tag{1.75}$$

2. the Newtonian gravitational potential U must be

$$U \ll 1; \tag{1.76}$$

3. the system's internal stresses must be much smaller than the mass-energy density

$$\frac{|T^{ij}|}{T^{00}} = \frac{|T^{ij}|}{\rho_0} \ll 1. \tag{1.77}$$

To understand when GR is reduced to Newtonian theory, we look at particles geodesics. Let us first recall that in Newton's theory, the world lines of particles are described by the following equation

$$\frac{d^2 x^i}{dt^2} = \frac{\partial U}{\partial x^i}. \tag{1.78}$$

Now, let us apply the low velocity and weak field limit to the GR, that means considering

$$g_{\mu\nu} = \eta_{\mu\nu} + h_{\mu\nu}, \quad |h_{\mu\nu}| \ll 1, \quad |v^j| = \left| \frac{dx^j}{dt} \right| \ll 1. \tag{1.79}$$

Taking these conditions into account in the geodesic equation of GR

$$\frac{d^2 x^i}{dt^2} = -\Gamma_{\alpha\beta}^i \frac{dx^\alpha}{dt} \frac{dx^\beta}{dt}, \tag{1.80}$$

we get

$$\frac{d^2 x^i}{dt^2} = \frac{1}{2} h_{00,i}. \tag{1.81}$$

By comparing Eq. (1.81) with Eq. (1.78), we have that GR is reduced to Newton's theory when

$$g_{00} = -1 + 2U. \tag{1.82}$$

1.2.2 Post-Newtonian approximation

We have seen, from Eqs. (1.71) - (1.74), that the Solar System can be described by a weak field and slow motion approximation. Indicating with ϵ^2 the maximum value assumed by the gravitational potential U , we can express the order of "smallness" of the expansion parameters as

$$U \sim v^2 \sim p/\rho_0 \sim \Pi \sim O(\epsilon^2). \tag{1.83}$$

This also implies that $v \sim O(\epsilon)$, $U^2 \sim O(\epsilon^4)$, and so on. Furthermore, since the (slow) motion of matter affects the variation over time of a quantity A , for a fixed x_j , we have

$$\left| \frac{\partial A / \partial t}{\partial A / \partial x_j} \right| \sim |v_j| \sim O(\epsilon). \tag{1.84}$$

These two conditions show that quantities with an odd number of v or $\partial/\partial t$ are odd in ϵ , and hence of the order $O(\epsilon)$, $O(\epsilon^3)$, and so on. Since $x_0 = -x_0$ under time reversal, these terms likewise change sign under this transformation. As a result, the metric coefficients g_{0j} change sign, whilst g_{00} and g_{jk} do not; in other words, the former has odd terms in ϵ , while the others have even terms.

Thus, post-Newtonian expansion necessitates a knowledge of the metric components at the following orders of magnitude

$$g_{00} \text{ up to } O(\epsilon^4), \tag{1.85}$$

$$g_{0j} \text{ up to } O(\epsilon^3), \tag{1.86}$$

$$g_{jk} \text{ up to } O(\epsilon^2). \tag{1.87}$$

Once the orders of magnitude have been established, we define the potentials that appear in post-Newtonian approximation. To this end, Will [42] lists a set of rules which we summarize here

1. metric corrections must be at most of the post-Newtonian order;
2. denoting by $|\mathbf{x} - \mathbf{x}'|$ the distance between a point \mathbf{x} of the field and a point \mathbf{x}' associated with the matter distribution, metric corrections must tend to zero when this distance tends to infinity, i.e. the metric must be Minkowskian at infinity;
3. a suitable coordinate system is chosen to make the metric adimensional;
4. the origin of the coordinates (spatial and temporal) is arbitrary in the coordinate system chosen in the previous point. This condition is guaranteed if each functional is expressed in terms of the distance $|\mathbf{x} - \mathbf{x}'|$;
5. the metric corrections h_{00} , h_{0j} , and h_{jk} should transform as a scalar, vector, and tensor, respectively, under spatial rotations;
6. it is possible to consider only functionals created by ρ_0 , Π , p , $T^{\mu\nu}$, and v , but not by their gradients, for simplicity's sake;
7. it would be better to consider simple functionals.

At this point we have all the ingredients necessary to determine the PPN approximation.

We start with the spatial components of the metric tensor. There are only two possible functionals which satisfy the constraints listed above and which cause g_{jk} to be of the order $O(\epsilon^2)$ (according to Eq. (1.87))

$$\delta_{jk}U = \delta_{jk} \int \frac{\rho_0(\mathbf{x}'-t)}{|\mathbf{x}-\mathbf{x}'|} d^3x'; \tag{1.88}$$

$$U_{jk} = \int \frac{\rho_0(\mathbf{x}'-t)(x_j-x'_j)(x_k-x'_k)}{|\mathbf{x}-\mathbf{x}'|^3} d^3x'. \tag{1.89}$$

In fact, we are dealing with simple and dimensionless functionals of ρ_0 , which transform as tensors and go to zero as $1/|\mathbf{x} - \mathbf{x}'|$ at infinity. As a result, the corrections to the g_{jk} components must be a linear combination of these functionals. For this purpose, it might be useful to introduce a “super - potential” $\chi(\mathbf{x}, t)$ such that

$$\chi(\mathbf{x}, t) \doteq - \int \rho_0(\mathbf{x}', t) |\mathbf{x} - \mathbf{x}'| d^3x'; \tag{1.90}$$

$$\chi_{,jk} = -\delta_{jk}U + U_{jk}; \tag{1.91}$$

$$\nabla^2\chi = -2U. \tag{1.92}$$

Similarly, we observe that the mixed components g_{0j} of the metric tensor, whose order is defined by Eq. (1.86), must be a linear combination of the following potentials

$$V_j(\mathbf{x}, t) = \int \frac{\rho_0(\mathbf{x}', t) v_j(\mathbf{x}', t)}{|\mathbf{x} - \mathbf{x}'|} d^3 x', \quad (1.93)$$

$$W_j(\mathbf{x}, t) = \int \frac{\rho_0(\mathbf{x}', t) [(\mathbf{x} - \mathbf{x}') \cdot \mathbf{v}(\mathbf{x}', t)] (x_j - x'_j)}{|\mathbf{x} - \mathbf{x}'|^3} d^3 x', \quad (1.94)$$

and in this case we have

$$\chi_{,0j} = V_j - W_j. \quad (1.95)$$

Finally, for the g_{00} component of the metric tensor, whose order is defined by Eq. (1.85), constraint 7 allows us to make a selection among all (many) possible functionals that also satisfy the other conditions. Hence, g_{00} must include a linear combination of the following potentials

$$\mathcal{A} = \int \frac{\rho'_0 [\mathbf{v}' \cdot (\mathbf{x} - \mathbf{x}')]^2}{|\mathbf{x} - \mathbf{x}'|^3} d^3 x', \quad (1.96)$$

$$\mathcal{B} = \int \frac{\rho'_0}{|\mathbf{x} - \mathbf{x}'|} (\mathbf{x} - \mathbf{x}') \cdot \frac{d\mathbf{v}'}{dt} d^3 x', \quad (1.97)$$

$$\Phi_1 = \int \frac{\rho'_0 v'^2}{|\mathbf{x} - \mathbf{x}'|} d^3 x', \quad (1.98)$$

$$\Phi_2 = \int \frac{\rho'_0 U'}{|\mathbf{x} - \mathbf{x}'|} d^3 x', \quad (1.99)$$

$$\Phi_3 = \int \frac{\rho'_0 \Pi'}{|\mathbf{x} - \mathbf{x}'|} d^3 x', \quad (1.100)$$

$$\Phi_4 = \int \frac{p'}{|\mathbf{x} - \mathbf{x}'|} d^3 x', \quad (1.101)$$

$$\Phi_W = \int \rho'_0 \rho''_0 \frac{\mathbf{x} - \mathbf{x}'}{|\mathbf{x} - \mathbf{x}'|^3} \cdot \left(\frac{\mathbf{x}' - \mathbf{x}''}{|\mathbf{x} - \mathbf{x}''|} - \frac{\mathbf{x} - \mathbf{x}''}{|\mathbf{x}' - \mathbf{x}''|} \right) d^3 x' d^3 x''. \quad (1.102)$$

Here we used the notation $k' = k(\mathbf{x}', t)$, for a given quantity k . It is possible to demonstrate that the potentials that we have seen so far

satisfy the properties listed below

$$\nabla^2 V_j = -4\pi\rho_0 v_j, \quad V_{j,j} = -U_{,0} \quad (1.103)$$

$$\nabla^2 \Phi_1 = -4\pi\rho_0 v^2, \quad (1.104)$$

$$\nabla^2 \Phi_2 = -4\pi\rho_0 U, \quad (1.105)$$

$$\nabla^2 \Phi_3 = -4\pi\rho_0 \Pi, \quad (1.106)$$

$$\nabla^2 \Phi_4 = -4\pi p, \quad (1.107)$$

$$\nabla^2 (\Phi_W + 2U^2 - 3\Phi_2) = 2\chi_{,ij} U_{,ij}, \quad (1.108)$$

$$\chi_{,00} = \mathcal{A} + \mathcal{B} - \Phi_1. \quad (1.109)$$

Given the arbitrariness of the chosen coordinate system, we can introduce an appropriate gauge transformation to simplify the metric components in the PPN approximation. It is

$$x^{\bar{\mu}} = x^\mu + \xi^\mu(x^\nu), \quad (1.110)$$

consequently

$$\bar{g}_{\bar{\mu}\bar{\nu}}(x^{\bar{\alpha}}) = g_{\mu\nu}(x^{\bar{\alpha}}) - \xi_{\mu;\nu} - \xi_{\nu;\mu}. \quad (1.111)$$

Anyway, this metric must satisfy Will's conditions for the PPN formalism. This implies that

- $\xi_{\mu;\nu} + \xi_{\nu;\mu}$ must be of the post-Newtonian order;
- $\xi_{\mu;\nu} + \xi_{\nu;\mu} \rightarrow 0$, at infinity;
- $|\xi^\mu|/|x^\mu| \rightarrow 0$, at infinity;
- $\xi_{\mu;\nu} + \xi_{\nu;\mu}$ must be constituted by simple functionals.

The superpotential χ introduced before is the functional that guarantees the validity of these constraints, through its gradient. Therefore, we fix

$$\xi_0 = \lambda_1 \chi_{,0}, \quad \xi_j = \lambda_2 \chi_{,j}. \quad (1.112)$$

Now, taking Eqs. (1.111) - (1.112) into account, and applying the properties of the superpotential given by Eqs. (1.95) - (1.109), we get

$$\bar{g}_{\bar{0}\bar{0}} = g_{00} - 2\lambda_2 (U^2 + \Phi_W - \Phi_2) - 2\lambda_1 (\mathcal{A} + \mathcal{B} - \Phi_1), \quad (1.113)$$

$$\bar{g}_{\bar{0}\bar{j}} = g_{0j} - (\lambda_1 + \lambda_2) (V_j - W_j), \quad (1.114)$$

$$\bar{g}_{\bar{j}\bar{k}} = g_{jk} - 2\lambda_2 \chi_{,jk}. \quad (1.115)$$

Will then uses the so-called “*standard post-Newtonian gauge*”, in which the spatial part of the metric is diagonal and isotropic, and the potential \mathcal{B} vanishes, to further simplify the result. Moreover, instead of the coefficients λ_1 and λ_2 , the author provides a parameter for each term that appears in the expansion, for a total of ten PPN parameters ($\gamma, \beta, \xi, \alpha_1, \alpha_2, \alpha_3, \zeta_1, \zeta_2, \zeta_3,$ and ζ_4). Moreover, he combines them in such a way that each PPN acquires a precise physical meaning (see Tab. 1.1). We thus definitively arrive at the PPN approximation

$$\begin{aligned}
 g_{00} = & -1 + 2U - 2\beta U^2 - 2\xi\Phi_W + (2\gamma + 2 + \alpha_3 + \zeta_1 - 2\xi)\Phi_1 + \\
 & + 2(3\gamma - 2\beta + 1 + \zeta_2 + \xi)\Phi_2 + 2(1 + \zeta_3)\Phi_3 + \\
 & + 2(3\gamma + 3\zeta_4 - 2\xi)\Phi_4 - (\zeta_1 - 2\xi)\mathcal{A}, \tag{1.116}
 \end{aligned}$$

$$\begin{aligned}
 g_{0j} = & -\frac{1}{2}(4\gamma + 3 + \alpha_1 - \alpha_2 + \zeta_1 - 2\xi)V_j + \\
 & -\frac{1}{2}(1 + \alpha_2 - \zeta_1 + 2\xi)W_j, \tag{1.117}
 \end{aligned}$$

$$g_{jk} = (1 + 2\gamma U)\delta_{jk}. \tag{1.118}$$

Parameter	What it measures relative to GR
γ	How much space-curvature produced by unit rest mass?
β	How much “non - linearity” in the superposition law for gravity?
ξ	Preferred - location effects?
α_1	Preferred - frame effects?
α_2	
α_3	
α_3	Violation of conservation of total momentum?
ζ_1	
ζ_2	
ζ_3	
ζ_4	

Table 1.1: *Will’s table on PPN parameters and their physical meaning [42].*

In the ERS formulation of the post-Newtonian approximation, the metric

tensor components depend only on two parameters (γ , and β), as follows

$$g_{00} = -1 + \frac{2M}{r} - 2\beta \left(\frac{M}{r}\right)^2, \quad (1.119)$$

$$g_{0j} = 0, \quad (1.120)$$

$$g_{jk} = \left(1 + \frac{2\gamma M}{r}\right), \quad (1.121)$$

where M is the Sun's mass.

GR gives the same results in both formulations (WN and ERS); however, the same may not be true, a priori, for extended and modified theories of gravity.

1.2.3 Post-Newtonian stress-energy tensor

As already mentioned, Will and Nordtvedt's PPN formalism is fluid-based. A perfect fluid is characterized by the following stress-energy tensor

$$T^{\mu\nu} = (\rho_0 + \rho_0\Pi + p) u^\mu u^\nu + pg^{\mu\nu}, \quad (1.122)$$

where $u^\mu = (u^0, \mathbf{v})$ is the four-velocity of a fluid element.

We want to compute the post-Newtonian corrections of the stress-energy tensor. First of all, we note that, similarly to the metric tensor, PPN approximation necessitates a knowledge of the $T^{\mu\nu}$ components at the following orders of magnitude

$$T^{00} \text{ up to } \rho_0 O(\epsilon^2), \quad (1.123)$$

$$T^{0j} \text{ up to } \rho_0 O(\epsilon^3), \quad (1.124)$$

$$T^{jk} \text{ up to } \rho_0 O(\epsilon^4). \quad (1.125)$$

Then, based on the orders of magnitude required for $T^{\mu\nu}$ and on Eqs. (1.116) - (1.118), we determine the corrections of the u^0 component of the four-velocity up to the following order [43]

$$u^0 = 1 + \frac{1}{2}v^2 + U + O(\epsilon^4). \quad (1.126)$$

Furthermore, since $u^i = v^i u^0$, we get

$$u^i = \left(1 + \frac{1}{2}v^2 + U\right) v^i + O(\epsilon^4). \quad (1.127)$$

Therefore, by substituting Eqs. (1.126) - (1.127) into Eq. (1.122) and considering the metric tensor corrections up to the appropriate orders, we obtain the PPN approximation of the stress-energy tensor

$$T^{00} = \rho (1 + \Pi + v^2 + 2U), \quad (1.128)$$

$$T^{0i} = \rho \left(1 + \Pi + v^2 + 2U + \frac{p}{\rho} \right) v^i, \quad (1.129)$$

$$T^{ij} = \rho \left(1 + \Pi + v^2 + 2U + \frac{p}{\rho} \right) v^i v^j + p \delta^{ij} (1 - 2\gamma U). \quad (1.130)$$

1.3 PPN parameters in metric theories of gravity

The value of the PPN parameters changes according to the theory under investigation. For this reason, experiments that provide PPN parameters can be used to test gravity theories: depending on the measured values, we can determine which theoretical model best fits the observations.

How can the theoretical formulation of the PPN parameters be determined in a unique way for each theory?

Again, Will [42] gives us a set of rules that we summarize here.

1. Establish the variables that characterize the theoretical model for which the PPNs will be calculated: the dynamic geometric variables (e.g. the metric $g_{\mu\nu}$, a scalar field ϕ , a vector field K^μ , a tensor field $B_{\mu\nu}$), the geometric background, matter, and non - gravitational field variables.
2. Fix cosmological boundary conditions and the asymptotic values of the variables identified in the previous step. Generally, a homogeneous and isotropic cosmological spacetime is considered. For example³

$$g_{\mu\nu} \rightarrow g_{\mu\nu}^{(0)} = \text{diag}(-c_0, c_1, c_1, c_1), \quad (1.131)$$

$$\phi \rightarrow \phi_0, \quad (1.132)$$

$$K_\mu \rightarrow (K, 0, 0, 0), \quad (1.133)$$

$$B_{\mu\nu} \rightarrow B_{\mu\nu}^{(0)} = \text{diag}(\omega_0, \omega_1, \omega_1, \omega_1). \quad (1.134)$$

³Usually, the metric tensor is considered asymptotically Minkowskian, which means that $c_0 = c_1 = 1$.

3. Do the series expansion up to the post-Newtonian order of the variables around their asymptotic value. For the dynamic geometric variables of the previous step, this is equivalent to

$$g_{\mu\nu} = g_{\mu\nu}^{(0)} + h_{\mu\nu}, \quad (1.135)$$

$$\phi = \phi_0 + \varphi, \quad (1.136)$$

$$K_\mu = (K + k_0, k_1, k_2, k_3), \quad (1.137)$$

$$B_{\mu\nu} = B_{\mu\nu}^{(0)} + b_{\mu\nu}, \quad (1.138)$$

with

$$h_{00} \sim O(\epsilon^2) + O(\epsilon^4), \quad h_{0j} \sim O(\epsilon^3), \quad h_{ij} \sim O(\epsilon^2), \quad (1.139)$$

$$\varphi \sim O(\epsilon^2) + O(\epsilon^4), \quad (1.140)$$

$$k_0 \sim O(\epsilon^2) + O(\epsilon^4), \quad k_j \sim O(\epsilon^3), \quad (1.141)$$

$$b_{00} \sim O(\epsilon^2) + O(\epsilon^4), \quad b_{0j} \sim O(\epsilon^3), \quad b_{ij} \sim O(\epsilon^2), \quad (1.142)$$

4. Replace the expansions calculated in the step 3 and Eqs. (1.128) - (1.130) for the stress-energy tensor into the field equations, assuming the corrections always stops at the post-Newtonian order.
5. Find a solution for h_{00} up to $O(\epsilon^2)$. It is possible to choose $h_{00} \rightarrow 0$ at infinity, so that
- $$h_{00} = 2\alpha U, \quad (1.143)$$
- where α is a function of the characteristic parameters of the theory.
6. Find a solution for h_{ij} up to $O(\epsilon^2)$ and for h_{0j} up to $O(\epsilon^3)$. At this point, if the theory under consideration has a gauge freedom, it is possible to fix one that simplifies the equations.
7. Find a solution for h_{00} up to $O(\epsilon^4)$.
8. Apply the standard PPN gauge.
9. Compare the series expansion of the metric tensor components just obtained with the standard one of Will and Nordtvedt (see Eqs. (1.116) - (1.118)).

Will uses the procedure outlined above to calculate PPN parameters for numerous metric theories of gravity. In the following sections, we present his results⁴.

⁴We refer to [42] for more details.

1.3.1 Metric theories of gravity

Einstein's Principle of Equivalence (EEP) is a milestone of the gravitational theory. It can be divided into three parts [42, 44].

1. Universality of Free Fall (UFF) - or, equivalently, the Weak Equivalence Principle (WEP): the trajectory of a freely falling test body is independent of its internal structure and composition.
2. Local Lorentz Invariance (LLI): the result of any local non-gravitational test experiment is independent of the (freely falling) apparatus' velocity and orientation.
3. Local Position Invariance (LPI): the result of any local non-gravitational test experiment is independent of where and when it is performed.

The EEP is called Strong Equivalence Principle (SEP) if we include bodies with self - gravitational interactions and experiments involving gravitational forces. In other words, the EEP states that gravity is described by a metric in curved spacetime; bodies follow the geodesics of the metric; and the (non-gravitational) laws of physics are reduced to those of special relativity in any local Lorentz frame.

All theories characterized by a metric and that satisfy the EPP are known as “*metric theories*”. Moreover, from a purely mathematical point of view [33], they are the simplest gravitational theories satisfying the criteria of

- *self - consistency*: propositions do not entail logical contradictions;
- *completeness*: all propositions can be demonstrated (or refuted);
- *agreement with past experiments*: the results of (earlier) performed gravity tests are accurately replicated.

It is evident right away that GR is a metric theory. So, let us begin by applying Will's rules to GR to determine its PPN parameters. In this regard, we consider the Einstein-Hilbert action

$$\mathcal{A}_{\text{GR}} = \frac{1}{16\pi} \int \sqrt{-g} R d^4x + \mathcal{A}_{\text{m}}, \quad (1.144)$$

with \mathcal{A}_{m} the matter action. It provides the field equations for GR

$$R_{\mu\nu} - \frac{1}{2}g_{\mu\nu}R = 8\pi T_{\mu\nu}, \quad (1.145)$$

through the variational principle. It is straightforward that the metric $g_{\mu\nu}$ is the only variable in Eq. (1.144). Therefore, we have to choose the asymptotic condition exclusively for $g_{\mu\nu}$. Typically, we assume a metric to be asymptotically Minkowskian

$$g_{\mu\nu} \rightarrow g_{\mu\nu}^{(0)} = \text{diag}(-1, 1, 1, 1). \quad (1.146)$$

Further, it is possible to fix gauge conditions. The author sets

$$h_{i,\mu}^{\mu} - \frac{1}{2}h_{\mu,i}^{\mu} = 0, \quad \text{with } i = 1, 2, 3, \quad \text{and } h_{\alpha}^{\mu} \equiv \eta^{\mu\beta}h_{\beta\alpha}, \quad (1.147)$$

$$h_{0,\mu}^{\mu} - \frac{1}{2}h_{\mu,0}^{\mu} = -\frac{1}{2}h_{00,0}. \quad (1.148)$$

Hence, solving order by order in perturbations, we finally arrive at

$$g_{00} = -1 + 2U - 2U^2 + 4\Phi_1 + 4\Phi_2 + 2\Phi_3 + 6\Phi_4, \quad (1.149)$$

$$g_{0j} = -\frac{7}{2}V_j - \frac{1}{2}W_j, \quad (1.150)$$

$$g_{ij} = (1 + 2U)\delta_{ij}. \quad (1.151)$$

By comparing these equations, term by term, with Eqs. (1.116) - (1.118), we determine the PPN parameters for GR

$$\gamma = \beta = 1, \quad (1.152)$$

$$\xi = \alpha_1 = \alpha_2 = \alpha_3 = \zeta_1 = \zeta_2 = \zeta_3 = \zeta_4 = 0. \quad (1.153)$$

Clearly, GR is not the only conceivable metric theory.

In general, metric theories are distinguished by the number and type of fields (other than the metric) present, as well as how they evolve in space and time. Consider a local reference frame (small enough to neglect the external inhomogeneities but large enough to incorporate a system of gravitating matter and related gravitational forces). It follows that [35]

- a metric theory that is endowed only with a metric tensor $g_{\mu\nu}$ satisfies all three statements of the EEP, even in strong form. This is because, away from the local system, on the boundaries with the external one, it is always feasible to construct a reference system in which $g_{\mu\nu}$ takes the form of the Minkowski metric. An example is GR;

- a metric theory with a metric tensor and a scalar field could violate the LPI due to the scalar field's dependency on the frame's location;
- a metric theory that contains dynamic vector and tensor fields could lead to a violation of both the LPI and the LLI.

As a result, we could use alternative metric theories to GR to verify possible violations of some principles, such as SEP. By extension, they enable us to describe physical phenomena that, without introducing new physics, we would be unable to explain in the context of GR.

In the next sections, we will look at different metric theories of gravity and how they are expressed in the PPN formalism.

1.3.2 Horndeski's theory

The introduction of scalar fields in Einstein-Hilbert action to mediate gravity was motivated by the need to explain cosmological observations like the accelerated expansion of the universe and the homogeneity of the CMB. Horndeski found the most general extension of GR that includes scalar fields and involves field equations at most of the second order [45]. This theory is described by the following action

$$\mathcal{A}_H = \sum_{i=2}^5 \int d^4x \sqrt{-g} \mathcal{L}_i[g_{\mu\nu}, \phi] + \mathcal{A}_m, \quad (1.154)$$

where the matter action is denoted by \mathcal{A}_m . The gravitational action depends on two variables, the metric $g_{\mu\nu}$ and the scalar field ϕ . It is obtained from the sum of four Lagrangians

$$\mathcal{L}_2 = K(\phi, X), \quad (1.155)$$

$$\mathcal{L}_3 = -G_3(\phi, X) \square \phi, \quad (1.156)$$

$$\mathcal{L}_4 = G_4(\phi, X) R + G_{4X}(\phi, X) [(\square \phi)^2 - (\nabla_\mu \nabla_\nu \phi)^2], \quad (1.157)$$

$$\mathcal{L}_5 = G_5(\phi, X) G_{\mu\nu} \nabla^\mu \nabla^\nu \phi - \frac{1}{6} G_{5X}(\phi, X) \left[-3 \square \phi (\nabla_\mu \nabla_\nu \phi)^2 + (\square \phi)^3 + 2 (\nabla_\mu \nabla_\nu \phi)^3 \right]. \quad (1.158)$$

Here, $X = -\frac{1}{2} \nabla^\mu \nabla_\mu \phi$ is the kinetic term; K , G_3 , G_4 , and G_5 are generic functions of the scalar field and of the kinetic term; finally, $G_{i\phi}$ and G_{iX} ,

with $i = 3, 4, 5$, are the derivatives of the function G_i with respect to ϕ and X respectively. Depending on the value these functions assume, we have different theories of gravity.

We do not report all the calculations for determining the PPNs in the Horndeski's model⁵; however we should remember that, in order to obtain the post-Newtonian limit, a perturbative expansion of the field equations⁶ is done around the asymptotic values of the gravitational variables ($\eta_{\mu\nu}$ for the metric tensor, and ϕ_0 for the scalar field)

$$g_{\mu\nu} = \eta_{\mu\nu} + h_{\mu\nu}, \quad \phi = \phi_0 + \psi, \quad (1.159)$$

and consequently,

$$X = -\frac{1}{2}\nabla^\mu\psi\nabla_\mu\psi. \quad (1.160)$$

In doing so, one must also consider Taylor's expansions of the Horndeski functions

$$K(\phi, X) = \sum_{m,n=0}^{\infty} K_{(m,n)}\psi^m X^n, \quad (1.161)$$

with

$$K_{(m,n)} = \frac{1}{m!n!} \left. \frac{\partial^{m+n}}{\partial\phi^m\partial X^n} K(\phi, X) \right|_{\phi=\phi_0, X=0}, \quad (1.162)$$

and analogously for the $G_i(\phi, X)$ functions.

Furthermore, a gauge besides the standard one (as specified in Will's rules, step 8) can be set. In [45], the author chooses

$$h_{ij,j} - \frac{1}{2}h_{jj,i} + \frac{1}{2}h_{00,i} = \frac{G_{4(1,0)}}{G_{4(0,0)}}\psi_{,i}, \quad h_{0j,j} + \frac{1}{2}h_{jj,0} = \frac{G_{4(1,0)}}{G_{4(0,0)}}\psi_{,0}. \quad (1.163)$$

Then, by applying all of Will's rules, we obtain the following expressions for the PPN parameters in Horndeski's theory

$$\gamma_H = \frac{\omega_H + 1}{\omega_H + 2}, \quad (1.164)$$

$$\beta_H = 1 + \frac{\omega_H + \tau - 4\sigma\omega_H}{4(\omega_H + 2)^2(2\omega + 3)}, \quad (1.165)$$

$$\alpha_1 = \alpha_2 = \alpha_3 = \zeta_1 = \zeta_2 = \zeta_3 = \zeta_4 = \xi = 0, \quad (1.166)$$

⁵For this, we refer to [45].

⁶Horndeski's field equations are entirely reported in the appendix of Ref. [46]

where

$$\omega_H = \frac{G_{4(0,0)}}{2G_{4(1,0)}^2} [K_{(0,1)} - 2G_{3(1,0)}], \quad (1.167)$$

$$\sigma = \frac{G_{4(0,0)}G_{4(2,0)}}{G_{4(1,0)}^2}, \quad (1.168)$$

$$\tau = \frac{G_{4(0,0)}^2}{2G_{4(1,0)}^3} [K_{(1,1)} - 4G_{3(2,0)}]. \quad (1.169)$$

Scalar Tensor theory

Scalar tensor theories have been introduced primarily as dark energy - free cosmological models and in the investigation of unification schemes such as strings. They can be treated as a limiting case of Horndeski's, with a proper choice of the characteristic functions. Specifically, if we select

$$X = -\frac{(\partial\phi)^2}{2}, \quad (1.170)$$

$$K(\phi, X) = \frac{\omega(\phi)}{\phi}X + \lambda(\phi)\phi, \quad (1.171)$$

$$G_4(\phi, X) = \frac{\phi}{2}, \quad (1.172)$$

$$G_3(\phi, X) = G_5(\phi, X) = 0, \quad (1.173)$$

Eq. (1.154) becomes

$$\mathcal{A}_{\text{ST}} = \frac{1}{16\pi} \int [\phi R - \phi^{-1}\omega(\phi)g^{\mu\nu}\phi_{,\mu}\phi_{,\nu} + 2\phi\lambda(\phi)] \sqrt{-g}d^4x + \mathcal{A}_m. \quad (1.174)$$

Here, the metric $g_{\mu\nu}$ and the scalar field ϕ are two dynamic gravitational variables; there are also two arbitrary functions of the scalar field, the coupling function $\omega(\phi)$ and the cosmological one⁷ $\lambda(\phi)$.

By varying with respect to $g_{\mu\nu}$ and ϕ , we get the following field equations, respectively

$$\begin{aligned} R_{\mu\nu} - \frac{1}{2}g_{\mu\nu}R - \lambda(\phi)g_{\mu\nu} &= 8\pi\phi^{-1}T_{\mu\nu} + \phi^{-1}(\phi_{;\mu\nu} - g_{\mu\nu}\square_g\phi) + \\ &+ \phi^{-2}\omega(\phi)\left(\phi_{,\mu}\phi_{,\nu} - \frac{1}{2}g_{\mu\nu}\phi_{,\lambda}\phi^{,\lambda}\right), \end{aligned} \quad (1.175)$$

⁷Will assumes $\lambda(\phi) = 0$.

$$\square_g \phi + \frac{1}{2} \phi_{,\mu} \phi^{,\mu} \frac{d}{d\phi} \ln \left(\frac{\omega(\phi)}{\phi} \right) + \frac{1}{2} \frac{\phi}{\omega(\phi)} \left[R + 2 \frac{d}{d\phi} (\phi \lambda(\phi)) \right] = 0. \quad (1.176)$$

To achieve the post-Newtonian expansion, we must fix the asymptotic values of the gravitational variables. We choose $g_{\mu\nu}$ asymptotically flat, while we denote with ϕ_0 the asymptotic value of ϕ , just like in Horndeski's theory. ϕ_0 is related to the current value of G

$$G_{\text{today}} \equiv \phi_0^{-1} \left(\frac{4 + 2\omega_0}{3 + 2\omega_0} \right) = 1, \quad \omega_0 = \omega(\phi_0), \quad (1.177)$$

in geometrized units. Eq. (1.177) suggests that if ϕ_0 varied over time, this could lead to a variation of G . With these considerations in mind, we implement the other Will's rules to obtain the metric tensor corrections

$$g_{00} = -1 + 2U - 2(1 + \Lambda)U^2 + 4 \left(\frac{3 + 2\omega_0}{4 + 2\omega_0} \right) \Phi_1 + 4 \left(\frac{1 + 2\omega_0}{4 + 2\omega_0} - \Lambda \right) \Phi_2 + 2\Phi_3 + 6 \left(\frac{1 + \omega_0}{2 + \omega_0} \right) \Phi_4, \quad (1.178)$$

$$g_{0j} = -\frac{1}{2} \left(\frac{10 + 7\omega_0}{2 + \omega_0} \right) V_j - \frac{1}{2} W_j, \quad (1.179)$$

$$g_{ij} = \left[1 + 2 \left(\frac{1 + \omega_0}{2 + \omega_0} \right) \right], \quad (1.180)$$

where

$$\Lambda = \frac{\omega'_0}{(3 + 2\omega_0)^2 (4 + 2\omega_0)}, \quad \omega'_0 = \left. \frac{d\omega}{d\phi} \right|_{\phi_0}. \quad (1.181)$$

By applying the step 9, we finally get the PPN parameters for a scalar tensor theory

$$\gamma = \frac{1 + \omega_0}{2 + \omega_0}, \quad \beta = 1 + \Lambda, \quad \xi = 0, \\ \alpha_1 = \alpha_2 = \alpha_3 = \zeta_1 = \zeta_2 = \zeta_3 = \zeta_4 = 0, \quad (1.182)$$

Brans-Dicke theory

Brans-Dicke theory is a particular scalar tensor theory with $\omega \equiv \omega_{BD} = \text{constant}$ and $\lambda(\phi) = 0$. Consequently, it can also be considered as a subclass of the broader Horndeski model. In fact, if we choose

$$K(\phi, X) = \frac{\omega_{BD}}{\phi} X, \quad G_4(\phi, X) = \frac{\phi}{2}, \quad G_3(\phi, X) = G_5(\phi, X) = 0 \quad (1.183)$$

we get, from Eq. (1.154), the Brans-Dicke action

$$\mathcal{A} = \frac{1}{16\pi} \int [\phi R - \phi^{-1} \omega_{BD} g^{\mu\nu} \phi_{,\mu} \phi_{,\nu}] \sqrt{-g} d^4x + \mathcal{A}_m. \quad (1.184)$$

While Horndeski and scalar tensor theories are among the most general approaches to generalize Einstein's gravity, the Brans-Dicke model was initially proposed to include the Mach principle within GR. Even though the model is theoretically significant, it seems to fail within experimental considerations. Besides experimental considerations, we work out, in this case, with $\Lambda = 0$, having the PPN parameters as

$$\begin{aligned} \gamma &= \frac{1+\omega_{BD}}{2+\omega_{BD}}, \quad \beta = 1, \quad \xi = 0, \\ \alpha_1 = \alpha_2 = \alpha_3 = \zeta_1 = \zeta_2 = \zeta_3 = \zeta_4 &= 0. \end{aligned} \quad (1.185)$$

$f(R)$ theory

Extended theories of gravity are built up through effective Lagrangians and can present higher-order terms in curvature invariants that could mimic the exotic behavior of matter [47, 48, 49, 50, 51, 52, 53]. In principle, they are extensions of Einstein's theory where GR is a particular case or it is recovered as soon as higher-order terms reduce to R . Here we consider a straightforward extension which is $f(R)$ gravity in the metric formalism [47, 54]. This theory might be considered as a limiting case of the Horndeski's model as well. It is easy to show that by taking

$$\phi = \partial_R f(R), \quad (1.186)$$

$$K = -\frac{1}{2}(\phi R - f(R)), \quad (1.187)$$

$$G_4(\phi, X) = \frac{\phi}{2}, \quad (1.188)$$

$$G_3(\phi, X) = G_5(\phi, X) = 0, \quad (1.189)$$

we get, from Eq. (1.154), the $f(R)$ action

$$\mathcal{A}_{f(R)} = \int d^4x \sqrt{-g} f(R) + \mathcal{A}_m, \quad (1.190)$$

where $f(R)$ is a generic function of the curvature scalar R , g is the determinant of the metric tensor and \mathcal{A}_m is the action of standard matter minimally

coupled to gravity.

Varying with respect to the metric implies the following fourth-order field equations [55, 56]

$$G_{\mu\nu} = \frac{1}{f_R(R)} \left\{ \frac{1}{2} g_{\mu\nu} [f(R) - R f_R(R)] + f_R(R)_{;\mu\nu} - g_{\mu\nu} \square f_R(R) \right\} + \frac{T_{\mu\nu}^{(m)}}{f_R(R)}, \quad (1.191)$$

where $T_{\mu\nu}^{(m)}$ is the stress-energy tensor of ordinary matter. The right hand side of (1.191) can be regarded as an effective stress-energy tensor $T_{\mu\nu}^{(eff)}$, given by the sum of $T_{\mu\nu}^{(m)}$ and a *curvature fluid* energy-momentum tensor $T_{\mu\nu}^{(curv)}$, sourcing the effective Einstein equations⁸.

However, one of the simplest techniques for obtaining PPN parameters in metric theory $f(R)$ is to avoid perturbing these equations and instead to apply the analogy to scalar-tensor theories via conformal transformations. [42, 57]. Indeed, the two different approaches, i.e. the standard one in Ref. [42] and the alternative in Ref. [57], appear equivalent. Thus, following this approach, one reaches the advantage of avoiding complicated manipulations, by means of conformal transformations only.

Particularly, one can start with the following action

$$\mathcal{A} = \int [\phi R - \phi^{-1} \omega(\phi) g^{\mu\nu} \phi_{;\mu} \phi_{;\nu} - \phi^2 V(\phi)] \sqrt{-g} dx^4 + \mathcal{A}_m, \quad (1.192)$$

$$\mathcal{A} = \int [\phi R - \phi^{-1} \omega(\phi) g^{\mu\nu} \phi_{;\mu} \phi_{;\nu} - \phi^2 V(\phi)] \sqrt{-g} dx^4 + \mathcal{A}_m, \quad (1.193)$$

where ϕ is the scalar field, $\omega(\phi)$ the coupling function, $V(\phi)$ the scalar potential and \mathcal{A}_m the matter action. It is analogous to the scalar field action

$$\mathcal{A} = \int \left[F(\tilde{\phi}) R + \frac{1}{2} g^{\mu\nu} \tilde{\phi}_{;\mu} \tilde{\phi}_{;\nu} - V(\tilde{\phi}) \right] \sqrt{-g} dx^4 + \mathcal{A}_m, \quad (1.194)$$

if we perform the following transformation

$$\phi = F(\tilde{\phi}), \quad (1.195)$$

$$\omega(\phi) = -\frac{F(\tilde{\phi})}{2F'^2(\tilde{\phi})}. \quad (1.196)$$

⁸This interpretation is based on the fact that further degrees of freedom coming from higher-order gravity can be recast as an effective perfect fluid which reduces to the standard energy-matter one as soon as GR is recovered. For a rigorous demonstration, see [58, 59].

Once clarified this point, from now on we indicate with ϕ the scalar field for both the two formalisms. It is straightforward to obtain the following equations for the PPN parameters

$$\gamma_W = \frac{1 + \omega}{2 + \omega}, \quad (1.197)$$

$$\beta_W = 1 + \frac{\lambda}{(4 + 2\omega)}, \quad (1.198)$$

where $\omega = \omega(\phi)$ and

$$\lambda = \frac{\phi d\omega/d\phi}{(3 + 2\omega)(4 + 2\omega)}. \quad (1.199)$$

Instead, using the second Lagrangian, we have

$$\gamma_{CT} = -\frac{F'^2(\phi)}{F(\phi) + 2F'^2(\phi)} + 1, \quad (1.200)$$

$$\beta_{CT} = \frac{1}{4} \frac{F(\phi)F'(\phi)}{(2F(\phi) + 3F'^2(\phi))} \frac{d\gamma_{CT}}{d\phi} + 1. \quad (1.201)$$

To verify that these PPN parameters are the same, let us go into the Einstein frame, where matter is coupled to geometry through a function (called “coupling function”)⁹ $A(\psi)$. Let us define the following function

$$\alpha(\psi) = \frac{d \ln A(\psi)}{d\psi}, \quad (1.202)$$

establishing a measure of the coupling in the Einstein frame between the scalar field and matter as an effect of the conformal transformation.

PPN parameters can be written in terms of α as

$$\gamma_{CT} = -\frac{2\alpha^2}{(1 + \alpha^2)^2} + 1 = \frac{1 - \alpha^2}{1 + \alpha^2}, \quad (1.203)$$

$$\beta_{CT} = \frac{1}{2} \frac{\alpha^2}{(1 + \alpha^2)^2} \frac{d\alpha}{d\psi} + 1, \quad (1.204)$$

where $\alpha = \alpha(\psi)$.

On the other hand, it is possible to only define the conformal transformations

⁹In the Einstein frame we denote the scalar field with ψ to distinguish it from the Jordan frame.

between the Jordan frame and the Einstein frame by

$$\phi = A(\psi)^{-2}, \quad (1.205)$$

$$3 + 2\omega(\phi) = \alpha(\psi)^{-1}. \quad (1.206)$$

By substituting Eq. (1.206) into Eq. (1.197) we get

$$\gamma_W = \frac{1 + \omega}{2 + \omega} = \frac{\frac{1}{2\alpha^2} - \frac{3}{2} + 1}{\frac{1}{2\alpha^2} - \frac{3}{2} + 2} = \frac{1 - \alpha^2}{1 + \alpha^2}, \quad (1.207)$$

where $\omega = \omega(\phi)$ and $\alpha = \alpha(\psi)$. Therefore, $\gamma_W \equiv \gamma_{CT}$. To calculate β_W , let us start by replacing Eq. (1.206) into Eq. (1.198), obtaining

$$\beta_W = \frac{\alpha^6}{(1 + \alpha^2)^2} \phi \frac{d\omega}{d\phi} + 1. \quad (1.208)$$

But, observing that, from Eq. (1.205), we have

$$\frac{d\psi}{d\phi} = -\frac{A(\psi)^3}{2} \left(\frac{dA(\psi)}{d\psi} \right)^{-1}, \quad (1.209)$$

and that we can rewrite Eq. (1.202) as

$$\alpha(\psi) = \frac{1}{A(\psi)} \frac{dA(\psi)}{d\psi}, \quad (1.210)$$

we get

$$\begin{aligned} \frac{d\omega(\phi)}{d\phi} &= \frac{d}{d\phi} \left(\frac{1}{2\alpha(\psi)^2} - \frac{3}{2} \right) = \frac{1}{2} \frac{d\psi}{d\phi} \frac{d}{d\psi} (\alpha(\psi)^{-2}) = \\ &= \frac{A(\psi)^3}{2\alpha(\psi)^3} \frac{d\alpha(\psi)}{d\psi} \left(\frac{dA(\psi)}{d\psi} \right)^{-1}. \end{aligned} \quad (1.211)$$

Thus

$$\phi \frac{d\omega(\phi)}{d\phi} = \frac{1}{2\alpha(\psi)^3} A(\psi) \left(\frac{dA(\psi)}{d\psi} \right)^{-1} \frac{d\alpha(\psi)}{d\psi} = \frac{1}{2\alpha(\psi)^4} \frac{d\alpha(\psi)}{d\psi}, \quad (1.212)$$

and

$$\beta_W = \frac{\alpha^6}{(1 + \alpha^2)^2} \phi \frac{d\omega}{d\phi} + 1 = \frac{1}{2} \frac{\alpha^2}{(1 + \alpha^2)^2} \frac{d\alpha}{d\psi} \quad (1.213)$$

which coincides with β_{CT} .

Finally, a further transformation to rewrite the PPN parameters of Eqs. (1.200) - (1.201) in terms of $df(R)/dR$ gives us

$$\gamma - 1 = -\frac{f''(R)^2}{f'(R) + 2f''(R)^2}, \quad (1.214)$$

$$\beta - 1 = \frac{1}{4} \frac{f'(R)f''(R)}{2f'(R) + 3f''(R)^2} \frac{d\gamma}{dR}, \quad (1.215)$$

and with all the other PPN parameters fix to zero.

These are the expressions for the PPN parameters in metric $f(R)$ theory [57, 60].

1.3.3 Vector Tensor theory

One of the main goals of modern physics is to unify all nature's forces into a single scheme. The Standard Model Extension (SME) is a field theory that combines the Standard Model (SM) of particle physics and GR. The spontaneous Lorentz symmetry breaking is a key aspect of the SME. The vector tensor theories were developed to explain how the LLI could be violated in the gravitational scenario.

A general vector tensor theory can be described by the following action

$$\begin{aligned} \mathcal{A}_{\text{VT}} = & \frac{1}{16\pi} \int [R + \omega K_\mu K^\mu R + \eta K^\mu K^\nu R_{\mu\nu} - \epsilon F_{\mu\nu} F^{\mu\nu} + \\ & + \tau K_{\mu;\nu} K^{\mu;\nu}] \sqrt{-g} d^4 + \mathcal{A}_m, \end{aligned} \quad (1.216)$$

with

$$F_{\mu\nu} = K_{\nu;\mu} - K_{\mu;\nu}, \quad (1.217)$$

and \mathcal{A}_m the matter action, as always. Here, we have two gravitational variables, the metric $g_{\mu\nu}$ and the dynamical (time-like) vector field K^μ . Furthermore, ω , η , ϵ , and τ are arbitrary parameters; while K is a cosmological parameter.

The field equations, obtained through the variational principle, are

$$R_{\mu\nu} - \frac{1}{2} g_{\mu\nu} R + \omega \Theta_{\mu\nu}^{(\omega)} + \epsilon \Theta_{\mu\nu}^{(\epsilon)} + \eta \Theta_{\mu\nu}^{(\eta)} + \tau \Theta_{\mu\nu}^{(\tau)} = 8\pi T_{\mu\nu}, \quad (1.218)$$

$$\epsilon F_{;\nu}^{\mu\nu} + \frac{1}{2} \tau K_{;\nu}^{\mu;\nu} - \frac{1}{2} \omega K^\mu R - \frac{1}{2} \eta K^\nu R_\nu^\mu = 0, \quad (1.219)$$

where

$$\Theta_{\mu\nu}^{(\omega)} = K_\mu K_\nu R + K^2 R_{\mu\nu} - \frac{1}{2} g_{\mu\nu} K^2 R - (K^2)_{;\mu\nu} + g_{\mu\nu} \square_g K^2, \quad (1.220)$$

$$\Theta_{\mu\nu}^{(\epsilon)} = -2(F_\mu^\alpha F_{\nu\alpha}) - \frac{1}{4} g_{\mu\nu} (F_{\alpha\beta} F^{\alpha\beta}), \quad (1.221)$$

$$\begin{aligned} \Theta_{\mu\nu}^{(\eta)} &= 2K^\alpha K_{(\mu} R_{\nu)\alpha} - \frac{1}{2} g_{\mu\nu} K^\alpha K^\beta R_{\alpha\beta} - (K^\alpha K_{(\mu})_{;\nu)\alpha} + \\ &\quad + \frac{1}{2} \square_g (K_\mu K_\nu) + \frac{1}{2} g_{\mu\nu} (K^\alpha K^\beta)_{;\alpha\beta}, \end{aligned} \quad (1.222)$$

$$\begin{aligned} \Theta_{\mu\nu}^{(\tau)} &= K_{\mu;\alpha} K_\nu^{;\alpha} + K_{\alpha;\mu} K_{;\nu}^\alpha - \frac{1}{2} g_{\mu\nu} K_{\alpha;\beta} K^{\alpha;\beta} + \\ &\quad + (K^\alpha K_{(\mu;\nu)} - K_{;\mu}^\alpha K_\nu) - K_{(\mu} K_{\nu}^{;\alpha})_{;\alpha}, \end{aligned} \quad (1.223)$$

and

$$K^2 = K_\mu K^\mu. \quad (1.224)$$

Despite the complexity of Eq. (1.218), the stress-energy conservation can be verified. However, by taking the divergence of Eq. (1.219), we get the restriction

$$\tau K_{;\nu\mu}^{\mu;\nu} - (\omega K^\mu R + \eta K^\nu R_{\nu}^\mu)_{;\mu} = 0, \quad (1.225)$$

which tells us that the vector field solution is constrained. This is attributable to the fact that the action is not invariant under the transformation

$$K_\mu \rightarrow K_\mu + \lambda_{,\mu}, \quad (1.226)$$

with λ scalar function.

Taking these constraints into account, we follow Will's procedure for calculating the PPN parameters. Specifically, we first adapt Eqs. (1.135) - (1.137) from step 3 to this case

$$g_{\mu\nu} = \eta_{\mu\nu} + h_{\mu\nu}, \quad K_\mu = K \delta_\mu^0 + k_\mu. \quad (1.227)$$

As in the theories analyzed above, Minkowski's metric is the asymptotic value for $g_{\mu\nu}$; whereas, for the vector field K_μ , we denote this value with $K \delta_\mu^0$, where K can vary on cosmological time scales.

Within the limitations of an action that is not fully gauge invariant, we choose¹⁰

$$h_{,\nu}^{\alpha\nu} - \frac{1}{2}h^{,\alpha} = 0. \quad (1.228)$$

Then, as is usual, we perturbatively solve field equations up to the post-Newtonian order to derive the PPN parameters for the vector tensor theory

$$\gamma = \frac{1 + K^2[\omega - 2\omega(2\omega + \eta - \tau)/(2\epsilon - \tau)]}{1 - K^2[\omega + 8\omega^2/(2\epsilon - \tau)]}, \quad (1.229)$$

$$\beta = \frac{1}{4}(3 + \gamma) + \frac{1}{2}\sigma[1 + \gamma(\gamma - 2)/G], \quad (1.230)$$

$$\xi = 0, \quad (1.231)$$

$$\alpha_1 = 4(1 - \gamma)[1 - (2\epsilon - \tau)\Delta] + 4\omega K^2 \Delta a, \quad (1.232)$$

$$\alpha_2 = 3(1 - \gamma) \left[1 - \frac{2}{3}(2\epsilon - \tau)\Delta \right] + 2\omega K^2 \Delta a - \frac{1}{2}bK^2/G, \quad (1.233)$$

$$\alpha_3 = \zeta_1 = \zeta_2 = \zeta_3 = \zeta_4 = 0. \quad (1.234)$$

Here

$$\sigma = \frac{(1 - \omega K^2)(2\omega - \eta + 2\epsilon)}{(1 - \omega K^2)(2\epsilon - \tau) - 8\omega^2 K^2}, \quad (1.235)$$

$$\Delta = \left\{ (2\epsilon - \tau)[1 - K^2(\omega + \eta - \tau)] + \frac{1}{2}(\eta - \tau)^2 K^2 \right\}^{-1}, \quad (1.236)$$

$$a = (2\epsilon - \tau)(3\gamma - 1) - 2(\eta - \tau)(2\gamma - 1), \quad (1.237)$$

$$b = \begin{cases} (2\omega + \eta - \tau)[(2\gamma - 1)(\gamma + 1) + \sigma(\gamma - 2)], \\ -(2\gamma - 1)^2(2\omega + \eta)[1 - \tau^{-1}(2\omega + \eta)], & \text{if } \tau \neq 0, \\ 0, & \text{if } \tau = 0, \end{cases} \quad (1.238)$$

and G is related to the present value of the gravitational constant

$$G_{\text{today}} \equiv G \left[\frac{1}{2}(\gamma + 1) + \frac{3}{2}\omega K^2(\gamma - 1) - \frac{1}{2}(\eta - \tau)K^2(1 + \sigma) \right]^{-1} = 1 \quad (1.239)$$

in geometrized units.

¹⁰Again, we use $\eta_{\mu\nu}$ to lower and raise the indices of the corrective terms $h_{\mu\nu}$ and k_μ .

1.3.4 Final remarks

Each PPN parameter has a specific meaning (see Tab. 1.1 in Sec. 1.2.2). By examining the values of a theory's PPN parameters, we may determine both its physical properties and whether or not it deviates from GR (which is characterized by $\gamma = \beta = 1$, with all the others equal to zero).

In particular, α_1 , α_2 , and α_3 show the presence of preferred - frame effects. As a result, if at least one of these α_i is non-zero, the theory is a *preferred - frame theory*. Rather, the parameters ζ_1 , ζ_2 , ζ_3 , ζ_4 , and α_3 indicate possible violations of total momentum conservation. The theory is *conservative* if all of these parameters are null. If there are five free PPN parameters (γ , β , ξ , α_1 , α_2), conservative theories are classified as *semi - conservative*; if there are three free PPN parameters (γ , β , ξ), they are classified as *fully conservative*. Based on these considerations, we can conclude that GR and scalar tensor theories are fully conservative and do not exhibit any preferred - frame effects ($(\alpha_i = \zeta_i = 0)$). These theories hence satisfy the SEP and can be tested, for example, to confirm its validity in the Solar System.

The same cannot be said a priori for vector tensor theories. They are semi-conservative ($\alpha_3 = \zeta_i = 0$) and can have preferred - frame effects since at least one amongst α_1 and α_2 is different from zero. This suggests that we might use vector tensor theories to detect SEP violations even in the Solar System (albeit unlikely).

The experimental measurement of PPN parameters, for example, via LR missions (see Sec. 4.1), would allow us to constrain some free parameters of the theory under investigation and “fit” it to the weak field, specifically the Solar System. However, in order to carry out a rigorous and complete test of the theoretical model, further constraints must be imposed using the strong field conditions. But, as we will show in the next sections, this is not achievable using the post-Newtonian approximation.

1.4 Equations of motion in the PPN formalism

We have seen that the final step in determining the PPN parameters of a theory is to compare the perturbative expansion of its metric tensor to the standard one of the WN formalism by equating the coefficients of equal potentials. However, it is possible that the metric tensor expansion of the new

theory has more potentials than those of the WN formalism. This occurs, for example, in the $f(R)$ theory but, in this case, the PPN parameters were computed using the analogy with the scalar tensor theory. Other theoretical models, such as $f(R)$ theory in Palatini formalism, cannot be treated in the same way [41]. Hence, what are our possible alternatives? Since we do not know how to deal with these new potentials, we proceed to the equations of motion calculation in the PPN formalism, as we did previously for the field equations.

Let us consider a system consisting of massive bodies. From now on, we denote with the subscript a all the quantities relating to the a th body.

The starting point is the conservation of the rest - mass (or baryon number) density¹¹

$$(\rho_0 u^\alpha)_{;\alpha} = (1 - \sqrt{-g})(1 - \sqrt{-g}\rho_0 u^\alpha)_{,\alpha} = 0. \quad (1.240)$$

If we define a new density ρ^* (called “conserved density”), we can reformulate Eq. (1.240) as the continuity equation

$$\begin{aligned} \rho^* &\equiv \rho_0 \left(1 + \frac{1}{2}v^2 + 3\gamma U\right) = \\ &= \rho_0 u^0 \sqrt{-g} + O(\rho_0 \epsilon^4). \end{aligned} \quad (1.241)$$

Now we can introduce the inertial mass of the body

$$m_a \doteq \int_a \rho^* \left(1 + \frac{1}{2}\bar{v}^2 - \frac{1}{2}U + \Pi\right) d^3x, \quad (1.242)$$

where

$$\bar{\mathbf{v}} \equiv \mathbf{v} - \mathbf{v}_{a(0)}, \quad \mathbf{v}_{a(0)} \equiv \int_a \rho^* \mathbf{v} d^3x, \quad (1.243)$$

and, consequently, the center of inertial mass

$$\mathbf{x}_a \doteq \frac{1}{m_a} \int_a \rho^* \left(1 + \frac{1}{2}\bar{v}^2 - \frac{1}{2}U + \Pi\right) \mathbf{x} d^3x. \quad (1.244)$$

This last equation enables us to determine the body’s velocity and acceleration. Specifically, using Eq. (1.241) and the conservation of local stress-energy

$$T_{;\nu}^{\mu\nu} = 0, \quad (1.245)$$

¹¹Remember that it is constituted by a perfect fluid in the WN formalism.

we get

$$\mathbf{v}_a \equiv \frac{d\mathbf{x}_a}{dt} = \frac{1}{m_a} \int_a \left[\rho^* \left(1 + \frac{1}{2} \bar{v}^2 - \frac{1}{2} U + \Pi \right) \mathbf{v} + p \bar{\mathbf{v}} - \frac{1}{2} \rho^* \bar{\mathbf{W}} \right] d^3x, \quad (1.246)$$

with

$$\bar{\mathbf{W}}_j = \int_a \rho' \frac{\bar{\mathbf{v}}' \cdot (\mathbf{x} - \mathbf{x}') (x_j - x'_j)}{|\mathbf{x} - \mathbf{x}'|^3} d^3x'. \quad (1.247)$$

Therefore

$$\begin{aligned} \mathbf{a}_a \equiv \frac{d\mathbf{v}_a}{dt} = & \frac{1}{m_a} \left\{ \int_a \rho^* \left(1 + \frac{1}{2} \bar{v}^2 - \frac{1}{2} U + \Pi \right) \left(\frac{d\mathbf{v}}{dt} \right) d^3x + \right. \\ & v_a^j \int_a p_j \bar{\mathbf{v}} d^3x + \int_a [p_{,0} \bar{\mathbf{v}} - (p/\rho^*) \nabla p] d^3x + \\ & \left. - \frac{1}{2} \left(\frac{d}{dt} \right) \int_a \rho^* \bar{\mathbf{W}} d^3x + \frac{1}{2} \mathcal{T}_a - \frac{1}{2} \mathcal{T}_a^* + \mathcal{P}_a \right\}. \end{aligned} \quad (1.248)$$

The last three terms

$$\mathcal{T}_a^j = \int_a \frac{\rho^* \rho^{*'} \bar{v}'^j \bar{\mathbf{v}}' \cdot (\mathbf{x} - \mathbf{x}')}{|\mathbf{x} - \mathbf{x}'|^3} d^3x d^3x', \quad (1.249)$$

$$\mathcal{T}_a^{*j} = \int_a \frac{\rho^* \rho^{*'} \bar{v}^j \bar{\mathbf{v}}' \cdot (\mathbf{x} - \mathbf{x}')}{|\mathbf{x} - \mathbf{x}'|^3} d^3x d^3x', \quad (1.250)$$

$$\mathcal{P}_a^j = \int_a \frac{\rho^* \rho' (x - x')^j}{|\mathbf{x} - \mathbf{x}'|^3} d^3x d^3x' \quad (1.251)$$

depend only by the internal structure of the *ath* body.

To obtain the final expression of acceleration, we must solve the integrals in Eq. (1.248). We can make some simplifications. In the Solar System, internal structure variations of the Sun and planets occur in time scales significantly longer than their orbital periods. As a result, we can set equal to zero the total time derivatives of those terms that depend only on the internal structure of the body. Furthermore, by using the PPN approximations of the stress-energy tensor, Eqs. (1.128) - (1.130), we can derive the post-Newtonian

Euler equation from Eq. (1.245)

$$\begin{aligned}
\rho^* \frac{dv^j}{dt} &= \rho^* U_{,j} - [p(1 + 3\gamma U)]_{,j} + p_{,j} \left(\frac{1}{2} v^2 + \Pi + \frac{p}{\rho^*} \right) + \\
&- \rho^* \frac{d}{dt} \left[(2\gamma + 2) U v^j - \frac{1}{2} (4\gamma + 4 + \alpha_1) V^j - \frac{1}{2} \alpha_1 U w^j \right] + \\
&v^j (\rho^* U_{,0} - p_{,0}) - \frac{1}{2} (1 + \alpha_2 + \zeta_1 + 2\xi) \rho^* (V^j - W^j)_{,0} + \\
&- \frac{1}{2} \rho^* [(4\gamma + 4 + \alpha_1) v^k + (\alpha_1 - 2\alpha_3) w^k] V_{k,j} + \\
&+ \rho^* \frac{\partial}{\partial x^j} \left[\Phi - \xi \Phi_W - \frac{1}{2} (\zeta_1 - 2\xi) \mathcal{A} - \frac{1}{2} \alpha_2 w^i w^k U_{ik} + \right. \\
&\left. + \alpha_2 w^k (V_k - W_k) \right] + \\
&+ \rho^* U_{,j} \left[\gamma v^2 - \frac{1}{2} \alpha_1 \mathbf{w} \cdot \mathbf{v} + \frac{1}{2} (\alpha_2 + \alpha_3 - \alpha_1) w^2 + \right. \\
&\left. - (2\beta - 2) U + \frac{3\gamma p}{\rho^*} \right], \tag{1.252}
\end{aligned}$$

where \mathbf{w} is the relative velocity between two different frames, and

$$\begin{aligned}
\Phi &= \frac{1}{2} (2\gamma + 2 + \alpha_3 + \zeta_1 - 2\xi) \Phi_1 + (3\gamma - 2\beta + 1 + \zeta_2 + \xi) \Phi_2 + \\
&+ (1 + \zeta_3) \Phi_3 + (3\gamma + 3\zeta_4 - 2\xi) \Phi_4. \tag{1.253}
\end{aligned}$$

Therefore, applying the appropriate simplifications and considering Eq. (1.252), we have the equations of motion for a body of mass m_a

$$\mathbf{a}_a = \mathbf{a}_{a,self} + \mathbf{a}_{a,Newt} + \mathbf{a}_{a,nbody}, \tag{1.254}$$

with

$$\begin{aligned}
a_{a,self}^j &= -\frac{1}{m_a} \left[\frac{1}{2} (\alpha_3 + \zeta_1) t_a^j + \zeta_1 \left(\mathcal{T}_a^j - \frac{3}{2} \mathcal{T}_a^{**j} \right) + \right. \\
&\quad \left. + \zeta_2 \Omega_a^j + \zeta_3 \mathcal{E}_a^j + 3\zeta_4 \mathcal{P}_a^j \right] - \frac{\alpha_3}{m_a} (w + v_a)^k H_a^{kj}, \tag{1.255}
\end{aligned}$$

$$a_{a,Newt}^j = \frac{(m_P)_a^{jk}}{m_a} \mathfrak{A}_{,k}, \tag{1.256}$$

$$\begin{aligned}
a_{a,nbody}^j &= \sum_{b \neq a} \frac{m_b x_{ab}^j}{r_{ab}^3} \left\{ (2\gamma + 2\beta) \frac{m_b}{r_{ab}} + \left(2\gamma + 2\beta + 1 + \frac{\alpha_1}{2} - \zeta_2 \right) \frac{m_a}{r_{ab}} + \right. \\
&\quad + (2\beta - 1 - 2\xi - \zeta_2) \sum_{c \neq ab} \frac{m_c}{r_{bc}} + (2\gamma + 2\beta - 2\xi) \sum_{c \neq ab} \frac{m_c}{r_{ac}} - \frac{1}{2} (1 + \\
&\quad + 2\xi + \alpha_2 - \zeta_1) \sum_{c \neq ab} m_c \frac{\mathbf{x}_{ab} \cdot \mathbf{x}_{bc}}{r_{bc}^3} - \xi \sum_{c \neq ab} m_c \frac{\mathbf{x}_{bc} \cdot \mathbf{x}_{ac}}{r_{ac}^3} - \gamma v_a^2 + \\
&\quad + \frac{1}{2} (4\gamma + 4 + \alpha_1) \mathbf{v}_a \cdot \mathbf{v}_b - \frac{1}{2} (2\gamma + 2 + \alpha_2 + \alpha_3) v_b^2 + \frac{1}{2} (\alpha_1 - \alpha_2 + \\
&\quad - \alpha_3) w^2 + \frac{1}{2} \alpha_1 \mathbf{w} \cdot \mathbf{v}_a + \frac{3}{2} \alpha_2 (\mathbf{w} \cdot \hat{\mathbf{n}}_{ab})^2 + \frac{1}{2} (\alpha_1 - 2\alpha_2 + \\
&\quad - 2\alpha_3) \mathbf{w} \cdot \mathbf{v}_b + \frac{3}{2} (1 + \alpha_2) (\mathbf{v}_b \cdot \hat{\mathbf{n}}_{ab})^2 + 3\alpha_2 (\mathbf{w} \cdot \hat{\mathbf{n}}_{ab}) (\mathbf{v}_b \cdot \hat{\mathbf{n}}_{ab}) \left. \right\} + \\
&\quad - \frac{1}{2} (4\gamma + 3 - 2\xi + \alpha_1 - \alpha_2 + \zeta_1) \sum_{b \neq a} \frac{m_b}{r_{ab}} \sum_{c \neq ab} \frac{m_c x_{bc}^j}{r_{bc}^3} + \\
&\quad - \xi \sum_{b \neq a} \frac{m_b}{r_{ab}^3} (\delta_{jk} - 3\hat{\mathbf{n}}_{ab}^j \hat{\mathbf{n}}_{ab}^k) \sum_{c \neq ba} m_c \left(\frac{x_{ac}^k}{r_{ac}} - \frac{x_{bc}^k}{r_{bc}} \right) + \\
&\quad + \sum_{b \neq a} \frac{m_b}{r_{ab}^3} \mathbf{x}_{ab} \cdot [(2\gamma + 2)\mathbf{v}_a - (2\gamma + 1)\mathbf{v}_b] v_a^j + \\
&\quad - \frac{1}{2} \sum_{b \neq a} \frac{m_b}{r_{ab}^3} \mathbf{x}_{ab} \cdot [(4\gamma + 4 + \alpha_1)\mathbf{v}_a - (4\gamma + 2 + \alpha_1 - 2\alpha_2)\mathbf{v}_b + 2\alpha_2 \mathbf{w}] v_b^j + \\
&\quad - \frac{1}{2} \sum_{b \neq a} \frac{m_b}{r_{ab}^3} \mathbf{x}_{ab} \cdot [\alpha_1 \mathbf{v}_a - (\alpha_1 - 2\alpha_2)\mathbf{v}_b + 2\alpha_2 \mathbf{w}] w^j. \tag{1.257}
\end{aligned}$$

Here

$$\mathbf{x}_{ab} = \mathbf{x}_a - \mathbf{x}_b, \quad (1.258)$$

$$\hat{\mathbf{n}}_{ab} = \frac{\mathbf{x}_{ab}}{r_{ab}}, \quad (1.259)$$

$$r_{ab} = |\mathbf{x}_{ab}|, \quad (1.260)$$

$$t_a^j = \int_a \frac{\rho^* \rho^{*'} \bar{v}'^2 (x - x')^j}{|\mathbf{x} - \mathbf{x}'|^3} d^3x d^3x', \quad (1.261)$$

$$\mathcal{T}_a^{j**} = \int_a \frac{\rho^* \rho^{*'} [\bar{\mathbf{v}}' \cdot (\mathbf{x} - \mathbf{x}')]^2 (x - x')^j}{|\mathbf{x} - \mathbf{x}'|^5} d^3x d^3x', \quad (1.262)$$

$$\Omega_a^j = \int_a \frac{\rho^* \rho^{*'} \rho^{*''} (x - x')^j}{|\mathbf{x}' - \mathbf{x}''| |\mathbf{x} - \mathbf{x}'|^3} d^3x d^3x' d^3x'', \quad (1.263)$$

$$\mathcal{E}_a^j = \int_a \frac{\rho^* \rho^{*'} \Pi' (x - x')^j}{|\mathbf{x} - \mathbf{x}'|^3} d^3x d^3x', \quad (1.264)$$

$$H_a^{kj} = \int_a \frac{\rho^* \rho^{*'} \bar{v}'^k (x - x')^j}{|\mathbf{x} - \mathbf{x}'|^3} d^3x d^3x', \quad (1.265)$$

$$Q_a^{ij} = \int_b \rho (3\bar{x}^i \bar{x}^j - |\bar{\mathbf{x}}|^2 \delta^{ij}) d^3x. \quad (1.266)$$

The first six terms in Eq. (1.255), involving terms such as t_a^j , \mathcal{T}_a^j and so on, depend only on the internal structure of the *ath* massive body and thus represent “self-accelerations” of the body’s center of mass. Such self-accelerations are associated with breakdowns in conservation of total momentum, since they depend on the PPN conservation-law parameters α_3 , ζ_1 , ζ_2 , ζ_3 and ζ_4 . In any semiconservative theory of gravity $\alpha_1 = \zeta_1 = \zeta_2 = \zeta_3 = \zeta_4 = 0$ and these self-accelerations are absent. Also note that spherically symmetric bodies suffer no acceleration regardless of the theory of gravity, since for them the terms t_a^j , \mathcal{T}_a^j , \mathcal{T}_a^{**j} , Ω_a^j , \mathcal{E}_a^j and \mathcal{P}_a^j are identically zero. The same is true for a composite massive body made up of two bodies in a nearly circular orbit, when the self-acceleration is averaged over an orbital period. Thus, there is little hope of testing the existence of these terms in the Solar System. The next term in Eq. (1.255), $-m_a^{-1} \alpha_3 (w + v_a) H_a^{kj}$ is a self acceleration which involves the massive body’s motion relative to the universe rest frame. It depends on the conservation-law/preferred-frame parameter α_3 , which is zero in any semiconservative theory of gravity.

The next term, Eq. (1.256) is the quasi-Newtonian acceleration of the mas-

sive body. Here $(m_P)_a^{jk}$ is the “passive gravitational mass tensor” given by

$$(m_P)_a^{jk} = m_a \left\{ \delta^{jk} \left[1 + (4\beta - \gamma - 3 - 3\xi - \alpha_1 + \alpha_2 - \zeta_1) \frac{\Omega_a}{m_a} + \right. \right. \\ \left. \left. - 3\xi \hat{\mathbf{n}}_{ab}^l \hat{\mathbf{n}}_{ab}^m \frac{\Omega_a^{lm}}{m_a} \right] + (2\xi - \alpha_2 + \zeta_1 - \zeta_2) \frac{\Omega_a^{jk}}{m_a} \right\} \quad (1.267)$$

where

$$\Omega_a = -\frac{1}{2} \int_a \frac{\rho^* \rho^{*'}}{|\mathbf{x} - \mathbf{x}'|} d^3x d^3x'. \quad (1.268)$$

Furthermore, $\mathfrak{U}(\mathbf{x}_a)$ is the quasi-Newtonian potential, given by

$$\mathfrak{U}(\mathbf{x}_a) = \sum_{b \neq a} \frac{[m_A(\hat{\mathbf{n}}_{ab})]_b}{r_{ab}}, \quad (1.269)$$

where $[m_A(\hat{\mathbf{n}}_{ab})]_b$ is the “active gravitational mass” of the b th body, given by

$$[m_A(\hat{\mathbf{n}}_{ab})]_b = m_b \left\{ 1 + \left(4\beta - \gamma - 3 - 3\xi - \frac{\alpha_3}{2} - \frac{\zeta_1}{2} - 2\zeta_2 \right) \frac{\Omega_b}{m_b} + \right. \\ \left. + \zeta_3 \frac{E_b}{m_b} \left(\frac{3}{2} \alpha_3 + \zeta_1 - 3\zeta_4 \right) \frac{P_b}{m_b} + \right. \\ \left. + \frac{1}{2} (\zeta_1 - 2\xi) \hat{\mathbf{n}}_{ab}^j \hat{\mathbf{n}}_{ab}^k \frac{\Omega_b^{jk}}{m_b} \right\}, \quad (1.270)$$

with

$$P_a = \int_a p d^3x, \quad E_b = \int_a \rho^* \Pi d^3x. \quad (1.271)$$

In Newtonian theory, the active gravitational mass, the passive gravitational mass and the inertial mass are the same, hence each massive body’s acceleration is independent of its mass or structure¹². However, passive gravitational mass could not be exactly equal to inertial mass in a given metric theory of gravity; their difference depends on the PPN parameters and on the gravitational self energy (Ω and Ω^{jk}) of the body. This is interpreted as some sort of gravitational Weak Equivalence Principle breakdown, baptized “Nordtvedt effect”.

The remaining term, Eq. (1.257), is called the n-body term. It contains

¹²Clearly this is the “Equivalence Principle”.

the post-Newtonian corrections to the Newtonian equations of motion which would result from treating each body as a “point mass” moving along a geodesic of the PPN metric produced by all the other bodies, assumed to be point masses, taking account of certain post-Newtonian terms generated by the gravitational field of the body itself. It is the n-body acceleration which produces the “classical” perihelion shift of the planets, as well as a host of other effects. Let us now focus in detail what we expect for the classes of scalar tensor theories that extend GR, analyzed in Sec. 1.3. We will replace the PPNs of these theories into the just-determined Eqs. (1.255) - (1.257). In this way, we get the equations of motion for a body of mass m_a in every theoretical model.

Horndeski's theory

$$a_{a,self}^j = 0, \quad (1.272)$$

$$a_{a,Newt}^j = \frac{(m_P)_a^{jk}}{m_a} \mathfrak{A}_{,k}, \quad (1.273)$$

$$\begin{aligned} a_{a,nbody}^j = & \sum_{b \neq a} \frac{m_b x_{ab}^j}{r_{ab}^3} \left\{ 2 \left(\frac{3 + 2\omega_H}{2 + \omega_H} + \frac{\omega_H + \tau - 4\sigma\omega_H}{4(\omega_H + 2)^2(2\omega + 3)} \right) \frac{m_b}{r_{ab}} + \left(\frac{7 + 4\omega_H}{2 + \omega_H} + \right. \right. \\ & \left. \left. + \frac{\omega_H + \tau - 4\sigma\omega_H}{2(\omega_H + 2)^2(2\omega + 3)} \right) \frac{m_a}{r_{ab}} + \left(\frac{1 + \omega_H + \tau - 4\sigma\omega_H}{2(\omega_H + 2)^2(2\omega + 3)} + 1 \right) \sum_{c \neq ab} \frac{m_c}{r_{bc}} + \right. \\ & \left. + 2 \left(\frac{3 + 2\omega_H}{2 + \omega_H} + \frac{\omega_H + \tau - 4\sigma\omega_H}{4(\omega_H + 2)^2(2\omega + 3)} \right) \sum_{c \neq ab} \frac{m_c}{r_{ac}} - \frac{1}{2} \sum_{c \neq ab} m_c \frac{\mathbf{x}_{ab} \cdot \mathbf{x}_{bc}}{r_{bc}^3} + \right. \\ & \left. - \frac{1 + \omega_H}{2 + \omega_H} v_a^2 + 2 \left(\frac{3 + 2\omega_H}{2 + \omega_H} \right) \mathbf{v}_a \cdot \mathbf{v}_b - \frac{3 + 2\omega_H}{2 + \omega_H} v_b^2 + \frac{3}{2} (\mathbf{v}_b \cdot \hat{\mathbf{n}}_{ab})^2 \right\} + \\ & - \frac{1}{2} \left(\frac{10 + 7\omega_H}{2 + \omega_H} \right) \sum_{b \neq a} \frac{m_b}{r_{ab}} \sum_{c \neq ab} \frac{m_c x_{bc}^j}{r_{bc}^3} + \sum_{b \neq a} \frac{m_b}{r_{ab}^3} \mathbf{x}_{ab} \cdot \left[2 \left(\frac{3 + 2\omega_H}{2 + \omega_H} \right) \mathbf{v}_a + \right. \\ & \left. - \frac{4 + 3\omega_H}{2 + \omega_H} \mathbf{v}_b \right] (v_a^j - v_b^j), \quad (1.274) \end{aligned}$$

with

$$(m_P)_a^{jk} = m_a \delta^{jk} \left[1 + \left(\frac{\omega_H + \tau - 4\sigma\omega_H}{(\omega_H + 2)^2(2\omega_H + 3)} + \frac{1}{2 + \omega_H} \right) \frac{\Omega_a}{m_a} \right], \quad (1.275)$$

$$[m_A(\hat{\mathbf{n}}_{ab})]_b = m_b \left[1 + \left(\frac{\omega_H + \tau - 4\sigma\omega_H}{(\omega_H + 2)^2(2\omega_H + 3)} + \frac{1}{2 + \omega_H} \right) \frac{\Omega_b}{m_b} \right]. \quad (1.276)$$

Scalar tensor theory

$$a_{a,self}^j = 0, \quad (1.277)$$

$$a_{a,Newt}^j = \frac{(m_P)_a^{jk}}{m_a} \mathfrak{U}_{,k}, \quad (1.278)$$

$$\begin{aligned} a_{a,nbody}^j &= \sum_{b \neq a} \frac{m_b x_{ab}^j}{r_{ab}^3} \left\{ 2 \left(\frac{3 + 2\omega}{2 + \omega} + \Lambda \right) \frac{m_b}{r_{ab}} + \left(\frac{8 + 5\omega}{2 + \omega} + 2\Lambda \right) \frac{m_a}{r_{ab}} + \right. \\ &+ (1 + 2\Lambda) \sum_{c \neq ab} \frac{m_c}{r_{bc}} + 2 \left(\frac{3 + 2\omega}{2 + \omega} + \Lambda \right) \sum_{c \neq ab} \frac{m_c}{r_{ac}} + \\ &- \frac{1}{2} \sum_{c \neq ab} m_c \frac{\mathbf{x}_{ab} \cdot \mathbf{x}_{bc}}{r_{bc}^3} - \frac{1 + \omega}{2 + \omega} v_a^2 + 2 \left(\frac{3 + 2\omega}{2 + \omega} \right) \mathbf{v}_a \cdot \mathbf{v}_b + \\ &- \frac{3 + 2\omega}{2 + \omega} v_b^2 + \frac{3}{2} (\mathbf{v}_b \cdot \hat{\mathbf{n}}_{ab})^2 \left. \right\} - \frac{1}{2} \left(\frac{10 + 7\omega}{2 + \omega} \right) \sum_{b \neq a} \frac{m_b}{r_{ab}} \sum_{c \neq ab} \frac{m_c x_{bc}^j}{r_{bc}^3} + \\ &+ \sum_{b \neq a} \frac{m_b}{r_{ab}^3} \mathbf{x}_{ab} \cdot \left[2 \left(\frac{3 + 2\omega}{2 + \omega} \right) \mathbf{v}_a - \frac{4 + 3\omega}{2 + \omega} \mathbf{v}_b \right] (v_a^j - v_b^j), \quad (1.279) \end{aligned}$$

where

$$(m_P)_a^{jk} = m_a \delta^{jk} \left[1 + \left(1 + 4\Lambda - \frac{1 + \omega}{2 + \omega} \right) \frac{\Omega_a}{m_a} \right], \quad (1.280)$$

$$[m_A(\hat{\mathbf{n}}_{ab})]_b = m_b \left[1 + \left(1 + 4\Lambda - \frac{1 + \omega}{2 + \omega} \right) \frac{\Omega_b}{m_b} \right]. \quad (1.281)$$

Brans-Dicke theory

$$a_{a,self}^j = 0, \quad (1.282)$$

$$a_{a,Newt}^j = \frac{(m_P)_a^{jk}}{m_a} \mathfrak{U}_{,k}, \quad (1.283)$$

$$\begin{aligned} a_{a,nbody}^j = & \sum_{b \neq a} \frac{m_b x_{ab}^j}{r_{ab}^3} \left\{ \frac{6 + 4\omega_{BD}}{2 + \omega_{BD}} \frac{m_b}{r_{ab}} + \frac{8 + 5\omega_{BD}}{2 + \omega_{BD}} \frac{m_a}{r_{ab}} + \sum_{c \neq ab} \frac{m_c}{r_{bc}} + \right. \\ & + \frac{6 + 4\omega_{BD}}{2 + \omega_{BD}} \sum_{c \neq ab} \frac{m_c}{r_{ac}} - \frac{1}{2} \sum_{c \neq ab} m_c \frac{\mathbf{x}_{ab} \cdot \mathbf{x}_{bc}}{r_{bc}^3} - \frac{1 + \omega_{BD}}{2 + \omega_{BD}} v_a^2 + \\ & \left. + \frac{6 + 4\omega_{BD}}{2 + \omega_{BD}} \mathbf{v}_a \cdot \mathbf{v}_b - \frac{3 + 2\omega_{BD}}{2 + \omega_{BD}} v_b^2 + \frac{3}{2} (\mathbf{v}_b \cdot \hat{\mathbf{n}}_{ab})^2 \right\} + \\ & - \frac{1}{2} \left(\frac{10 + 7\omega_{BD}}{2 + \omega_{BD}} \right) \sum_{b \neq a} \frac{m_b}{r_{ab}} \sum_{c \neq ab} \frac{m_c x_{bc}^j}{r_{bc}^3} + \\ & + \sum_{b \neq a} \frac{m_b}{r_{ab}^3} \mathbf{x}_{ab} \cdot \left[\frac{6 + 4\omega_{BD}}{2 + \omega_{BD}} \mathbf{v}_a + \right. \\ & \left. - \frac{4 + 3\omega_{BD}}{2 + \omega_{BD}} \mathbf{v}_b \right] (v_a^j - v_b^j), \quad (1.284) \end{aligned}$$

with

$$(m_P)_a^{jk} = m_a \delta^{jk} \left(1 + \frac{1}{2 + \omega_{BD}} \frac{\Omega_a}{m_a} \right), \quad (1.285)$$

$$[m_A(\hat{\mathbf{n}}_{ab})]_b = m_b \left(1 + \frac{1}{2 + \omega_{BD}} \frac{\Omega_b}{m_b} \right). \quad (1.286)$$

$f(R)$ theory

$$a_{a,self}^j = 0, \quad (1.287)$$

$$a_{a,Newt}^j = \frac{(m_P)_a^{jk}}{m_a} \mathfrak{U}_{,k}, \quad (1.288)$$

$$\begin{aligned} a_{a,nbody}^j &= \sum_{b \neq a} \frac{m_b x_{ab}^j}{r_{ab}^3} \left\{ \left(\frac{m_b}{r_{ab}} + \frac{m_a}{r_{ab}} + \sum_{c \neq ab} \frac{m_c}{r_{ac}} \right) \times \right. \\ &\quad \times \left(\frac{120 f''(R)^6 + 16 f'(R)^3 + 187 f'(R) f''(R)^4 + 2 (f^{(3)}(R) + 48) f'(R)^2 f''(R)^2}{2 (2 f''(R)^2 + f'(R))^2 (3 f''(R)^2 + 2 f'(R))} \right) + \\ &\quad + \frac{m_a}{r_{ab}} + \left[\frac{f'(R) f''(R)^2 (2 f^{(3)}(R) f'(R) - f''(R)^2)}{2 (2 f''(R)^2 + f'(R))^2 (3 f''(R)^2 + 2 f'(R))} + 1 \right] \sum_{c \neq ab} \frac{m_c}{r_{bc}} + \\ &\quad - \frac{1}{2} \sum_{c \neq ab} m_c \frac{\mathbf{x}_{ab} \cdot \mathbf{x}_{bc}}{r_{bc}^3} - \left(\frac{f''(R)^2}{2 f''(R)^2 + f'(R)} + 1 \right) v_a^2 + \\ &\quad + \left. \left(\frac{f''(R)^2}{2 f''(R)^2 + f'(R)} + 2 \right) (2 \mathbf{v}_a \cdot \mathbf{v}_b - v_b^2) + \frac{3}{2} (\mathbf{v}_b \cdot \hat{\mathbf{n}}_{ab})^2 \right\} + \\ &\quad - \frac{1}{2} \left(9 - \frac{2 f'(R)}{2 f''(R)^2 + f'(R)} \right) \sum_{b \neq a} \frac{m_b}{r_{ab}} \sum_{c \neq ab} \frac{m_c x_{bc}^j}{r_{bc}^3} + (v_a^j - v_b^j) \times \\ &\quad \times \sum_{b \neq a} \frac{m_b}{r_{ab}^3} \mathbf{x}_{ab} \cdot \left[2 \left(\frac{f''(R)^2}{2 f''(R)^2 + f'(R)} + 2 \right) \mathbf{v}_a + \right. \\ &\quad \left. - \left(4 - \frac{f'(R)}{2 f''(R)^2 + f'(R)} \right) \mathbf{v}_b \right], \quad (1.289) \end{aligned}$$

with

$$(m_P)_a^{jk} = m_a \delta^{jk} \left[1 - \frac{2 f''(R)^2 (3 f''(R)^4 - (f^{(3)}(R) - 1) f'(R)^2 + 4 f'(R) f''(R)^2)}{(2 f''(R)^2 + f'(R))^2 (3 f''(R)^2 + 2 f'(R))} \frac{\Omega_a}{m_a} \right], \quad (1.290)$$

$$[m_A(\hat{\mathbf{n}}_{ab})]_b = m_b \left[1 - \frac{2 f''(R)^2 (3 f''(R)^4 - (f^{(3)}(R) - 1) f'(R)^2 + 4 f'(R) f''(R)^2)}{(2 f''(R)^2 + f'(R))^2 (3 f''(R)^2 + 2 f'(R))} \frac{\Omega_b}{m_b} \right]. \quad (1.291)$$

1.4.1 Final remarks

Fixing the free parameters through the equations of motion provides an alternative technique to test gravity theories in the weak field, without exploiting the numerical values of the PPN parameters. Planetary Ephemeris Program (PEP) is a software that allows us to evaluate the orbital motion of planets, see Sec. 4.4. Our plan is to use PEP to enter the alternative theories equations of motion calculated above. However, this requires a revision of the FORTRAN code used to write the software, which is currently set on GR.

1.5 The frame dragging

When Einstein began formulating his theory of GR, he attempted to incorporate Mach's principle, which states that rotations and accelerations relative to fixed and distant masses in the universe ("distant stars") cause the appearance of inertial forces. For instance, a clock that co-rotates at a constant distance around a spinning body will result forward in the starting point relative to a second clock at rest there; contrariwise, a counter-rotating clock will be behind the other one in that same point [61]. Thus, a particle orbiting a rotating body undergoes precession.

Numerous experiments conducted in the Solar System aim to quantify this effect, even though it is minimal in the weak field. Today, the goal of new space missions is to improve the accuracy of previous missions' measurements as well as to test the precession also in alternative theories of gravity. As is usual, the theoretical framework is essential. In the case of the Solar System, we employ PPN formalism to analyze the phenomenon.

Let $x^\mu(\tau)$ be the world line of a gyroscope orbiting a rotating body and let u^μ be its tangent (time-like) four-vector. We denote by S^μ the spin of the gyroscope, which is a space-like four-vector defined at each point of the gyroscope's world line. From these definitions, we immediately find that $S^\mu u_\mu = 0$ [62]. Along the curve, S^μ obeys to Fermi - Walker (FW) transport law [42]

$$u^\nu S^\mu_{;\nu} = u^\mu (a^\nu S_\nu), \quad (1.292)$$

where $a^\mu = u^\nu u^\mu_{;\nu}$ is the gyroscope's four-acceleration.

Let us observe that, if the world line is a geodesic, the acceleration is null and the FW transport becomes the parallel transport.

To evaluate the variation in spin orientation, we introduce an orthonormal

local frame at each point along the gyroscope's trajectory

$$g_{\alpha\beta}e_{\hat{\mu}}^{\alpha}e_{\hat{\nu}}^{\beta} = \eta_{\mu\nu}. \quad (1.293)$$

Here, $\hat{\mu}, \hat{\nu} = (0, 1, 2, 3)$ label the tetrad vectors; this indices are raised or lowered through the Minkowski's metric $\eta_{\mu\nu}$. By construction

$$e_{\hat{0}}^{\mu} = u^{\mu}. \quad (1.294)$$

The spatial part of this vector base is non-rotating, therefore it is obtained with a Lorentz boost plus a renormalization of the lengths, and does not satisfy the FW law [33, 42, 62]

$$e_{\hat{j}}^0 = v_j + O(\epsilon^3), \quad (1.295)$$

$$e_{\hat{j}}^k = (1 - \gamma U)\delta_{kj} + \frac{1}{2}v_j v_k + O(\epsilon^4). \quad (1.296)$$

Now, we will determine the components of the spin four-vector in this new frame. It is straightforward to demonstrate that spin is a purely spatial vector also in this new base; in fact,

$$S_{\hat{0}} \equiv e_{\hat{0}}^{\mu} S_{\mu} = u^{\mu} S_{\mu} = 0. \quad (1.297)$$

Instead, for the $S_{\hat{j}}$ components, we use Eq. (1.292) and the fact that $e_{\hat{j}}^{\mu} u_{\mu} = 0$, obtaining

$$0 = e_{\hat{j}}^{\mu} u^{\nu} S_{\mu;\nu} = u^{\nu} S_{\hat{j};\nu} - S_{\mu} u^{\nu} e_{\hat{j};\nu}^{\mu}. \quad (1.298)$$

The first term is nothing but¹³

$$u^{\nu} S_{;\nu} = \frac{dS_j}{d\tau}. \quad (1.299)$$

To evaluate the second term in Eq. (1.298), we use Eqs.(1.295) - (1.296). Specifically, from Eq.(1.295), we have

$$S^0 = v_j S_{\hat{j}} + O(\epsilon^3) S_j; \quad (1.300)$$

while from Eq.(1.296)

$$S^k = (1 - \gamma U) S_{\hat{k}} + \frac{1}{2} v_k v_j S_{\hat{j}} + O(\epsilon^4) S_j. \quad (1.301)$$

¹³ $u^0 = dx^0/d\tau$.

Therefore, considering also the PPN expansion of the metric tensor (see Eqs. (1.116) - (1.118)), Eq. (1.298) becomes

$$\frac{dS_{\hat{j}}}{d\tau} = S_{\hat{k}} [v_{[j}a_{k]} + g_{0[k,j]} - (2\gamma + 1)v_{[j}U_{,k]}], \quad (1.302)$$

Equivalently, in vector form

$$\frac{d\mathbf{S}}{d\tau} = \boldsymbol{\Omega} \times \mathbf{S}, \quad (1.303)$$

where

$$\boldsymbol{\Omega} = -\frac{1}{2}\mathbf{v} \times \mathbf{a} - \frac{1}{2}\nabla \times \mathbf{g} + \left(\gamma + \frac{1}{2}\right)\mathbf{v} \times \nabla U, \quad (1.304)$$

and

$$\mathbf{g} \equiv g_{oj}\mathbf{e}_j. \quad (1.305)$$

As shown in Eq. (1.304), $\boldsymbol{\Omega}$ is the sum of three terms. The first

$$\boldsymbol{\Omega}_{\text{Th}} = -\frac{1}{2}\mathbf{v} \times \mathbf{a} \quad (1.306)$$

is the *Thomas precession*, which is particularly important in the fine structure of the atomic spectrum. The last term

$$\boldsymbol{\Omega}_{\text{dS}} = \left(\gamma + \frac{1}{2}\right)\mathbf{v} \times \nabla U \quad (1.307)$$

is the *de Sitter precession*, which is caused by the gyroscope's rotational velocity relative to the static component of the gravitational field generated by the central body. It was determined for the first time by de Sitter in 1916, in the context of GR, who obtained $\frac{3}{2}\mathbf{v} \times \nabla U$, which is perfectly consistent with Eq. (1.307) when $\gamma = 1$.

Finally, the second term in Eq. (1.304) is the *Lense-Thirring precession*

$$\boldsymbol{\Omega}_{\text{LT}} = -\frac{1}{2}\nabla \times \mathbf{g} = \frac{1}{2}\left(\frac{\alpha_1}{4} + \gamma + 1\right)\frac{3(\mathbf{J} \cdot \hat{\mathbf{r}})\hat{\mathbf{r}} - \mathbf{J}}{r^3}. \quad (1.308)$$

In GR, it becomes

$$\boldsymbol{\Omega}_{\text{LT}}^{\text{GR}} = -\frac{1}{2}\nabla \times \mathbf{g} = \frac{3(\mathbf{J} \cdot \hat{\mathbf{r}})\hat{\mathbf{r}} - \mathbf{J}}{r^3}. \quad (1.309)$$

Since in the previous sections we determined the PPN parameters for several alternative metric theories of gravity, we can write the analytical expression of the Lense-Thirring precession in each of these models.

Horndeski's theory

$$\Omega_{\text{LT}}^{\text{H}} = \left(\frac{3 + 2\omega_{\text{H}}}{4 + 2\omega_{\text{H}}} \right) \frac{3(\mathbf{J} \cdot \hat{\mathbf{r}})\hat{\mathbf{r}} - \mathbf{J}}{r^3}. \quad (1.310)$$

Scalar tensor theory

$$\Omega_{\text{LT}}^{\text{ST}} = \left(\frac{3 + 2\omega}{4 + 2\omega} \right) \frac{3(\mathbf{J} \cdot \hat{\mathbf{r}})\hat{\mathbf{r}} - \mathbf{J}}{r^3}. \quad (1.311)$$

Brans-Dicke theory

$$\Omega_{\text{LT}}^{\text{BD}} = \left(\frac{3 + 2\omega_{\text{BD}}}{4 + 2\omega_{\text{BD}}} \right) \frac{3(\mathbf{J} \cdot \hat{\mathbf{r}})\hat{\mathbf{r}} - \mathbf{J}}{r^3}. \quad (1.312)$$

$f(R)$ theory

$$\Omega_{\text{LT}}^{f(R)} = \left[\frac{2f'(R) + 5f''(R)^2}{2f'(R) + 4f''(R)^2} \right] \frac{3(\mathbf{J} \cdot \hat{\mathbf{r}})\hat{\mathbf{r}} - \mathbf{J}}{r^3}. \quad (1.313)$$

Chapter 2

Astrophysical constraints of low and high gravity tests

The adimensional quantity that allows us to easily distinguish the weak field regime from the strong field one is¹ ϵ

$$\epsilon \sim \frac{GM}{Rc^2}, \quad (2.1)$$

where we reintroduced Newton's gravitational constant G and the speed of light c , while M and R are the mass and radius of the source of the gravitational field, respectively. We know that $\epsilon^2 \sim 10^{-5}$ in the Solar System, that is, in the weak field. This enables us to perform series expansions in the variables U , v^2 , p/ρ , and Π ; in other words, we may use the PPN formalism to describe gravity. The same is not true in strong fields, where ϵ takes on greater values; for example, $\epsilon \sim 1$ in the region of a non-rotating black hole, and $\epsilon \sim 0.2$ for a neutron star. Therefore, it is clear that we cannot employ post-Newtonian expansion to test a theory even in the strong field regime.

In this chapter, we present an alternative method for testing theories at both low and high gravity domains: the red and blue shift measure. It is based on local position invariance and precision test, along which red and blue shift measures between two identical clocks, regardless the clock structures, plays a crucial role in bounding how time intervals change in presence of gravity [63]. In practice, we evaluate the frequency modifications observed in the exchange

¹Alternatively, we can evaluate the quantity $GM/R^3c^2 \sim \ell^{-2}$, where ℓ is a scale length. When ℓ coincides with the Planck length, the regime will be characterized by quantum gravity effects. The strong field is that of Planck's time.

of a photon between two observers. This technique does not involve the field equations but only the spacetime symmetries. In this section, we compute the red and blue shift in the three distinct contexts of low, intermediate and high gravity, by considering astrophysical and cosmological sources. Specifically, we handle the binary system Earth-Mars as low energy landscape whereas white dwarfs and neutron stars as higher energy sources. To this end, we take into account a spherical Schwarzschild-de Sitter spacetime and an axially symmetric Zipoy-Voorhees metric to model all the aforementioned systems. By varying the free parameters that enter the two metrics, we got feasible red and blue shift intervals and interpreted our expectations in view of current experiments and limits.

2.1 The photon red and blue shift

First of all, let us analyze the general method used to determine the frequency shift which occurs when a photon is emitted by a massive particle (e.g. a planet or a star) and received by a distant observer. Here we follow the mathematical procedure described in [64, 65].

We start with the simplest metric describing a rotating axially symmetric spacetime (in spherical coordinates)

$$ds^2 = g_{tt}dt^2 + 2g_{t\varphi}dtd\varphi + g_{\varphi\varphi}d\varphi^2 + g_{rr}dr^2 + g_{\theta\theta}d\theta^2, \quad (2.2)$$

where $g_{\mu\nu} = g_{\mu\nu}(r, \theta)$, in the gauge $g_{r\theta} = 0$. Let us now indicate with r_e and r_d the photon's emitter and photon's detector positions, respectively², and so $u_p^\mu = (u_p^t, u_p^r, u_p^\theta, u_p^\varphi)$ is the four-velocity of the photon's emitter (when $p = e$) or of the photon's detector (when $p = d$). We should remark that d and e do not have *a priori* the meaning of distance from the central mass which generates the gravitational field. Rather, these positions are calculated with respect to a suitable reference system, whose origin could coincide with the object's center of mass. Since the above relation refers to a massive object, the following normalization condition holds

$$u_p^\mu u_{p,\mu} = -1, \quad (2.3)$$

²From now on, to simplify the notation, we will denote these two positions with r_p , where the subscript p can be e or d depending on whether it refers to the emitter or the detector respectively.

which explicitly reads

$$[g_{tt}(u^t)^2 + g_{rr}(u^r)^2 + g_{\varphi\varphi}(u^\varphi)^2 + g_{\theta\theta}(u^\theta)^2 + g_{t\varphi}u^t u^\varphi] \Big|_{r=r_p} = -1. \quad (2.4)$$

Similarly, we indicate with $k^\mu = (k^t, k^r, k^\theta, k^\varphi)$ the four-velocity of the photon, albeit normalization condition is now

$$k^\mu k_\mu = 0, \quad (2.5)$$

to explicitly give

$$\begin{aligned} g_{tt}(k^t)^2 + g_{rr}(k^r)^2 + g_{\varphi\varphi}(k^\varphi)^2 + \\ + g_{\theta\theta}(k^\theta)^2 + g_{t\varphi}k^t k^\varphi = 0. \end{aligned} \quad (2.6)$$

Metric components are independent from the variables t and φ , therefore there are two commuting Killing vector fields, respectively time-like and rotational ones as follow

$$\xi^\mu = (1, 0, 0, 0), \quad (2.7)$$

$$\psi^\mu = (0, 0, 0, 1). \quad (2.8)$$

These two Killing fields imply the existence of two conserved quantities for the massive particle

$$E \doteq -g_{\mu\nu}\xi^\mu u^\nu = -g_{tt}u^t - g_{t\varphi}u^\varphi, \quad (2.9)$$

$$L \doteq g_{\mu\nu}\psi^\mu u^\nu = g_{\varphi\varphi}u^\varphi + g_{t\varphi}u^t, \quad (2.10)$$

that are the total energy, E , and angular momentum, L . We now evaluate u^φ and u^t in function of the energy, E , and angular momentum, L , from Eqs. (2.9) and (2.10), to give

$$u^\varphi = -\frac{Eg_{t\varphi} + Lg_{tt}}{g_{t\varphi}^2 - g_{\varphi\varphi}g_{tt}}, \quad (2.11)$$

$$u^t = \frac{Eg_{\varphi\varphi} + Lg_{t\varphi}}{g_{t\varphi}^2 - g_{\varphi\varphi}g_{tt}}, \quad (2.12)$$

and plugging the above expressions into Eq. (2.3), we get

$$\left[g_{rr}(u^r)^2 + g_{\theta\theta}(u^\theta)^2 + 1 - \frac{E^2 g_{\varphi\varphi} + L^2 g_{tt} + 2ELg_{t\varphi}}{g_{t\varphi}^2 - g_{\varphi\varphi}g_{tt}} \right] \Big|_{r=r_p} = 0. \quad (2.13)$$

Even though the four-vector components for velocity and momentum do not vanish, rotating the polar coordinate system, the metric, Eq. (2.2), does not change. Hence, this intrinsic symmetry implies that we can limit to the equatorial plane, where $\theta = \pi/2$, leading to $u^\theta = k^\theta = 0$.

Further, since we hereafter on circular orbits only, we even require $u^r = 0$, providing Eq. (2.13) becomes

$$\left[1 - \frac{E^2 g_{\varphi\varphi} + L^2 g_{tt} + 2ELg_{t\varphi}}{g_{t\varphi}^2 - g_{\varphi\varphi}g_{tt}} \right] \Big|_{r=r_p} = 0, \quad (2.14)$$

that reduces to

$$V_{\text{eff}}(r_p) = 0. \quad (2.15)$$

The former is the energy conservation law, clearly valid for circular orbits. In addition, these orbits require [65, 66]

$$V'_{\text{eff}}(r_p) = 0, \quad (2.16)$$

$$V''_{\text{eff}}(r_p) \geq 0, \quad (2.17)$$

guaranteeing orbit stability [67] and the existence of the potential minimum³. Analogously, the two Killing fields, Eqs. (2.7) and (2.8), imply the existence of two conserved quantities for the photon, the total energy E_γ and the angular momentum L_γ

$$E_\gamma \doteq -g_{\mu\nu}\xi^\mu k^\nu = -g_{tt}k^t - g_{t\varphi}k^\varphi, \quad (2.18)$$

$$L_\gamma \doteq g_{\mu\nu}\psi^\mu k^\nu = g_{\varphi\varphi}k^\varphi + g_{t\varphi}k^t. \quad (2.19)$$

Now we have all the ingredients to determine the red and blue shift of the emitted photon. Thus, the photon frequency at given point p is defined as [36]

$$\omega_p = -(k_\mu u^\mu) |_p. \quad (2.20)$$

Since we consider time-like orbits that are both circular and equatorial, depending on whether we use Eqs. (2.9)-(2.10) or Eqs. (2.18)-(2.19), we can rewrite ω_p in two ways, respectively

$$\omega_p = (Ek^t - Lk^\varphi) |_p, \quad (2.21)$$

$$\omega_p = (E_\gamma u^t - L_\gamma u^\varphi) |_p. \quad (2.22)$$

³For the sake of completeness, the equality only holds for spherical symmetry.

In particular, the frequency of the photon at the emission point is

$$\begin{aligned}\omega_e &= -(k_\mu u^\mu)|_e = \\ &= (Ek^t - Lk^\varphi)|_e = \\ &= (E_\gamma u^t - L_\gamma u^\varphi)|_e,\end{aligned}\tag{2.23}$$

whereas the frequency of the photon at the detection point is

$$\begin{aligned}\omega_d &= -(k_\mu u^\mu)|_d = \\ &= (Ek^t - Lk^\varphi)|_d = \\ &= (E_\gamma u^t - L_\gamma u^\varphi)|_d.\end{aligned}\tag{2.24}$$

Thus, we define the frequency shift associated with the emission and detection of photons as

$$\begin{aligned}1 + z = \frac{\omega_e}{\omega_d} &= \frac{(E_\gamma u^t - L_\gamma u^\varphi)|_e}{(E_\gamma u^t - L_\gamma u^\varphi)|_d} = \\ &= \frac{(u^t - bu^\varphi)|_e}{(u^t - bu^\varphi)|_d},\end{aligned}\tag{2.25}$$

where⁴

$$b \equiv \frac{L_\gamma}{E_\gamma}.\tag{2.26}$$

It will also be convenient to introduce the redshift z_c corresponding to a photon emitted by a particle located at the center observed by a faraway detector, i.e. $b = 0$

$$z_c = \frac{u_e^t}{u_d^t} - 1,\tag{2.27}$$

since astronomical data are generally collected in terms of the kinematic redshift, defined as

$$\begin{aligned}z_{\text{kin}} \doteq z - z_c &= \frac{(u_e^t u_d^\varphi - u_d^t u_e^\varphi)b}{u_d^t (u_t - bu^\varphi)_d} = \\ &= \frac{(u_e^t \Omega_d - u_e^\varphi)b}{u_d^t (1 - \Omega_d b)},\end{aligned}\tag{2.28}$$

⁴Let us observe here that b is the same both at the numerator and the denominator of (2.25), since E_γ and L_γ are determined by the same photon path.

where the *angular velocity* of a detector located far away from the photons source

$$\Omega_d \equiv \frac{u_d^\varphi}{u_d^t} \quad (2.29)$$

has been introduced as well. Of course, b varies with the photon path. Then a value of b as a function of the circular orbit of the emitting source (i.e., as a function of r) must be determined, in such a way that its absolute value represents the observed radial distance on either side of the observed center ($b = 0$) by a faraway observer. The idea is that frequency shifts yielding maximum and minimum values correspond to photons emitted with initial velocities collinear to the source velocity [68]. This amounts to require $k^r = k^\theta = 0$ at $p = e$, and therefore these photons paths, recalling (2.18), (2.19), are such that

$$-E_\gamma k_e^t + L_\gamma k_e^\varphi = (k_\mu k^\mu)_e = 0, \quad (2.30)$$

that gives, using (2.26), two possible solutions for the so called *apparent impact parameter* b

$$b_\pm = -\frac{g_{t\varphi} \pm \sqrt{g_{t\varphi}^2 - g_{\varphi\varphi}g_{tt}}}{g_{tt}}, \quad (2.31)$$

depending on whether the photon is emitted by a receding, b_- , or an approaching, b_+ , object with respect to a distant observer. Hence, the b_- and b_+ solutions are related to the red and the blue shift once we substitute them in Eq. (2.25), respectively

$$\text{Red shift } z_{\text{red}} = \frac{u_e^t - b_- u_e^\varphi}{u_d^t (1 - b_- \Omega_d)} - 1, \quad (2.32)$$

$$\text{Blue shift } z_{\text{blue}} = \frac{u_e^t - b_+ u_e^\varphi}{u_d^t (1 - b_+ \Omega_d)} - 1. \quad (2.33)$$

Finally, given b_+ and b_- , from Eq. (2.28), we get two possible z_{kin} values, namely z_1 and z_2

$$z_1 = \frac{(u_e^t \Omega_d - u_e^\varphi) b_-}{u_d^t (1 - \Omega_d b_-)}, \quad (2.34)$$

$$z_2 = \frac{(u_e^t \Omega_d - u_e^\varphi) b_+}{u_d^t (1 - \Omega_d b_+)}, \quad (2.35)$$

that correspond to the cases in which the photon is emitted by a receding or an approaching source, respectively⁵.

2.1.1 Non rotating spacetime

As special case, we limit to non rotating spacetimes, i.e. the ones for which $g_{t\varphi} = 0$. This will be the case of Schwarzschild-de Sitter and Zipoy-Voorhees metrics that we analyze in the next sections. Thus, Eq. (2.2) simply reduces to

$$ds^2 = g_{tt}dt^2 + g_{\varphi\varphi}d\varphi^2 + g_{rr}dr^2 + g_{\theta\theta}d\theta^2, \quad (2.38)$$

with gauge condition, $g_{r\theta} = 0$. Clearly, all the previous equations before determined are accordingly simplified and so the conserved quantities associated to the massive particles (observes) now become

$$E = -g_{tt}u^t, \quad (2.39)$$

$$L = g_{\varphi\varphi}u^\varphi, \quad (2.40)$$

and so the velocities are $u^t = -\frac{E}{g_{tt}}$, $u^\varphi = \frac{L}{g_{\varphi\varphi}}$, while the equation $V_{\text{eff}}(r_p) = 0$ for the effective potential becomes

$$\left[1 + \frac{E^2 g_{\varphi\varphi} + L^2 g_{tt}}{g_{\varphi\varphi} g_{tt}} \right] \Big|_{r=r_p} = 0. \quad (2.41)$$

Similarly, the conserved quantities associated to the photon are

$$E_\gamma = -g_{tt}k^t, \quad (2.42)$$

$$L_\gamma = g_{\varphi\varphi}k^\varphi, \quad (2.43)$$

from which $k^t = -\frac{E_\gamma}{g_{tt}}$, $k^\varphi = \frac{L_\gamma}{g_{\varphi\varphi}}$, so that the apparent impact parameter finally reads

$$b_\pm = \mp \sqrt{-\frac{g_{\varphi\varphi}}{g_{tt}}}. \quad (2.44)$$

⁵It is remarkable to underline the relation between z_{red} , or z_{blue} , and z_{kin} . In particular, from Eq. (2.28), it reads

$$z_{red} = (z_{kin} + z_c)|_{b=b_-}, \quad (2.36)$$

$$z_{blue} = (z_{kin} + z_c)|_{b=b_+}. \quad (2.37)$$

The functional forms of z_1 and z_2 are identical to Eqs. (2.34) and (2.35) since assuming $g_{t\varphi} = 0$ modifies only the apparent impact parameters rather than z_{kin} . We here observe that $b_+ = -b_-$, implying $z_1 = -z_2$. With the above recipe in our hand we are now in condition to handle spacetime symmetries to model astrophysical landscapes. We therefore report below the two metrics involved in our computation.

2.2 Spacetime solutions

As stated above, our purpose is to test gravity theories on different energy domains, evaluating the red and blue shift of astrophysical and cosmological objects. Thereby, we first handle the simplest axisymmetric spacetime based on the Zipoy-Voorhees metric to model astrophysical objects, such as neutron stars and white dwarfs. Afterwards, we switch to the spherical symmetry based on the Schwarzschild-de Sitter metric. In such a case, differently of the astrophysical case, we intend to work out cosmological scenarios and to compute red and blue shifts by fixing the cosmological constant from Planck's measurements [18].

Clearly, these two regimes, based on two different spacetime symmetries, are profoundly different from each other. The first is a regime of high gravity, since it deals with neutron stars and white dwarfs. The second is purely cosmological, involving infrared scales of energy. Below we first summarize each metric formalism and then we argue bounds over the free coefficients.

2.2.1 The Zipoy-Voorhees metric

The strategy of getting red and blue shift is here applied to the *Zipoy-Voorhees metric* [69]. The metric, in spherical coordinates, reads

$$ds^2 = -Fdt^2 + \frac{1}{F} [Gdr^2 + Hd\theta^2 + (r^2 - 2kr) \sin^2 \theta d\varphi^2], \quad (2.45)$$

where

$$F = \left(1 - \frac{2k}{r}\right)^\delta, \quad (2.46)$$

$$G = \left(\frac{r^2 - 2kr}{r^2 - 2kr + k^2 \sin^2 \theta}\right)^{\delta^2 - 1}, \quad (2.47)$$

$$H = \frac{(r^2 - 2kr)^{\delta^2}}{(r^2 - 2kr + k^2 \sin^2 \theta)^{\delta^2 - 1}}. \quad (2.48)$$

Here, δ is a free parameter which can vary into three possible ranges

- $\delta > 1$: tidal forces diverge at the singularity, particles are crushed;
- $\frac{1}{2} < \delta < 1$: the singularity is mild, i.e. particles reach it with zero velocity;
- $\delta < \frac{1}{2}$: the singularity is repulsive, particles are ejected.

It is remarkable to notice the limiting case $\delta \rightarrow 1$ provides the Schwarzschild metric, whereas $\delta \rightarrow 1/2$ could show likely critical effects. For example, in Ref. [70] the authors worked out naked singularity configuration to get regions of repulsive gravity, using eigenvalue method [71, 72] and showing this interval as critical. However, we here focus on regular objects, such as NS, WD and/or Solar System configurations, and so we do not expect any critical region over δ and/or red or blue shifts, as we effectively get later. Furthermore, $k = m/\delta$ is the ratio between the mass m of the gravitational field and the δ parameter. As underlined before, we are limiting to the equatorial plane, *i.e.*, $\theta = \pi/2$. The Zipoy-Voorhees metric describes a non rotating spacetime ($g_{t\varphi} = 0$), thus we can consider Eq. (2.41) that reads

$$1 - \frac{E^2 (r^2 - 2kr) \left(1 - \frac{2k}{r}\right)^{-\delta} - L^2 \left(1 - \frac{2k}{r}\right)^\delta}{r^2 - 2kr} \Bigg|_{r=r_p} = 0 \quad (2.49)$$

Its derivative with respect to r gives the condition for circular orbits, say Eq. (2.16)

$$\frac{\left(1 - \frac{2k}{r}\right)^{-\delta} \left[2\delta kr E^2 (r - 2k) + 2L^2 (\delta k + k - r) \left(1 - \frac{2k}{r}\right)^{2\delta} \right]}{r^2 (r - 2k)^2} \Bigg|_{r=r_p} = 0, \quad (2.50)$$

with $r_p = r_e, r_d$, as before. Solving the system given by the two last relations, we obtain the total energy and the angular momentum

$$E = \sqrt{\frac{\left(1 - \frac{2k}{r}\right)^\delta (\delta k + k - r)}{2\delta k + k - r}} \Bigg|_{r=r_p}, \quad (2.51)$$

$$L = \pm \sqrt{\frac{\delta k r (2k - r) \left(1 - \frac{2k}{r}\right)^{-\delta}}{2\delta k + k - r}} \Bigg|_{r=r_p}. \quad (2.52)$$

Consequently, we immediately get

$$u^t|_{r=r_p} = -\sqrt{\frac{\left(1 - \frac{2k}{r}\right)^{-\delta} (\delta k + k - r)}{2\delta k + k - r}} \Bigg|_{r=r_p}, \quad (2.53)$$

$$u^\varphi|_{r=r_p} = \pm \sqrt{\frac{\delta k (2k - r) \left(1 - \frac{2k}{r}\right)^\delta}{r(k - r)^2 (2\delta k + k - r)}} \Bigg|_{r=r_p}. \quad (2.54)$$

Furthermore, from Eq. (2.44), we have

$$b_\pm = \mp \frac{\sqrt{r^2 - 2kr}}{\left(1 - \frac{2k}{r}\right)^\delta}, \quad (2.55)$$

Finally, substituting Eqs. (2.53) - (2.54) evaluated in $r = r_d$ into Eq. (2.29), we get the angular velocity

$$\Omega_{d\pm} = \mp \sqrt{\frac{\delta k (2k - r_d) \left(1 - \frac{2k}{r_d}\right)^{2\delta}}{r_d (k - r_d)^2 (\delta k + k - r_d)}}, \quad (2.56)$$

where Ω_{d+} and Ω_{d-} are respectively referred to a co-rotating and to a counter-rotating photons source with respect to the angular velocity of the gravitational field source. In conclusion, substituting all these equations into Eqs. (2.34) - (2.35), we get the expressions for z_1 and z_2 for the Zipoy-Voorhees

metric

$$\begin{aligned}
z_{1\pm} = & \pm \left\{ \left[\frac{r_e(r_d - 2k)}{r_d(r_e - 2k)} \right]^\delta \left[\left(1 - \frac{2k}{r_d} \right)^\delta \sqrt{\frac{\left(1 - \frac{2k}{r_e} \right)^\delta (2k - r_e)^2 k \delta}{(k - r_e)^2 (r_e - k - 2k\delta)}} + \right. \\
& \left. - \sqrt{\frac{\left(1 - \frac{2k}{r_e} \right)^\delta \left(1 - \frac{2k}{r_d} \right)^{2\delta} (r_d - 2k)^2 (k - r_e + k\delta) k \delta}{(r_d - k)^2 (k - r_e + 2k\delta) (r_d - k - k\delta)}} \right] \right\} \times \\
& \times \left\{ \sqrt{\frac{\left(1 - \frac{2k}{r_d} \right)^\delta (k - r_d + k\delta)}{k - r_d + 2k\delta}} \left[\left(1 - \frac{2k}{r_d} \right)^\delta + \right. \right. \\
& \left. \left. \pm \sqrt{\frac{(r_d - 2k)^2 \left(1 - \frac{2k}{r_d} \right)^{2\delta} k \delta}{(r_d - k)^2 (r_d - k - k\delta)}} \right] \right\}^{-1}, \tag{2.57}
\end{aligned}$$

$$\begin{aligned}
z_{2\pm} = & \pm \left\{ \left[\frac{r_e(r_d - 2k)}{r_d(r_e - 2k)} \right]^\delta \left[- \left(1 - \frac{2k}{r_d} \right)^\delta \sqrt{\frac{\left(1 - \frac{2k}{r_e} \right)^\delta (2k - r_e)^2 k \delta}{(k - r_e)^2 (r_e - k - 2k\delta)}} + \right. \\
& \left. + \sqrt{\frac{\left(1 - \frac{2k}{r_e} \right)^\delta \left(1 - \frac{2k}{r_d} \right)^{2\delta} (r_d - 2k)^2 (k - r_e + k\delta) k \delta}{(r_d - k)^2 (k - r_e + 2k\delta) (r_d - k - k\delta)}} \right] \right\} \times \\
& \times \left\{ \sqrt{\frac{\left(1 - \frac{2k}{r_d} \right)^\delta (k - r_d + k\delta)}{k - r_d + 2k\delta}} \left[\left(1 - \frac{2k}{r_d} \right)^\delta + \right. \right. \\
& \left. \left. \mp \sqrt{\frac{(r_d - 2k)^2 \left(1 - \frac{2k}{r_d} \right)^{2\delta} k \delta}{(r_d - k)^2 (r_d - k - k\delta)}} \right] \right\}^{-1}, \tag{2.58}
\end{aligned}$$

where the subscript \pm is again referred to a co-rotating and counter-rotating source with respect to the angular velocity of the gravitational field source. Let us observe that $z_1 = -z_2$, in both the co-rotating and counter-rotating cases, regardless of the mass that generates the gravitational field. Above we put forward that the z_1 and z_2 variations can be expressed in terms of r_d for both a rotating and counter-rotating configurations. This would help to argue the intervals of validity for the Zipoy-Voorhees free parameters when this metric is applied to astrophysical situations.

2.2.2 Gravitational field sources for the Zipoy-Voorhees metric

We analyze the variation of z_1 and z_2 as function of the position of the detector r_d , in the co-rotating and in the counter-rotating configurations. The analysis is based on different gravitational field sources

- a neutron star in the maximally - rotating configuration [73], corresponding to a high gravity regime,
- a white dwarf in the maximally - rotating configuration [73], corresponding to an intermediate gravity regime,
- Earth and Mars for the Solar System, corresponding to a low gravity regime.

We report the plots 2.1, 2.3 and 2.5 in which we infer the availability intervals for each term.

For the neutron star, the variation of z_1 and z_2 as function of r_d depend stronger on δ . For this reason, we choose three values of δ , one for each range, Fig. 2.1

1. $\delta = 1000$, *i.e.*, where we take an arbitrary large value to address the condition $\delta \gg 1$,
2. $\delta = \frac{3}{4}$, as arbitrary close value to $\delta = 1$, obtained as mean value of the interval $\frac{1}{2} < \delta < 1$,
3. $\delta = \frac{1}{4}$, as arbitrary close value to $\delta = 0$, obtained as mean value of the interval $0 < \delta < \frac{1}{2}$.

However, for WDs, see Fig. 2.3, the increase or decrease of δ do not seem to modify the overall evolution. The same happens for the binary configuration constituted by the Earth and Mars: one can notice from Fig. 2.5 that they very weakly depend upon δ variation. The above configuration is built up assuming the Earth and Mars as distinct gravitational sources as separate cases. For the sake of clearness, the δ variation is not so evident from the plots since those variations are extremely small and not particularly visible. The corresponding values have been evaluated for WDs, Earth and Mars, noticing a slight difference that permits one to fix δ to portray the examples we showed in the aforementioned figures. Even though not so evident from

the plots, the above occurrence for which δ is as larger as one approaches higher gravity regimes turns out to be clear even from a theoretical viewpoint. As one approaches regimes of low gravity any quadrupole deviation is negligibly small and so one can approximate with a spherical symmetry those configurations, without losing generality. Furthermore, in the low and intermediate gravity regimes the symmetries $z_{1+} = z_{2-}$ and $z_{1-} = z_{2+}$ emerge, together with $z_{1\pm} = -z_{2\pm}$, being valid for any gravitational sources. The pending caveat to check would be represented by orbit stability, i.e. Eq. (2.17). For the Zipoy-Voorhees metric, the second derivative with respect to r of Eq. (2.49) is always zero: since this is a quasi-spherical spacetime, we can assert that all orbits are stable.

Finally, let us observe that, for $\delta = 1$ and, consequently, $k = m$, all these equations reduce to those obtained in the Schwarzschild metric. It is now remarkable to stress that for $\delta = 1/2$, in all the analyzed gravity regimes, we do not obtain critical values of z , as expected.

2.2.3 The Schwarzschild-de Sitter metric

In this subsection, we apply the method described above to the Schwarzschild-de Sitter metric, corresponding to a spherical symmetric spacetime with an effective cosmological constant, Λ [75, 76, 77]. For this fundamental property, the metric can be used for cosmological applications, to infer bounds on red and blue shifts, fixing Λ . In spherical coordinates, we have

$$ds^2 = - \left(1 - \frac{2m}{r} + \frac{\Lambda r^2}{3} \right) dt^2 + \frac{1}{\left(1 - \frac{2m}{r} + \frac{\Lambda r^2}{3} \right)} dr^2 + r^2 d\theta^2 + r^2 \sin^2 \theta d\varphi^2. \quad (2.59)$$

We again stress, we study the phenomenon in the equatorial plane, namely $\theta = \pi/2$. Even this metric is clearly non-rotating and so Eq. (2.41) becomes

$$\left[1 - \frac{E^2 r^2 - L^2 \left(1 - \frac{2m}{r} + \frac{\Lambda r^2}{3} \right)}{r^2 \left(1 - \frac{2m}{r} + \frac{\Lambda r^2}{3} \right)} \right] \Big|_{r=r_p} = 0, \quad (2.60)$$

and its derivative with respect to r

$$\left[\frac{6(3m + \Lambda r^3)E^2}{(\Lambda r^3 + 3r - 6m)} - \frac{2L^2}{r^3} \right] \Big|_{r=r_p} = 0. \quad (2.61)$$

with $r_p = \{r_e, r_d\}$, as before. Solving the system given by the former two equations, we obtain

$$E^2 = \frac{(\Lambda r^3 + 3r - 6m)^2}{9r(r - 3m)} \Big|_{r=r_p}, \quad (2.62)$$

$$L^2 = \frac{r^2(3m + \Lambda r^3)}{3(r - 3m)} \Big|_{r=r_p}, \quad (2.63)$$

from which we get the total energy and the angular momentum

$$E = \frac{\Lambda r^3 + 3r - 6m}{\sqrt{9r(r - 3m)}} \Big|_{r=r_p}, \quad (2.64)$$

$$L = \pm r \sqrt{\frac{3m + \Lambda r^3}{3(r - 3m)}} \Big|_{r=r_p}. \quad (2.65)$$

Thus, we again find

$$u^t|_{r=r_p} = \sqrt{\frac{r}{r - 3m}} \Big|_{r=r_p}, \quad (2.66)$$

$$u^\varphi|_{r=r_p} = \pm \sqrt{\frac{3m + \Lambda r^3}{3r^2(r - 3m)}} \Big|_{r=r_p}. \quad (2.67)$$

Furthermore, we have

$$b_\pm = \mp \sqrt{\frac{r^2}{\left(1 - \frac{2m}{r} + \frac{\Lambda r^2}{3}\right)}}, \quad (2.68)$$

$$\Omega_{d\pm} = \pm \sqrt{\frac{3m + \Lambda r_d^3}{3r_d^3}}, \quad (2.69)$$

where Ω_{d+} and Ω_{d-} are respectively referred to a co-rotating and to a counter-rotating photons source with respect to the angular velocity of the gravitational field source, as before. Hence, plugging all these relations within Eqs. (2.34)-(2.35), we get the expressions for z_1 and z_2 for the Schwarzschild-de

Sitter metric

$$z_{1\pm} = \pm \frac{\sqrt{\frac{r_e}{r_e-3m}} \left(\sqrt{\frac{3m+\Lambda r_d^3}{3r_d-6m+\Lambda r_d^3}} - \sqrt{\frac{3m+\Lambda r_e^3}{3r_e-6m+\Lambda r_e^3}} \right)}{\sqrt{\frac{r_d}{r_d-3m}} \left(1 \mp \sqrt{\frac{3m+\Lambda r_d^3}{3r_d-6m+\Lambda r_d^3}} \right)}, \quad (2.70)$$

$$z_{2\pm} = \mp \frac{\sqrt{\frac{r_e}{r_e-3m}} \left(\sqrt{\frac{3m+\Lambda r_d^3}{3r_d-6m+\Lambda r_d^3}} - \sqrt{\frac{3m+\Lambda r_e^3}{3r_e-6m+\Lambda r_e^3}} \right)}{\sqrt{\frac{r_d}{r_d-3m}} \left(1 \pm \sqrt{\frac{3m+\Lambda r_d^3}{3r_d-6m+\Lambda r_d^3}} \right)}, \quad (2.71)$$

where the subscript \pm is again referred to a co-rotating and counter-rotating source with respect to the angular velocity of the gravitational field source. Let us observe that $z_1 = -z_2$, in both the co-rotating and counter-rotating cases, regardless of the mass that generates the gravitational field.

2.2.4 Gravitational field sources for the Schwarzschild-de Sitter metric

In analogy to the previous treatment, for the Schwarzschild-de Sitter metric we analyze the variation of z_1 and z_2 as function of the position of the detector r_d , in the co-rotating and in the counter-rotating cases. As before, the analysis is based on different gravitational field sources

- a neutron star in the maximally - rotating configuration [73], see Fig. 2.2. Here the employed field is strong,
- a white dwarf in the maximally - rotating configuration [73], see Fig. 2.4. Here we consider an intermediate field,
- Earth and Mars for the Solar System, see Fig. 2.6.

Furthermore, we consider Λ as the cosmological constant, whose value is $\Lambda = 1.1056 \times 10^{-52} m^{-2}$ [18]. As for the Zipoy-Voorhees metric, in the low and intermediate gravity regimes we again find $z_{1+} = z_{2-}$ and $z_{1-} = z_{2+}$, in addition to $z_{1\pm} = -z_{2\pm}$. The last thing to check is the orbits stability, i.e. Eq. (2.17). For the Schwarzschild-de Sitter metric, the second derivative of Eq. (2.60) is

$$\left[\frac{8\Lambda r^4 + 6mr(1 - 5\Lambda r^2) - 36m^2}{r^2(r - 3m)(\Lambda r^3 + 3r - 6m)} \right] \Big|_{r=r_p} \geq 0. \quad (2.72)$$

Thus, we study Eq. (2.72) for every gravitational field source.

By considering the photons emitter placed on the neutron star, i.e. $r_e = R$, with R the neutron star radius, we get that the emitter orbit is stable

$$V''_{\text{eff}}(r_e) = 7.61641 \times 10^{-4} > 0, \quad (2.73)$$

while the detector orbit is stable for

$$r_d \geq 9.4374 \text{ km}. \quad (2.74)$$

Analogously, by considering the photons emitter placed on the white dwarf, i.e. $r_e = R$, with R the white dwarf radius, we get that the emitter orbit is stable

$$V''_{\text{eff}}(r_e) = 8.62859 \times 10^{-14} > 0, \quad (2.75)$$

while the detector orbit is stable for

$$r_d \geq 1.5876 \text{ km}. \quad (2.76)$$

Finally, by considering the photons emitter placed on the planet, i.e. $r_e = r_{\text{Earth}}$ and $r_e = r_{\text{Mars}}$, with r_{Earth} and r_{Mars} the Earth and Mars radius respectively, we get that the emitters orbits are stable

$$V''_{\text{eff}}(r_e) = 3.42303 \times 10^{-17} > 0 \text{ for Earth}, \quad (2.77)$$

$$V''_{\text{eff}}(r_e) = 2.43224 \times 10^{-17} > 0 \text{ for Mars}, \quad (2.78)$$

while the detectors orbits are stable for

$$r_d \geq 2.65555 \times 10^{-5} \text{ km for Earth}, \quad (2.79)$$

$$r_d \geq 2.84142 \times 10^{-6} \text{ km for Mars}. \quad (2.80)$$

As before, let us observe that, for $\Lambda \rightarrow 0$, all these equations reduce to those obtained in the Schwarzschild metric.

2.3 Results

In this section, we compare these theoretical predictions with current experimental bounds, got from experiments. Finally, we propose how to build up plausible experiments and develop technical configurations to check the validity of these methods.

2.3.1 High and intermediate gravity regimes

The increase or decrease of the red and blue shift bounds depend upon the choice of the free parameters. The possible underlying configuration is crucial in understanding how to single out the most feasible interval of redshifts or blue shifts. We then split the involved two symmetries below, commenting separately on findings and comparing the obtained bounds with previous expectations got from the literature.

Numerical values got during computation		
	M	R
	(M_\odot)	($10^3 m$)
WD	0.18	18304.5
NS	1.07	13.61

Table 2.1: *Table of astrophysical values adopted during the computation for high and intermediate gravity regimes. We only consider the maximally rotating configurations for NS and WD, where gravitational effects are stringent.*

NS case

In the case of NS, we compute expectations over $z_1(r)$ and $z_2(r)$ in the maximally - rotating configuration, with the ranges of masses and radii respectively given by $M \in [1.07; 1.47]M_\odot$ and $r \simeq 13.61$. The values got by z_1 and z_2 reach a plateau as $d \gtrsim 0$, i.e., as d becomes larger than zero. This indicates the strong gravity regime of NS, as expected, and happens for both the setups of Schwarzschild-de Sitter and Zipoy-Voorhees spacetimes, when the former is computed for very large δ values.

Particularly, the Zipoy-Voorhees metric seems to match the Schwarzschild-de Sitter solution as the quadrupole increases, in agreement with the fact that NS are described as rotating objects. Further, this indicates the Schwarzschild - de Sitter spacetime is a suitable approximation for determining the NS red and blue shifts, although the metric itself does not describe a rotating object. The very impressive fact is that one underlines very small changes within the interval $\delta \in [0.75; 10^3]$. This suggests a limiting regime between the above interval, being compatible with the theoretical bounds over δ that exclude repulsive effects of gravity.

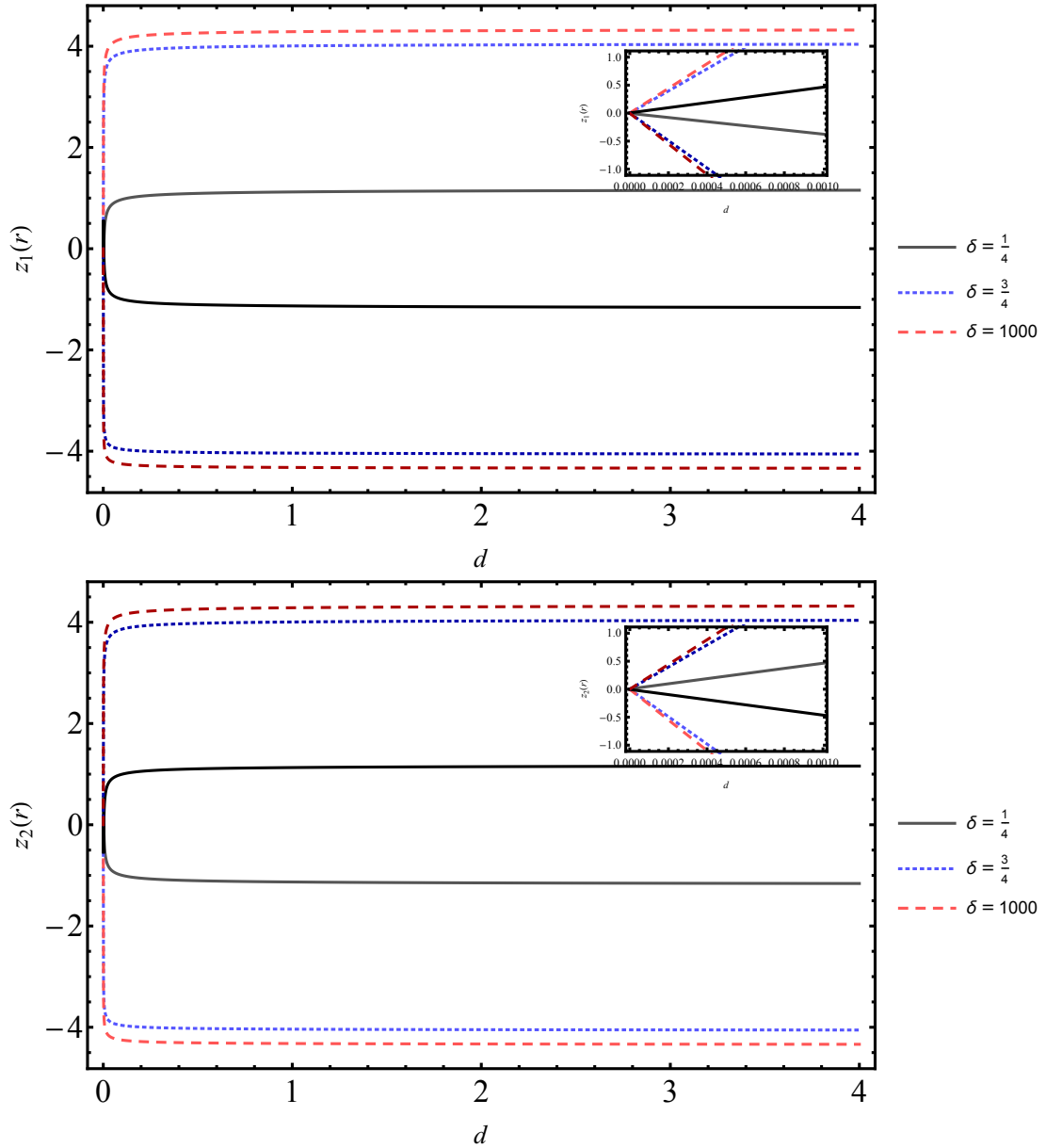


Figure 2.1: $z_1(r)$ and $z_2(r)$ as function of $d = r_d - r_e$ within the Zipoy-Voorhees spacetime. The gravitational field source is a neutron star of mass $M = 1.07M_\odot$, with $M_\odot = 1.47$ km the solar mass, and radius $R = 13.61$ km, in the maximally - rotating configuration [73]. Here, $d \in [0; 4 \cdot 10^5]$ km, whereas z_1 and z_2 are in power of 10^{-1} . In the small zoom, we report z_1 and z_2 up to $d = 40$ km.

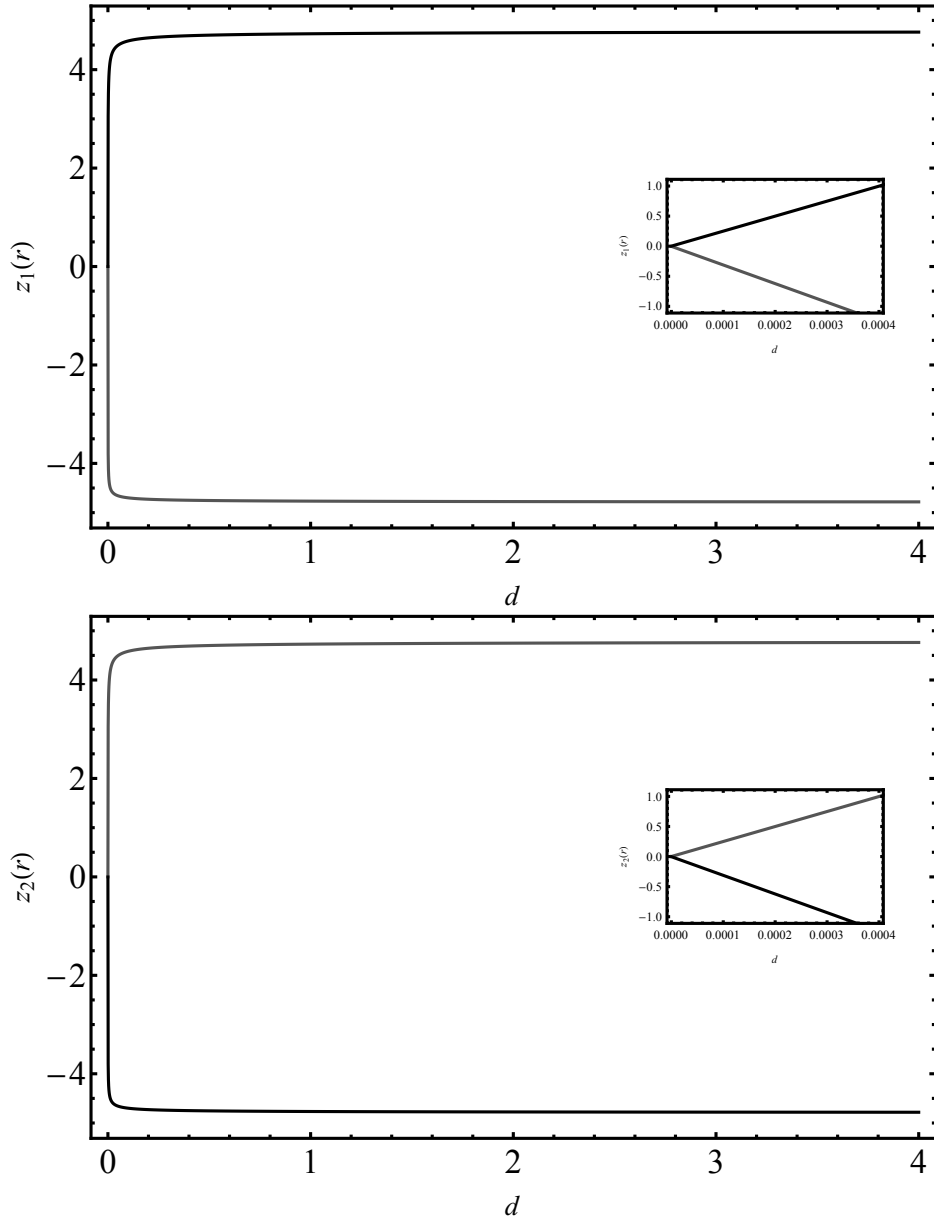


Figure 2.2: $z_1(r)$ and $z_2(r)$ as function of $d = r_d - r_e$ within the Schwarzschild-Sitter spacetime. The gravitational field source is a neutron star of mass $M = 1.07M_\odot$, with $M_\odot = 1.47$ km the solar mass, and radius $R = 13.61$ km, in the maximally - rotating configuration [73]. Here, $d \in [0; 4 \cdot 10^5]$ km, whereas z_1 and z_2 are in power of 10^{-1} . In the small zoom, we report z_1 and z_2 up to $d = 40$ km.

WD case

In the case of WD, we have regimes of intermediate gravity. We therefore compute our expectations over $z_1(r)$ and $z_2(r)$ in the maximally - rotating configuration, with the ranges of masses and radii respectively given by $M \in [0.18; 1.47]M_\odot$ and $r \simeq 18304.5$ km. The values got by z_1 and z_2 reach a plateau as $d \gtrsim 3$, *i.e.*, as d becomes larger than zero. As well as NS regime for both the setups of Schwarzschild-de Sitter and Zipoy-Voorhees spacetimes, with very large δ , we encounter the same behaviors. As for the NS, we can deduce that the Schwarzschild - de Sitter metric is even a good approximation for WDs in determining the red and the blue shift. Finally, from Figs. (2.3) - (2.4) we immediately get

$$z_{1+,ZV} = z_{2-,ZV} = z_{1-,SdS} = z_{2+,SdS} , \quad (2.81)$$

$$z_{1-,ZV} = z_{2+,ZV} = z_{1+,SdS} = z_{2-,SdS} , \quad (2.82)$$

where the subscripts ZV and SdS indicate Zipoy-Voorhees and Schwarzschild-de Sitter spacetimes respectively.

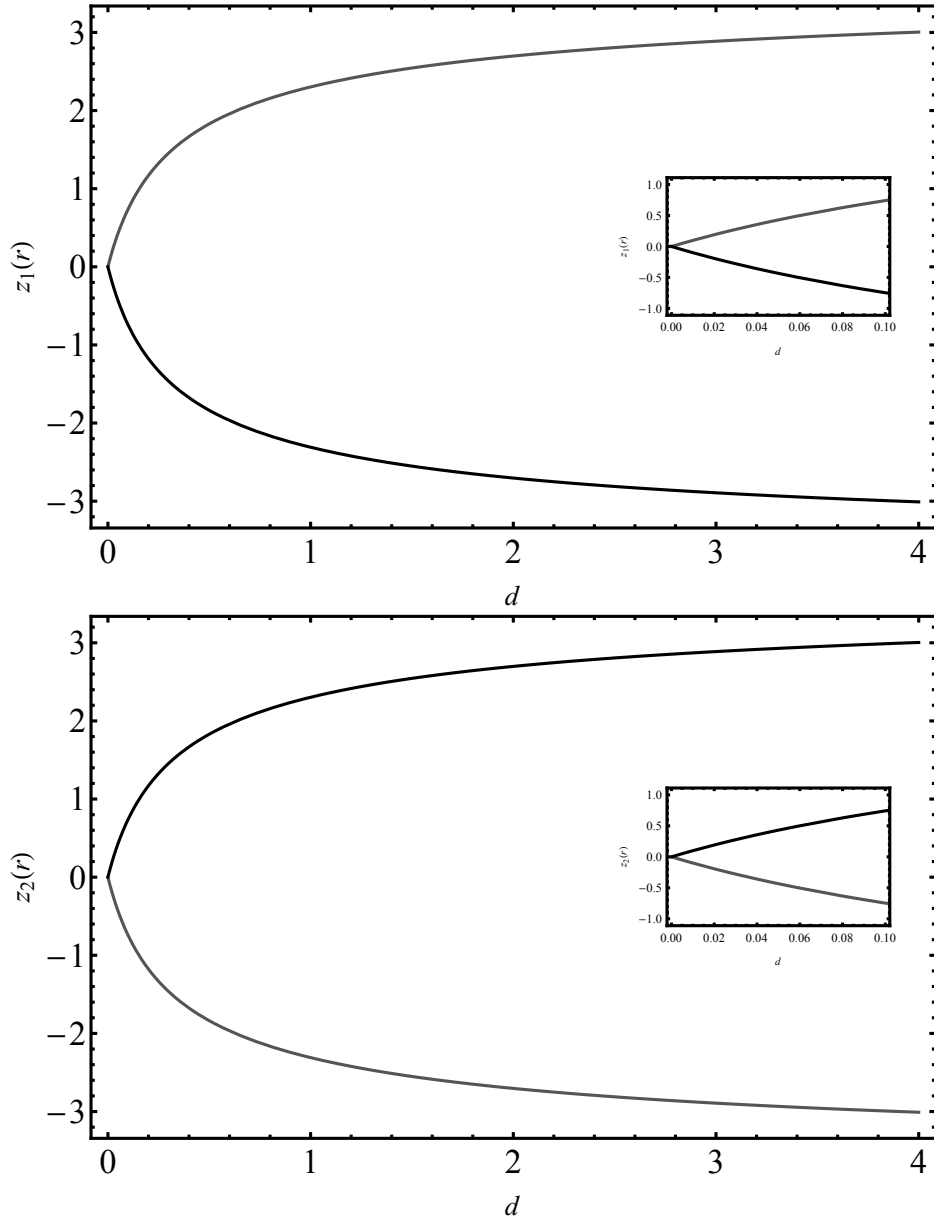


Figure 2.3: $z_1(r)$ and $z_2(r)$ as function of $d = r_d - r_e$ within the Zipoy-Voorhees spacetime. The gravitational field source is a white dwarf of mass $M = 0.18M_\odot$, with $M_\odot = 1.47$ km the solar mass, and radius $R = 18304.5$ km, in the maximally - rotating configuration [73]. Here, $d \in [0; 4 \cdot 10^5]$ km, whereas z_1 and z_2 are in power of 10^{-3} . In the small zoom, we report z_1 and z_2 up to $d = 10^4$ km.

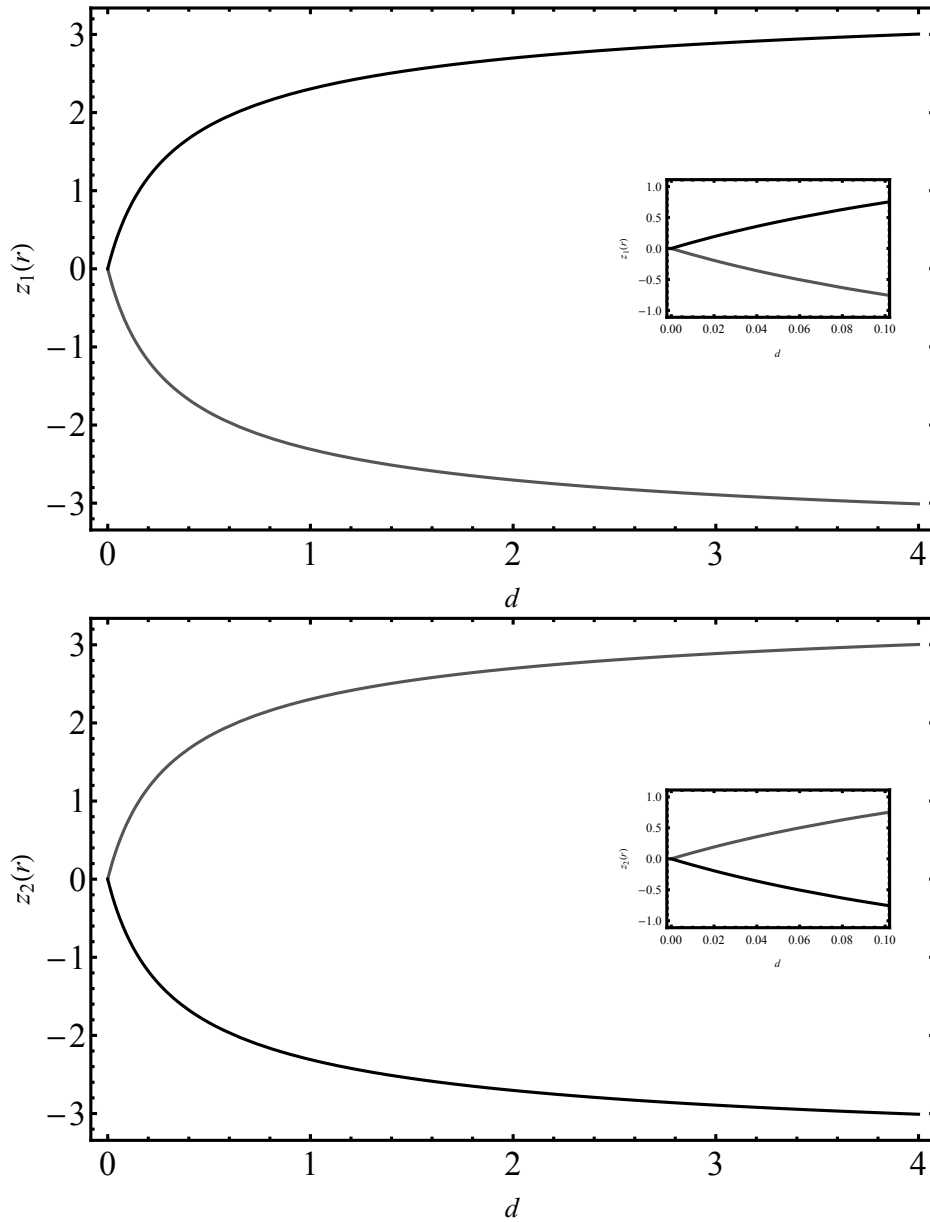


Figure 2.4: $z_1(r)$ and $z_2(r)$ as function of $d = r_d - r_e$ within the Schwarzschild-de Sitter spacetime. The gravitational field source is a white dwarf of mass $M = 0.18M_\odot$, with $M_\odot = 1.47$ km the solar mass, and radius $R = 18304.5$ km, in the maximally - rotating configuration [73]. Here, $d \in [0; 4 \cdot 10^5]$ km, whereas z_1 and z_2 are in power of 10^{-3} . In the small zoom, we report z_1 and z_2 up to $d = 10^4$ km.

2.3.2 Regime of low gravity

The use of lunar LR is commonly got using powerful pulsed searchlight, from the Earth to lunar Cube Corner Retroreflectors⁶ (CCRs) [78, 79]. More generally, LR is a technique that gets a measure of the round - trip time of a laser fired by a ground station on Earth, received by a CCR on a satellite and reflected back to the station. If the satellite is not the Moon, we refer to as satellite LR [80]. We follow here both the lunar and satellite LR approaches to face the low gravity regime.

For every LR experiment is performed, it is important to take into account the relative motion between the laser source and the retroreflector. This causes an angular deflection of the laser beam. In fact, in absence of a relative motion, the laser would exactly return back to the station. The angular deflection is also called velocity aberration (VA) and it is defined as

$$VA = \frac{2}{c} [\Delta v_d - v_e \cos \phi], \quad (2.83)$$

where Δv_d is the difference between the orbital velocity and rotational velocity at the equator of the satellite or planet on which is placed the retroreflector, v_e the rotational velocity of the satellite or planet on which is placed the laser source at the equator and ϕ the laser source latitude. Consequently, the term in the square brackets in Eq. (2.83) represents the relative velocity between the involved two objects. We are going to use the VA and the laser wavelength to determine the red and blue shifts through relativistic Doppler effect in the equatorial plane, *i.e.*,

$$\lambda' = \lambda \sqrt{\frac{1 + VA/2}{1 - VA/2}} \quad (2.84)$$

where, instead of the ratio between the relative velocity and c , we used the VA through Eq. (2.83). Thus, one immediately computes the required z through the standard formula $z = \frac{\lambda' - \lambda}{\lambda}$.

We study the theoretical models by considering Earth and Mars as sources of the gravitational field in the Solar System, see Figs. 2.5-2.6.

We want to compare the theoretical results with the experimental ones deriving from the LR missions.

⁶Device made up of three perpendicular reflective surfaces which retro-reflect the signal in the same direction in which it arrived. For more details, see Sec. 4.2.

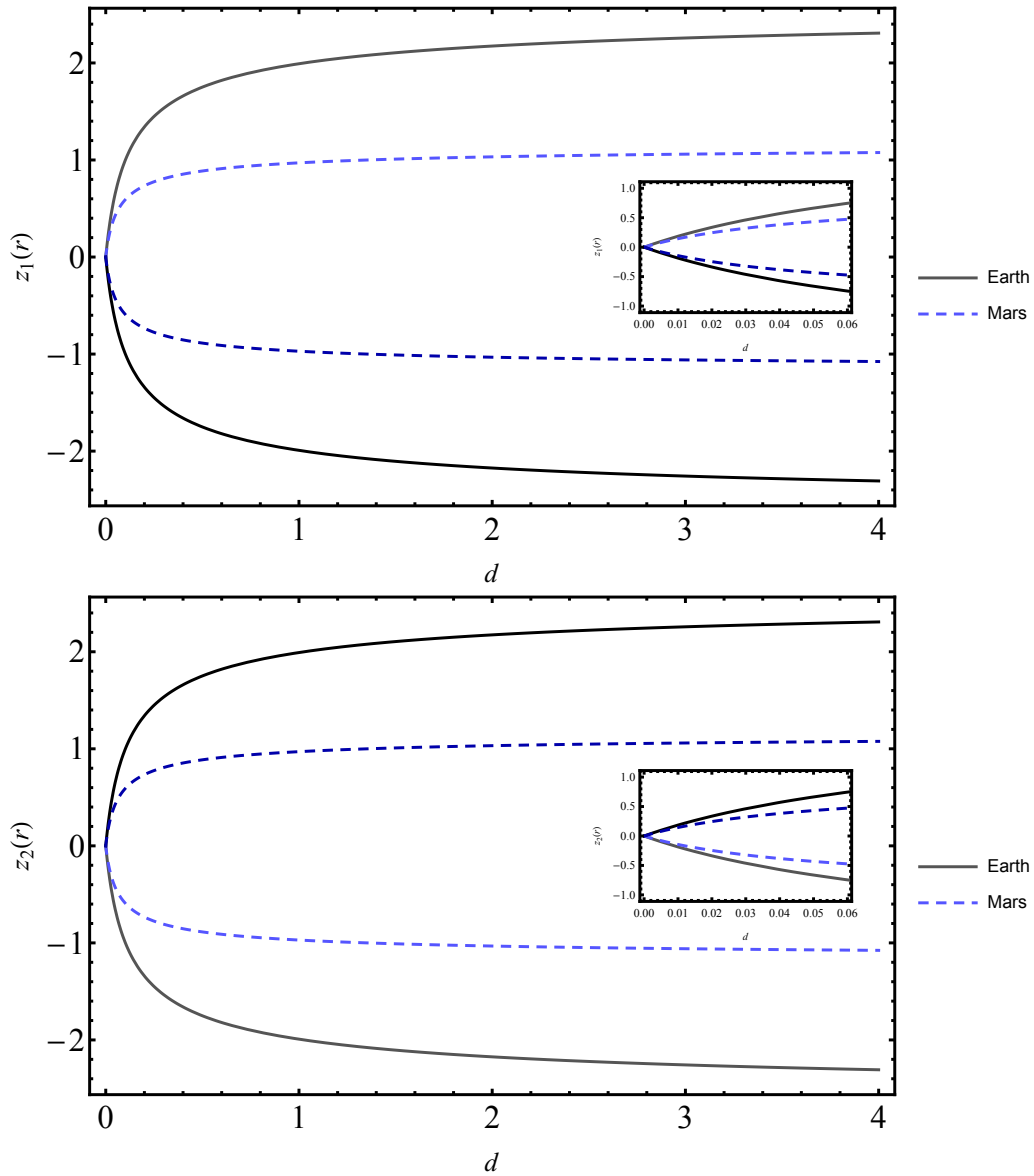


Figure 2.5: $z_1(r)$ and $z_2(r)$ as function of $d = r_d - r_e$ within the Zipoy-Voorhees spacetime. We analyzed the two cases, i.e. emitter on Mars and Earth respectively, with $d \in [0; 4 \cdot 10^5]$ km, whereas z_1 and z_2 are in power of 10^{-5} . In the small zoom, we report z_1 and z_2 up to $d = 6 \cdot 10^3$ km. This choice enables to get feasible intervals for Phobos, where $d \simeq 5986.5$ km, with Mars as source, and intervals for LARES-2 [74], where $d \simeq 5899$ km, with Earth as source.

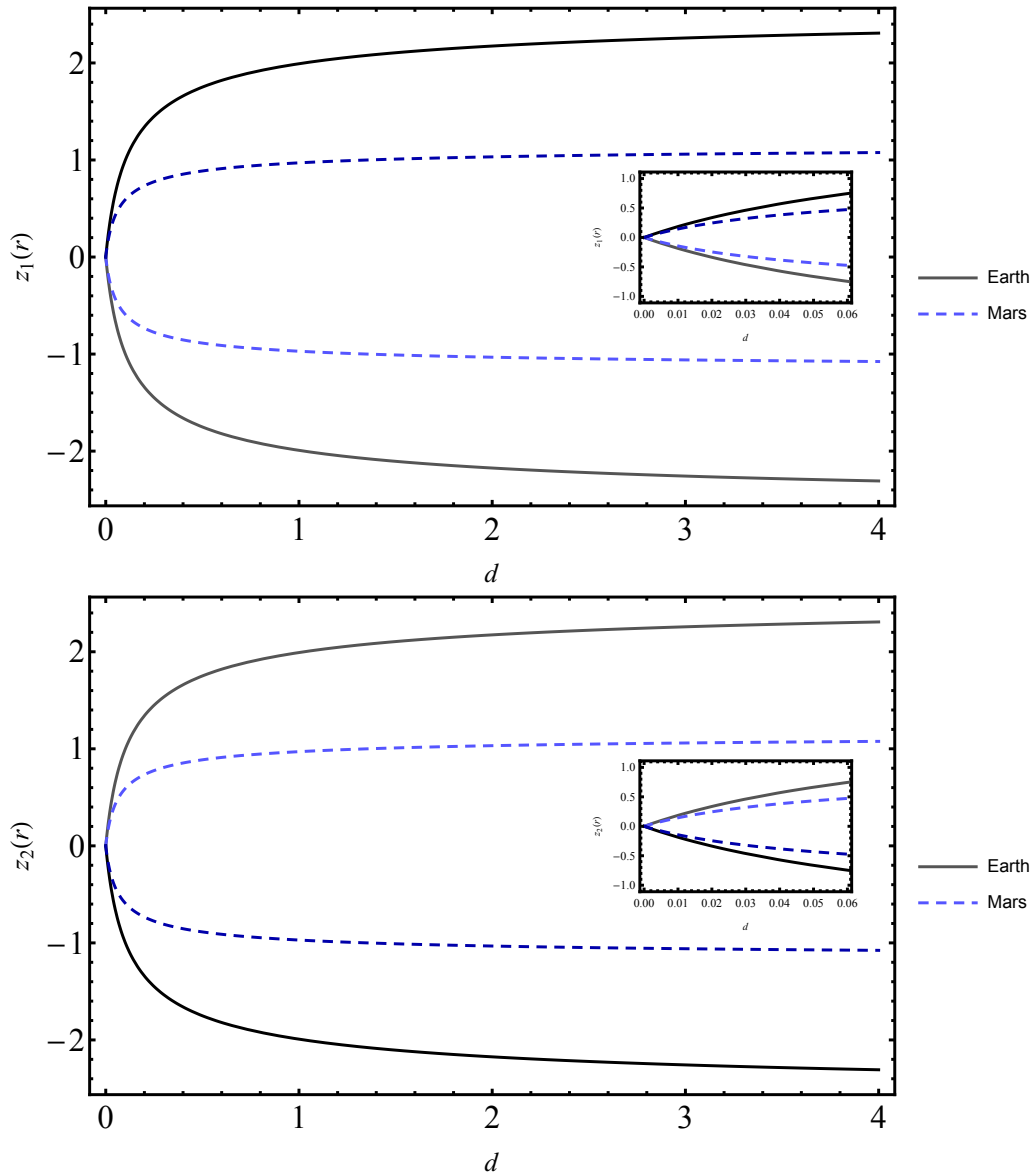


Figure 2.6: $z_1(r)$ and $z_2(r)$ as function of $d = r_d - r_e$ within the Schwarzschild-de Sitter spacetime. We analyzed the two cases, i.e. emitter on Mars and Earth respectively, with $d \in [0; 4 \cdot 10^5]$ km, whereas z_1 and z_2 are in power of 10^{-5} . In the small zoom, we report z_1 and z_2 up to $d = 6 \cdot 10^3$ km. This choice enables to get feasible intervals for Phobos, where $d \simeq 5986.5$ km, with Mars as source, and intervals for LARES-2 [74], where $d \simeq 5899$ km, with Earth as source.

We thus analyze three particular configurations

- Earth-Moon system. Here, we model the two astrophysical objects and involve the lunar LR.
- Earth-satellite system. Here, the configuration is analogous to the standard lunar LR, but using an artificial satellite instead of the Moon. This second case is therefore similar to the previous one⁷.
- Mars-Phobos system. Here we propose *ex novo* an architecture to get feasible red and blue shift ranges. It involves a laser source placed on Mars, considered as the gravitational source, modeled through the spacetime approach described before. The CCRs could be placed on Phobos, i.e. a natural Mars satellite⁸. A similar approach has been developed by [81], where the authors proposed a system constituted by Earth and Phobos. The procedure we here develop permits to extend previous results through the use of alternative technologies of LR.

The predicted values, got from the theoretical models under exam for these three configurations, are portrayed in Tabs. 2.2-2.3. Here, we again observe the same symmetries reported in Eqs. (2.81,2.82). On the other hand, the indirect measurements of z , obtained starting from the experimental data of the LR, are instead reported in Tabs. 2.4-2.6. The slight differences between experimental and predicted outcomes are due to several facts. First, experimentally speaking, we are handling the VA technique only. In fact, although different types of CCRs used in space missions, to calculate z we only require the VAs depending on the orbital and rotational involved objects velocities, the local position of the laser source on the planet and the laser beam wavelength, generally 532 nm. Second, the accuracy can be refined adopting more than the configurations here investigated. Below, we summarize how to heal such issues adopting direct measure methods, by proposing novel experimental configurations.

⁷We here refer to the LARES-2 expectations. For us, LARES-2 is the acronym of Laser RELativity Satellite No. 2 and makes use of the Earth-satellite LR prerogative that we need. For more details, see Sec. 4.3.1.

⁸This prerogative goes beyond the binary system Earth-Moon, with the advantage of being closer to each other, i.e. guaranteeing a more precise pulse measure.

$z \pm \delta z$	lunar LR (10^{-5})	Satellite LR (10^{-6})	Phobos LR (10^{-6})
$z_{1+} \equiv z_{2-}$	2.298042	7.36990	4.72646
$\delta z_{1+} \equiv \delta z_{2-}$	± 0.000005	± 0.01551	± 0.00046
$z_{1-} \equiv z_{2+}$	-2.298057	-7.37018	-4.72653
$\delta z_{1-} \equiv \delta z_{2+}$	± 0.000005	± 0.01551	± 0.00046

Table 2.2: Table of red and blue shift values, predicted by means of the Zipoy-Voorhees metric. We also report the corresponding error bars, namely $\delta z_{1,2\pm}$, evaluated by the standard logarithmic error propagation. Since for low gravity, the predictions over z do not significantly change by varying δ , with an accuracy smaller than one part over 10^6 , we arbitrarily select $\delta = 0.5$. Here we consider lunar LR for the system Earth-Moon, satellite LR for the system Earth - LARES-2 [74] and finally Phobos LR for the proposed experiment that employs Mars and its satellite, Phobos.

$z \pm \delta z$	lunar LR (10^{-5})	Satellite LR (10^{-6})	Phobos LR (10^{-6})
$z_{1+} \equiv z_{2-}$	-2.298057	-7.37018	-4.72653
$\delta z_{1+} \equiv \delta z_{2-}$	± 0.000005	± 0.01551	± 0.00046
$z_{1-} \equiv z_{2+}$	2.298057	7.37018	4.72653
$\delta z_{1-} \equiv \delta z_{2+}$	± 0.000005	± 0.01551	± 0.00046

Table 2.3: *Table of red and blue shift values, predicted by means of the Schwarzschild-de Sitter metric. We also report the corresponding error bars, namely $\delta z_{1,2\pm}$, evaluated by the standard logarithmic error propagation. Here we consider lunar LR for the system Earth-Moon, satellite LR for the system Earth - LARES-2 [74] and finally Phobos LR for the proposed experiment that employs Mars and its satellite, Phobos.*

Station	ϕ	VA (10^{-6})	$z \pm \delta z$ (10^{-6})
McDonald	30°.68 N	4.051	2.025629 ± 0.000007
Apollo	32°.78 N	4.112	2.055989 ± 0.000007
Matera	40°.65 N	4.370	2.185235 ± 0.000007
Grasse	43°.75 N	4.485	2.242475 ± 0.000007

Table 2.4: z value for four different operational LR stations placed on Earth and retroreflectors placed on the Moon. The velocities are expressed in units of radiant. We also report the corresponding errors, namely δz , evaluated by the standard logarithmic error propagation. The table is split into $\phi < 40$ and $\phi > 40$. The increase of z in function of ϕ is more than 10% for largest ϕ here reported. The mean value is: $(2.127332 \pm 0.000007) \cdot 10^{-6}$.

Station	ϕ	VA (10^{-6})	$z \pm \delta z$ (10^{-5})
McDonald	30°.68 N	35.30	1.76428 ± 0.00159
Apollo	32°.78 N	35.36	1.76826 ± 0.00159
Matera	40°.65 N	35.62	1.78118 ± 0.00159
Grasse	43°.75 N	35.74	1.78690 ± 0.00159

Table 2.5: z value for four different operational LR stations placed on Earth and retroreflectors placed on LARES-2 satellite [74]. The velocities are expressed in units of radiant. We also report the corresponding errors, namely δz , evaluated by the standard logarithmic error propagation. The table is split into $\phi < 40$ and $\phi > 40$. The increase of z in function of ϕ is more than 10% for largest ϕ here reported. The mean value is: $(1.775155 \pm 0.00159) \cdot 10^{-5}$.

Station	ϕ	VA (10^{-6})	$z \pm \delta z$ (10^{-6})
Mars	0°	12.63	6.314072 ± 0.000052

Table 2.6: In this table, we report a plausible z value for a station placed on Mars equator, with the ansatz that a few retroreflectors will be placed on Phobos, as we proposed above. We also report the corresponding errors, namely δz , evaluated by the standard logarithmic error propagation. In particular, we figure out a laser station placed on Mars equator, i.e., the position in which satellite views got from Mars leads to the best configuration.

Designs of proposed experimental setups

In view of the overall results, we summarize the following consequences.

- At high gravity regimes δ values, using axisymmetric spacetime, agree with the Schwarzschild-de Sitter prediction, making use of the Planck satellite bounds.
- As well as NS, the regimes of intermediate gravity, here investigated employing WD, behave in analogy.
- At low gravity, in the Solar System, the adopted spacetime metrics are clearly unadequate to fix stringent limits over the free parameters as well as the red and blue shift intervals that slightly disagree with observations (see Tabs. 2.4-2.6).
- Analogously LR cannot be used to get indirect measurements for z . Moreover, the results coming from the use of Schwarzschild metric, without taking care about the Λ value, seem to agree with our scheme, indicating that Λ is quite badly constrained within the Solar System.

From the above considerations, a direct measure of z would be more predictive than other indirect treatments. So that, one can build up experimental setups based on genuine wavelength measures only. To do so, let us take the simplest configuration we could work with, based on the Earth-Moon system. We can send a laser pulse whose wavelength is known, as well as in the lunar LR technique. The detector is meant to measure the corresponding wavelength and then to get possible hints on red or blue shifts. Alternatively, another possibility is offered by a rotating orbiter around Mars or more away planets, without excluding to take into account other configurations. The orbiter sends signals, whose wavelength is known. The detector, again placed on the given planet we are considering, gets the signals and provides a direct measure of the pulse shift in wavelength that is converted in red and blue shift. Last but not least, even if the astrophysical configurations of NS and WD could in principle be adopted for future missions to better get z , the experimental complexity to put on them instruments would be a great limitation for the experiment itself. On the other hand, cosmological red and blue shifts would be the key to fix the cosmological constant value. The strategy would be to take the large scale structure of the universe, switching the spacetime to more complicated metrics that could overcome the likely issues related to Schwarzschild-de Sitter.

2.3.3 Error analysis

In this subsection, we report the values of z and the respective errors obtained when the field sources are the NS and the WD, both in the two employed metrics. We have selected 3 values of $d = r_d - r_e$ within the range chosen for the plots, $d \in [0; 4 \cdot 10^5]$. In particular

- $d = 0$ and $d = 4 \cdot 10^5$, i.e. the extremes of the interval;
- $d = 2 \cdot 10^5$, which is the midpoint of the interval.

In the case of the Zipoy-Voorhees metric, we considered the δ values chosen for the plots ($\delta = 1/4$, $\delta = 3/4$ and $\delta = 1000$); while for the Schwarzschild-de Sitter metric, we considered the Λ value of the Planck collaboration: $\Lambda = (1.10566 \pm 0.022703) \cdot 10^{-46} \text{ km}^{-2}$.

Errors are calculated through the standard logarithmic error propagation, considering that for NS and WD it is hard to get with high accuracy both mass and radii. We therefore work out the following strategy: we consider Refs. [82, 83] and there we got the maximum and minimum bounds associated to mass and radii for both NS and WD. Then, we consider the average constraints and use for computation, in particular

- for NS: $M = (1.07 \pm 0.11) M_\odot$ and $R = 13.61_{-0.68}^{+2.18} \text{ km}$,
- for WD: $M = (0.180_{-0.004}^{+0.056}) M_\odot$ and $R = 18304.5_{-823.70}^{+5491.3} \text{ km}$,

where $M_\odot = 1.47 \text{ km}$.

	$d = 0$		$d = 2 \cdot 10^5$		$d = 4 \cdot 10^5$	
	NS	WD	NS	WD	NS	WD
$\delta = 1/4$						
$z_{1+} = z_{2-}$	$0.00000^{+0.11185}_{-0.03489}$	$0.00000^{+0.00057}_{-0.00009}$	$0.11412^{+0.25949}_{-0.15085}$	$0.00265^{+0.00098}_{-0.00011}$	$0.11555^{+0.25894}_{-0.15050}$	$0.00299^{+0.00103}_{-0.00012}$
$z_{1-} = z_{2+}$	$0.00000^{+0.12958}_{-0.04042}$	$0.00000^{+0.00057}_{-0.00009}$	$-0.11477^{+0.26092}_{-0.15166}$	$-0.00265^{+0.00098}_{-0.00012}$	$-0.11601^{+0.25995}_{-0.15107}$	$-0.00299^{+0.00104}_{-0.00012}$
$\delta = 3/4$						
$z_{1+} = z_{2-}$	$0.00000^{+0.01657}_{-0.00517}$	$0.00000^{+0.00057}_{-0.00009}$	$0.40249^{+0.07605}_{-0.04408}$	$0.00265^{+0.00098}_{-0.00011}$	$0.40385^{+0.07626}_{-0.04423}$	$0.00299^{+0.00103}_{-0.00012}$
$z_{1-} = z_{2+}$	$0.00000^{+0.03254}_{-0.01015}$	$0.00000^{+0.00057}_{-0.00009}$	$-0.40475^{+0.07659}_{-0.04444}$	$-0.00265^{+0.00098}_{-0.00012}$	$-0.40545^{+0.07646}_{-0.04449}$	$-0.00299^{+0.01037}_{-0.00012}$
$\delta = 1000$						
$z_{1+} = z_{2-}$	$0.00000^{+0.02404}_{-0.00750}$	$0.00000^{+0.00057}_{-0.00009}$	$0.43056^{+0.08699}_{-0.05044}$	$0.00265^{+0.00098}_{-0.00011}$	$0.43194^{+0.08719}_{-0.05058}$	$0.00299^{+0.00103}_{-0.00012}$
$z_{1-} = z_{2+}$	$0.00000^{+0.05126}_{-0.01599}$	$0.00000^{+0.00057}_{-0.00009}$	$-0.43302^{+0.08761}_{-0.05085}$	$-0.00265^{+0.00098}_{-0.00012}$	$-0.43366^{+0.08762}_{-0.05087}$	$-0.00299^{+0.00104}_{-0.00012}$

Table 2.7: z values with errors for the Zipoy-Voorhees metric, with a NS and a WD as field sources, for 3 different values of δ , at 3 different values of d .

	$d = 0$		$d = 2 \cdot 10^5$		$d = 4 \cdot 10^5$	
	NS	WD	NS	WD	NS	WD
$z_{1+} = z_{2-}$	$0.00000^{+0.06596}_{-0.02057}$	$0.00000^{+0.00057}_{-0.00009}$	$-0.47754^{+0.11548}_{-0.06703}$	$-0.00266^{+0.00098}_{-0.00012}$	$-0.47816^{+0.11549}_{-0.06705}$	$-0.00299^{+0.00104}_{-0.00012}$
$z_{1-} = z_{2+}$	$0.00000^{+0.06596}_{-0.02057}$	$0.00000^{+0.00057}_{-0.00009}$	$0.47754^{+0.11578}_{-0.06703}$	$0.00266^{+0.00098}_{-0.00012}$	$0.47816^{+0.11549}_{-0.06705}$	$0.00299^{+0.00104}_{-0.00012}$

Table 2.8: z values with errors for the Schwarzschild-de Sitter metric, with a NS and a WD as field sources, at 3 different values of d .

2.3.4 Results for the Schwarzschild spacetime

The Schwarzschild metric reads

$$ds^2 = - \left(1 - \frac{2m}{r}\right) dt^2 + \frac{1}{\left(1 - \frac{2m}{r}\right)} dr^2 + r^2 d\Omega^2, \quad (2.85)$$

with $d\Omega^2 = d\theta^2 + \sin^2\theta d\varphi^2$. Below, we summarize the main results of the general procedure, described in Sec. 2.1, applied to this metric. In particular, we find an overall agreement with the results got in [64]. We have as conserved quantities

$$E = \frac{r - 2m}{\sqrt{r(r - 3m)}} \Big|_{r=r_p}, \quad (2.86)$$

$$L = \pm r \sqrt{\frac{m}{r - 3m}} \Big|_{r=r_p}, \quad (2.87)$$

and velocities

$$u^t|_{r=r_p} = \sqrt{\frac{r}{r - 3m}} \Big|_{r=r_p}, \quad (2.88)$$

$$u^\varphi|_{r=r_p} = \pm \frac{1}{r} \sqrt{\frac{m}{r - 3m}} \Big|_{r=r_p}, \quad (2.89)$$

and the kinematic quantities

$$b_\pm = \mp \frac{r}{\sqrt{1 - \frac{2m}{r}}}, \quad (2.90)$$

$$\Omega_{d\pm} = \pm \sqrt{\frac{m}{r_d^3}}. \quad (2.91)$$

Finally, $z_{1\pm}$ and $z_{2\pm}$ are

$$z_{1\pm} = \pm \frac{\sqrt{\frac{r_e}{r_e - 3m}} \left(\frac{1}{\sqrt{r_d - 2m}} - \frac{1}{\sqrt{r_e - 2m}} \right)}{\sqrt{\frac{r_d}{r_d - 3m}} \left[1 \mp \sqrt{\frac{m}{r_d - 2m}} \right]}, \quad (2.92)$$

$$z_{2\pm} = \mp \frac{\sqrt{\frac{r_e}{r_e - 3m}} \left(\frac{1}{\sqrt{r_d - 2m}} - \frac{1}{\sqrt{r_e - 2m}} \right)}{\sqrt{\frac{r_d}{r_d - 3m}} \left(1 \pm \sqrt{\frac{m}{r_d - 2m}} \right)}. \quad (2.93)$$

Comparing these last two equations with those obtained for the Zipoy-Voorhees metric and for the Schwarzschild-de Sitter metric, we easily note that Eqs. (2.57) - (2.58) reduce to Eqs. (2.92) - (2.93) for $\delta = 1$ (that is $k = m$) and Eqs. (2.70) - (2.71) reduce to Eqs. (2.92) - (2.93) for $\Lambda = 0$.

$z \pm \delta z$	lunar LR (10^{-5})	Satellite LR (10^{-6})	Phobos LR (10^{-6})
$z_{1+} \equiv z_{2-}$	-2.298057	-7.37018	-4.72653
$\delta z_{1+} \equiv \delta z_{2-}$	± 0.000005	± 0.01551	± 0.00046
$z_{1-} \equiv z_{2+}$	2.298057	7.37018	4.72653
$\delta z_{1-} \equiv \delta z_{2+}$	± 0.000005	± 0.01551	± 0.00046

Table 2.9: *Table of red and blue shift values, predicted by means of the Schwarzschild metric. We also report the corresponding errors, namely $\delta z_{1,2\pm}$, evaluated by the standard logarithmic error propagation. Here we consider lunar LR for the system Earth-Moon, satellite LR for the system Earth - LARES-2 [74] and finally Phobos LR for the proposed experiment that employs Mars and its satellite, Phobos.*

Chapter 3

High gravity tests

One of the new frontiers of physics is undoubtedly the realization of space missions aimed at observing the universe in regions of spacetime where relativistic effects are relevant. The study of Einstein's equations solutions in the strong gravity regime is an ever-evolving subject of research. In particular, wormholes have received a lot of attention in recent years. The properties of these mathematical solutions to the field equations encourage researchers to investigate numerous theoretical models, both in the context of GR and extended/modified theories, in order to gain a better understanding of gravitational phenomena.

After examining modified theories in the PPN formalism to test them in the weak field regime, in this chapter we see how they can describe structures in strong gravitational fields. Specifically, we will employ $f(R)$ theory to find exact solutions of traversable wormholes.

3.1 Wormholes solutions of Einstein's equations

Wormholes can be interpreted as “short-cuts” connecting different spacetime regions [84] and so they represent hypothetical tunnels between two asymptotic regimes of the same spacetime [85]. In the most accredited scenario, the wormhole short cut path is traversable through a *minimal surface area called wormhole throat*. The simplest approach showing these features is the so called Einstein-Rosen bridge coming from the connection of two Schwarzschild solutions [86, 87, 88, 89]. It is characterized by spherical sym-

metry and by the presence of an event horizon. This implies that any observer, trying to cross the wormhole throat, inevitably falls into the singularity [90]. Hence, the metric itself *a priori* prevents the traversability due to the singularity. Consequently, to heal this issue, one can consider non-singular metrics defined for every radial coordinates [91]. However, if the Birkhoff theorem is valid and matter fields are included in a non-vanishing energy-momentum tensor, this approach leads to severe bounds at the wormhole throat. There, the condition $\tau_0 > \rho_0 c^2$ must hold, i.e. radial tension might be large enough to exceed the total mass-energy density [91]. Consequently the energy-momentum tensor violates the null energy condition (NEC) at the throat [84, 92], $T_{\mu\nu}k^\mu k^\nu < 0$, in naive analogy to some cosmological contexts, see e.g. [93, 94]. Thus, in this *standard approach*, i.e. in the framework of GR, one is forced to take a negative energy density and pressure. This exotic landscape provides a structure that can be *traversable*, albeit it is not clear how matter could exhibit negative energy density and pressure [95]. In other words, standard matter cannot be used to achieve stable wormhole solutions in the framework of GR.

In this respect, several approaches have been proposed to alleviate the problem. They focus mainly in considering exotic forms of matter to overcome this strange behavior. Conversely, extended and/or modified theories of gravity are natural suites where this can be addressed retaining standard matter [96, 47, 48, 49, 50]. In fact, in these scenarios, the above conditions do not apply directly to matter and so, in lieu of imposing exotic conditions over the energy and pressure, one can take geometry to play the role of exotic matter [51]. This mimics the wormhole properties through higher-order curvature terms and/or effective field theories that can be mapped into Lagrangians extending the Einstein-Hilbert one.

In this section, in analogy to GR, we consider a spherically symmetric metric with two asymptotically flat regions. In particular, we take in to account $f(R)$ gravity theories, in metric formalism, and we assume time-independent metric coefficients, using the widely-consolidate Morris-Thorne spacetime. We thus determine exact solutions of traversable wormhole, without violating the signs of energy and pressure, postulating a power-law form for $f(R)$, i.e. $f(R) = f_0 R^{1+\epsilon}$ where ϵ is a real number. Immediately, GR can be recovered in the limit $\epsilon \rightarrow 0$. In this perspective, we can control deviations from GR and the role of geometric terms in stabilizing the wormhole solutions. In this context, two classes of stable and traversable wormhole can be recovered.

In the first case, the throat is assumed as an inverse power of the radial coordinate. In the second case, we consider a parameter α controlling the size of the throat. It is worth noticing that these solutions can be recovered by assuming simple rational series, made in terms of $(0, 1)$ Padé polynomials. We thus provide a physical interpretation over these choices and investigate the physical properties associated to them. In this regard, we impose the fluid perturbations passing through the throat are negligibly small. This condition is achieved if the sound speed is vanishing during the fluid evolution. This feature cannot be found in GR, albeit it gets suitable constraints over the free coefficients of our wormhole picture. In particular, we show that if the sound speed is zero to guarantee stability, even the Starobinsky scalaron [52] (with $\sim R^2$) is not fully recovered within this scheme, leading to solutions with $\epsilon \neq 0$. It means that GR cannot be trivially recovered by construction. We thus discuss which power law intervals are allowed under this scheme and discuss the corresponding physical implications.

3.1.1 $f(R)$ wormholes with rational shape reconstructions

A static and spherically symmetric wormhole solution is

$$ds^2 = e^{2\Phi(r)} dt^2 - \frac{1}{1 - b(r)/r} dr^2 - r^2 d\Omega^2, \quad (3.1)$$

which is the so-called Morris and Thorne metric [91]. Eq. (3.1) characterizes a wormhole with the following features: (i) the spacetime is static and spherically symmetric; (ii) the throat has a minimal surface connecting two asymptotically flat regions; (iii) there is no Killing horizon and then two-way travels are enabled. The physical realization of such criteria depends on the gravitational forces, the proper time for crossing and astrophysical scales where possible wormholes are expected [97].

In this picture, $b(r)$ and $\Phi(r)$ are functions of the radial coordinate and they are denoted respectively as *shape* and *redshift functions*. The radial coordinate r ranges from a minimum and a positive value r_0 , defining the wormhole throat, to infinity. In order to avoid the presence of event horizons, one imposes that $\Phi(r)$ is finite at any r . It is possible to construct asymptotically flat spacetimes, where $b(r)/r \rightarrow 0$ and $\Phi \rightarrow 0$ as $r \rightarrow \infty$. A fundamental ingredient in wormhole physics is the the so-called *flare-out condition* of the

wormhole throat $b(r_0) = r_0$ [91] given by the condition $(b'r - b)/2b^2 < 0$. In GR, the latter condition implies that through the Einstein field equation, the stress-energy tensor violates the NEC at the throat, i.e., $T_{\mu\nu}k^\mu k^\nu|_{r_0} < 0$. We consider

$$2\Phi(r) = \frac{r_0}{r} \quad (3.2)$$

that resembles a Newtonian potential for $\Phi(r)$ in analogy to black hole physics [98, 99]. The ratio $\frac{b(r)}{r}$ is debated and its form is *a priori* unknown. Finding out the forms of $\Phi(r)$ and $b(r)$ from the field equations means to derive a Morris-Thorne-like wormhole solution. Here, we follow two physically-motivated strategies imposing

$$\frac{b(r)}{r} = \left(\frac{r_0}{r}\right)^{1+\beta}, \quad (3.3a)$$

$$\frac{b(r)}{r} = \frac{r_0}{1 + \alpha r}, \quad (3.3b)$$

with $\beta \in \mathbb{R}$ and $\beta + 1 > 0$ and $\alpha \equiv \frac{r_0 - 1}{r_0}$ to guarantee that at $r = r_0$ the wormhole is not singular.

Therefore our wormhole metric takes two possible forms

$$ds^2 = e^{r_0/r} dt^2 - \frac{1}{1 - \left(\frac{r_0}{r}\right)^{\beta+1}} dr^2 - r^2 d\Omega^2, \quad (3.4)$$

$$ds^2 = e^{r_0/r} dt^2 - \frac{1}{1 - \frac{r_0}{1 + \alpha r}} dr^2 - r^2 d\Omega^2. \quad (3.5)$$

In both cases, the expressions are polynomials characterizing b/r . To enable stability, one can require that within the whole interval of r , the ratio $b(r)/r$ does not diverge. An intriguing proposal has been shown in [99], where a shape function of the type $b(r) = r_0 \left(\frac{r_0}{r}\right)^\beta \exp\left(-\delta \frac{r-r_0}{r_0}\right)$ has been introduced. As $r - r_0 \ll 1$, it is possible to make a Taylor expansion that leads to Eq. (3.3a) that turns out to be an extension of the cases discussed in [98, 99]. Hereafter, Eq. (3.3a) will be dubbed phenomenological shape function, to stress that it has been argued from heuristic considerations.

At $r = r_0$, to avoid discontinuities in the Morris-Thorne metric, we can require the domain to be stable even before $r = r_0$. Thus, one can imagine to expand around $r = r_0$ in terms of rational expansions, made by Padé functions, widely used in recent literature [49, 100, 101]. The corresponding

ratio, constructed by means of Padé polynomials, changes dramatically the form of solutions or leaves it unaltered. As a prototype of our recipe, we take into account the simplest Padé expansion [102]. To this end, we recall that the Padé technique is built up from the standard Taylor series, being to lower divergences or singular points. Hence, given a function $f(z) = \sum_{i=0}^{\infty} c_i z^i$, expanded with a given set of coefficients, namely c_i , it is approximated by means of a (n, m) Padé approximant by the ratio [103]

$$P_{n,m}(z) = \frac{\sum_{\kappa=0}^n a_{\kappa} z^{\kappa}}{1 + \sum_{\sigma=1}^m b_{\sigma} z^{\sigma}}, \quad (3.6)$$

where the Taylor expansion matches the coefficients of the expansion up to the highest possible order

$$P'_{n,m}(0) = f'(0), \quad (3.7)$$

⋮

$$P_{n,m}^{(n+m)}(0) = f^{(n+m)}(0), \quad (3.8)$$

with the additional request $P_{n,m}(0) = f(0)$.

The numerator is thus constructed to have $n + 1$ independent coefficients, whereas in the denominator, it is m , for a total of $n + m + 1$ unknown terms. For small radii, rational expressions are essentially indistinguishable from the Taylor one, but, at larger radii, the convergence radius of rational polynomials is determined by the following practical rule [104, 105]

- I. *The most suitable rational approximation order leads to the function that maximizes the convergence radius.*
- II. *The most suitable rational approximation minimizes the involved free constants.*

Consequently a small number of free parameters is essential to enable the rational approximation to be convergent, providing the compromise between arbitrary-order expansions and minimal number of free parameters in the denominator.

The lowest Padé orders are two: (1,0) and (0,1). They turn out to be the simplest approaches to use in the framework of wormholes. We are forced to take the (0,1) order since it guarantees that all the other assumptions over the stability of b/r are preserved¹. In both cases, the asymptotic conditions are automatically satisfied, i.e. $e^{r_0/r} \rightarrow 1$ and $\frac{1}{1-b(r)/r} \rightarrow 1$ as $r \rightarrow \infty$.

We are now able to get the corresponding energy conditions and to check whether the above consistency conditions are satisfied.

Let us start with the field Eqs. (1.191) in $f(R)$ theory which can be rewritten as

$$T_{\mu\nu}^{(m)} = f_R(R)G_{\mu\nu} - \left\{ \frac{1}{2}g_{\mu\nu} \left[f(R) - Rf_R(R) \right] + f_R(R)_{;\mu\nu} - g_{\mu\nu} \square f_R(R) \right\}. \quad (3.9)$$

In order to write energy conditions [84, 92], we can choose

$$T^\mu{}_\nu = \text{diag}(\rho, -p_r, -p_t, -p_t), \quad f(R) = f_0 R^{1+\epsilon}, \quad (3.10)$$

where p_t is the tangential pressure, p_r the radial pressure and ρ the energy density, whereas $f(R)$ is a power law, with f_0 dimensional constant². For $\epsilon \ll 1$, it can be written in the form

$$f(R) \sim R + \epsilon R \ln R + \mathcal{O}(\epsilon^2), \quad (3.11)$$

corresponding to the GR plus a correction. Clearly this form is useful to control little deviations with respect to the standard Einstein's theory. Recently, this approach revealed particularly useful to study compact objects, like neutron stars and black holes, where deviations with respect to GR can be useful to fit observations [106, 107].

Here, we adopt a similar approach to investigate which cases correspond to small departures from Einstein's gravity according to the values of ϵ . As we will see below, ϵ is constrained in range of values providing wormhole solutions with vanishing sound speed. In other words, we can state that

Stable and traversable wormhole solutions are possible for small deviations of Einstein's gravity in presence of standard perfect fluid matter.

¹The expansion (1,0) corresponds to a first order Taylor expansion and does not work well to guarantee that, for $r \rightarrow \infty$, $\frac{b}{r} \rightarrow 0$. We have to check this property for all cases at the wormhole throat, namely $r_0, b(r_0)/r_0 = 1$.

²From now on we set this constant equal to 1.

Starting from (3.9) and (3.10), we get the components of the energy-momentum tensor for the generic metric (3.1)

$$\begin{aligned}
 p_r(r) = & \frac{1}{2} \left[\frac{r(r_0^2 + r(r_0 - 4r)b'(r)) - r_0(r_0 + r)b(r)}{2r^5} \right]^{1+\epsilon} \times \\
 & \left\{ \left[-\epsilon + \frac{4(1+\epsilon)r((r-r_0)b(r) + r_0r)}{r(r(4r-r_0)b'(r) - r_0^2) + r_0(r_0+r)b(r)} + \right. \right. \\
 & + \left(2\epsilon(1+\epsilon)r(r_0-4r)(r-b(r)) \left(r(r_0^2 + 4r_0r - 8r^2)b'(r) + \right. \right. \\
 & \left. \left. 4r_0^2r + r^3(4r-r_0)b''(r) - r_0(5r_0+4r)b(r) \right) \right] \times \\
 & \left. \times \left[\left(r_0(r_0+r)b(r) - r(r_0^2 + r(r_0-4r)b'(r)) \right)^2 \right]^{-1} \right\}, \quad (3.12)
 \end{aligned}$$

$$\begin{aligned}
 p_t(r) = & \frac{1}{2} \left[\frac{r(r_0^2 + r(r_0 - 4r)b'(r)) - r_0(r_0 + r)b(r)}{2r^5} \right]^{1+\epsilon} \times \\
 & \times \left\{ \left[(1 + \epsilon) \left((r_0^2 + r_0r + 2r^2) b(r) + r(r_0 - 2r)b'(r) - r_0(r_0 + 2r) \right) \right] \times \right. \\
 & \times \left[r(r_0^2 + r(r_0 - 4r)b'(r)) - r_0(r_0 + r)b(r) \right]^{-1} - \epsilon + \\
 & + \left[2\epsilon(1 + \epsilon)r^2(b(r) - rb'(r)) \left(r(-r_0^2 - 4r_0r + 8r^2)b'(r) + \right. \right. \\
 & \left. \left. - 4r_0^2r + r^3(r_0 - 4r)b''(r) + r_0(5r_0 + 4r)b(r) \right) \right] \times \\
 & \times \left[(r_0(r_0 + r)b(r) - r(r_0^2 + r(r_0 - 4r)b'(r)))^2 \right]^{-1} + \\
 & + \left[r(r_0^2 + r(r_0 - 4r)b'(r)) - r_0(r_0 + r)b(r) \right]^{-3} \times \\
 & \left[2\epsilon(1 + \epsilon)r(r - b(r)) \left[r_0^2(r_0 + r)(5r_0^2 + 54r_0r + 32r^2)b(r)^2 + \right. \right. \\
 & + r_0rb(r) \left(-r_0^2(9r_0^2 + 90r_0r + 64r^2) + \right. \\
 & - (r_0^4 + 28r_0^3r + 80r_0^2r^2 - 192r_0r^3 - 160r^4)b'(r) + \\
 & + r^2(r_0 + r) \left((3r_0^2 + 8r_0r - 24r^2)b''(r) - 2r^2(r_0 - 4r)b^{(3)}(r) \right) \left. \right) \left. \right] + \\
 & + r^2 \left(4(r_0^5 + 8r_0^4r + 2(\epsilon - 1)r^{13}) + \right. \\
 & + r(r_0 - 4r)(r_0 + 2r)(r_0^2 + 20r_0r - 16r^2)b'(r)^2 + \\
 & + r_0^2r^2 \left((-3r_0^2 - 8r_0r + 24r^2)b''(r) + 2r^2(r_0 - 4r)b^{(3)}(r) \right) + \\
 & b'(r) \left(r^3(r_0 - 4r) \left((-3r_0^2 - 8r_0r + 24r^2)b''(r) + 2r^2(r_0 - 4r)b^{(3)}(r) \right) + \right. \\
 & \left. \left. + r_0^2(r_0^3 + 26r_0^2r + 40r_0r^2 - 160r^3) \right) \right] \left. \right\}. \tag{3.13}
 \end{aligned}$$

$$\begin{aligned}
\rho(r) = & \frac{1}{2} \left[\frac{r(r_0^2 + r(r_0 - 4r)b'(r)) - r_0(r_0 + r)b(r)}{2r^5} \right]^{1+\epsilon} \times \\
& \times \left\{ \epsilon - \frac{4(1+\epsilon)r^3b'(r)}{r(r(4r - r_0)b'(r) - r_0^2) + r_0(r_0 + r)b(r)} + \right. \\
& + \left[2\epsilon(1+\epsilon)r^2(rb'(r) - b(r)) \left(r(-r_0^2 - 4r_0r + 8r^2)b'(r) + \right. \right. \\
& \left. \left. - 4r_0^2r + r^3(r_0 - 4r)b''(r) + r_0(5r_0 + 4r)b(r) \right) \right] \times \\
& \times \left[(r_0(r_0 + r)b(r) - r(r_0^2 + r(r_0 - 4r)b'(r)))^2 \right]^{-1} + \\
& - \left[r(r_0^2 + r(r_0 - 4r)b'(r)) - r_0(r_0 + r)b(r) \right]^{-3} \times \\
& \times \left[2\epsilon(1+\epsilon)r(r - b(r)) \left[r_0^2(r_0 + r)(5r_0^2 + 44r_0r + 24r^2)b(r)^2 + \right. \right. \\
& + r_0rb(r) \left(r^2(r_0 + r) \left((3r_0^2 + 6r_0r - 16r^2)b''(r) - 2r^2(r_0 - 4r)b^{(3)}(r) \right) + \right. \\
& - 3r_0^2(3r_0^2 + 24r_0r + 16r^2) + r^2 \left(4(r_0^5 + 6r_0^4r + 2(\epsilon - 1)r^{13}) + \right. \\
& - (r_0^4 + 26r_0^3r + 60r_0^2r^2 - 152r_0r^3 - 112r^4)b'(r) \left. \right) + \\
& + r(r_0 - 4r)(r_0^3 + 20r_0^2r + 16r_0r^2 - 16r^3)b'(r)^2 + \\
& + r_0^2r^2 \left((-3r_0^2 - 6r_0r + 16r^2)b''(r) + 2r^2(r_0 - 4r)b^{(3)}(r) \right) + \\
& + b'(r)(r^3(r_0 - 4r) \left((-3r_0^2 - 6r_0r + 16r^2)b''(r) + 2r^2(r_0 - 4r)b^{(3)}(r) \right) + \\
& \left. \left. + r_0^2(r_0^3 + 24r_0^2r + 24r_0r^2 - 112r^3) \right) \right] \left. \right\}, \tag{3.14}
\end{aligned}$$

Here, the form of $b(r)$ is not specified. If we consider the energy-momentum tensor for perfect fluids written in the form $T^\mu{}_\nu = \text{diag}(\rho, -p, -p, -p)$, the

average pressure is $p(r) = \frac{1}{3} [p_r(r) + 2p_t(r)]$, and then

$$\begin{aligned}
p(r) = & \frac{1}{6} \left[\frac{r(r_0^2 + r(r_0 - 4r)b'(r)) - r_0(r_0 + r)b(r)}{2r^5} \right]^{1+\epsilon} \times \\
& \times \left\{ \frac{4(1+\epsilon)r((r-r_0)b(r) + r_0r)}{r(r(4r-r_0)b'(r) - r_0^2) + r_0(r_0+r)b(r)} - \epsilon + \right. \\
& + \left[2\epsilon(1+\epsilon)r(r_0-4r)(r-b(r)) \left(r(r_0^2 + 4r_0r - 8r^2) b'(r) + \right. \right. \\
& + \left. \left. 4r_0^2r + r^3(4r-r_0)b''(r) - r_0(5r_0+4r)b(r) \right) \right] \times \\
& \times \left[(r_0(r_0+r)b(r) - r(r_0^2 + r(r_0-4r)b'(r)))^2 \right]^{-1} + \\
& + 2 \left[-\epsilon + \left[(1+\epsilon) \left((r_0^2 + r_0r + 2r^2) b(r) + \right. \right. \right. \\
& + \left. \left. \left. r(r(r_0-2r)b'(r) - r_0(r_0+2r)) \right) \right] \right] \times \\
& \times \left[r(r_0^2 + r(r_0-4r)b'(r)) - r_0(r_0+r)b(r) \right]^{-1} + \\
& + \left[2\epsilon(1+\epsilon)r^2(b(r) - rb'(r)) \left(r(-r_0^2 - 4r_0r + 8r^2) b'(r) + \right. \right. \\
& - \left. \left. 4r_0^2r + r^3(r_0-4r)b''(r) + r_0(5r_0+4r)b(r) \right) \right] \times \\
& \times \left[(r_0(r_0+r)b(r) - r(r_0^2 + r(r_0-4r)b'(r)))^2 \right]^{-1} + \\
& + \left[r(r_0^2 + r(r_0-4r)b'(r)) - r_0(r_0+r)b(r) \right]^{-3} \times \\
& \times \left[2\epsilon(1+\epsilon)r(r-b(r)) \left(r_0^2(r_0+r) (5r_0^2 + 54r_0r + 32r^2) b(r)^2 + \right. \right. \\
& + r_0rb(r)(r^2(r_0+r) ((3r_0^2 + 8r_0r - 24r^2) b''(r) - 2r^2(r_0-4r)b^{(3)}(r)) + \\
& - r_0^2(9r_0^2 + 90r_0r + 64r^2) + \\
& - (r_0^4 + 28r_0^3r + 80r_0^2r^2 - 192r_0r^3 - 160r^4) b'(r)) + \\
& + r^2(4(r_0^5 + 8r_0^4r + 2(\epsilon-1)r^{13}) + \\
& + r(r_0-4r)(r_0+2r)(r_0^2 + 20r_0r - 16r^2) b'(r)^2 + \\
& + r_0^2r^2((-3r_0^2 - 8r_0r + 24r^2) b''(r) + 2r^2(r_0-4r)b^{(3)}(r)) + \\
& + b'(r)(r^3(r_0-4r)((-3r_0^2 - 8r_0r + 24r^2) b''(r) + 2r^2(r_0-4r)b^{(3)}(r)) + \\
& \left. \left. \left. + r_0^2(r_0^3 + 26r_0^2r + 40r_0r^2 - 160r^3) \right) \right) \right] \right] \left. \right\}. \tag{3.15}
\end{aligned}$$

In this way, the null energy condition [84, 92] at the throat, for the metric (3.4), that is for $\frac{b(r)}{r} = \left(\frac{r_0}{r}\right)^{\beta+1}$, is expressed as

$$\begin{aligned} \rho + p|_{r_0} = & \left[3(1 - 3\beta)^2\right]^{-1} \left\{ (1 + \epsilon) \left(\frac{3\beta - 1}{2r_0^2}\right)^{1+\epsilon} [6 + \beta - 3\beta^2(8 + \beta) + \right. \\ & \left. + (1 + \epsilon)[-5 + \beta(1 + 3\beta(3 + \beta))]] \right\} \geq 0, \end{aligned} \quad (3.16)$$

while, for the metric (3.5), i.e. for $\frac{b(r)}{r} = \frac{r_0}{1+\alpha r}$, it is

$$\begin{aligned} \rho + p|_{r_0} = & - \left\{ (1 + \epsilon) \left(-\frac{r_0 + 3}{2r_0^3}\right)^{1+\epsilon} \left[(r_0 - 1)[r_0(5r_0 + 9) - 6](1 + \epsilon) + \right. \right. \\ & \left. \left. - 2[r_0(3r_0^2 + r_0 - 15) + 3] \right] \right\} [3r_0(r_0 + 3)^2]^{-1} \geq 0. \end{aligned} \quad (3.17)$$

Another aspect to check is the flare-out condition [108]

$$\left. \frac{b'(r)r - b(r)}{2b(r)^2} \right|_{r_0} < 0, \quad (3.18)$$

which becomes, for the metric (3.4) at the throat

$$-\frac{1 + \beta}{2r_0} < 0 \quad \rightarrow \quad \beta > -1. \quad (3.19)$$

In the other case, it is fulfilled for

$$-\frac{r_0 - 1}{2r_0^2} < 0 \quad \rightarrow \quad r_0 > 1, \quad (3.20)$$

provided that $r_0 > 0$. The consistency of our model is guaranteed in both cases. These results allow to give necessary conditions on the function $b(r)/r$ but they are not sufficient to show that the form of $b(r)$ is of the form of a polynomial. To ensure this hypothesis, we assume that the sound speed, i.e. the variation of the pressure with respect to the density, is negligibly small [109]. Combining this additional requirement, we stabilize the solution as we shall show below.

3.1.2 The stability condition and the sound speed

We require the solutions to be stable, besides being traversable. This reflects to the stability of fluids inside the throat, with the hypothesis of satisfying the above energy conditions.

Thus, let us consider the perturbation condition by means of the adiabatic sound speed, c_s , i.e. we assume the sound speed definition in adiabatic perturbations, in analogy to what happens in fluid dynamics [110, 111]. So, defining the adiabatic sound speed by [112, 113, 114]

$$c_s^2 = \left(\frac{\partial p}{\partial \rho} \right)_S, \quad (3.21)$$

we can guarantee how perturbations affect solutions analyzing its value within the throat. Hence, the sound speed is essential to guarantee the viability of our approximated versions of b/r . The above expression for c_s can be specified as

$$\left. \frac{dp}{d\rho} \right|_{r_0} = 0. \quad (3.22)$$

Plugging Eqs. (3.14) and (3.15) in Eq. (3.22) and considering $\frac{b(r)}{r} = \left(\frac{r_0}{r} \right)^{\beta+1}$, we get the following stability condition for the metric (3.4)

$$\begin{aligned} & 147 - 32r_0^8 \epsilon(\epsilon - 1)(1 + \beta) - 4(1 + \epsilon)^2(1 + \beta)[5 - 3\beta(2 + \beta)]^2 + \\ & + \beta\{-428 + \beta[-926 + 3\beta(148 + \beta(161 + 24\beta))]\} + \\ & - (1 + \epsilon)\{45 + \beta[-288 + \beta(-658 + 3\beta(60 + \beta(95 + 12\beta)))]\} \times \\ & \times \left\{ 3 \left[16r_0^8 \epsilon(\epsilon - 1)(1 + \beta) + 2(1 + \epsilon)^2(1 + \beta)[5 - 3\beta(2 + \beta)]^2 + \right. \right. \\ & - 55 + (1 + \epsilon)(1 + \beta)[5 + \beta(-113 + 3\beta(-37 + \beta(19 + 6\beta)))] + \\ & \left. \left. + \beta[166 - \beta(-400 + 3\beta(38 + \beta(67 + 12\beta)))] \right] \right\}^{-1} = 0. \quad (3.23) \end{aligned}$$

Similarly, by considering $\frac{b(r)}{r} = \frac{r_0}{1 + \alpha r}$, we get the stability condition for the metric (3.5)

$$\begin{aligned} & \frac{1}{3} \left\{ -2 - r_0(r_0 + 3) \left[r_0(r_0^2(35(1 + \epsilon) - 37) - 12r_0(\epsilon + 2) - 177(1 + \epsilon) + \right. \right. \\ & + 135) + 90(1 + \epsilon) - 54 \left. \right] \left[r_0 + 36(7 - 5(1 + \epsilon)) + (-714 + r_0(393 + \right. \\ & + r_0(389 + r_0(-137 + r_0(32(r_0 - 1)r_0^7 - 55)))) + r_0(1 + \epsilon)(354 + \\ & + r_0(-39 + r_0(-163 + r_0(-48r_0^9 + 48r_0^8 + 5r_0 + 23)))) + 2(r_0 - 1)(1 + \epsilon)^2 \times \\ & \left. \left. \times (36 + r_0(-108 + r_0(21 + r_0(8r_0^9 + 25r_0 + 90)))) \right]^{-1} \right\} = 0. \end{aligned} \quad (3.24)$$

We can therefore analyze the consequence of such conditions for our wormhole solutions as reported in the next subsection. The corresponding results are clearly numerical since no analytical solutions can be obtained integrating the above stability conditions³ coming from $c_s = 0$.

3.1.3 The wormhole solutions

In the case of metric (3.4), we have determined a class of wormhole solutions satisfying the three above conditions, namely the null energy condition (3.16), the flare-out condition (3.19) and the stability condition (3.23). In particular, once the value of the β parameter is fixed, we determine the wormhole throat (as a function of ϵ) and the values of ϵ that satisfy Eqs. (3.16), (3.19), (3.23) and the condition $r_0 > 0$. We have summarized the results obtained in Table 3.1. In particular, we note that $\epsilon = \frac{1}{2}$, i.e. $f(R) = R^{3/2}$, is obtained in three cases⁴

1. $\beta = 7 \Rightarrow r_0 \simeq 3.632$;
2. $\beta = 8 \Rightarrow r_0 \simeq 3.862$;
3. $\beta = 9 \Rightarrow r_0 \simeq 4.078$.

³The assumption $c_s = 0$ is also used in astrophysics to guarantee stability of virialized structures. See e.g. [115].

⁴ $f(R)$ gravity with $1 + \epsilon = 3/2$ is particularly relevant for cosmological and astrophysical applications. It is related to invertible conformal transformation [55]. It allows a curvature interpretation of dark matter phenomena according to MOND [116] and the transition from decelerated to accelerated regimes in cosmology [117].

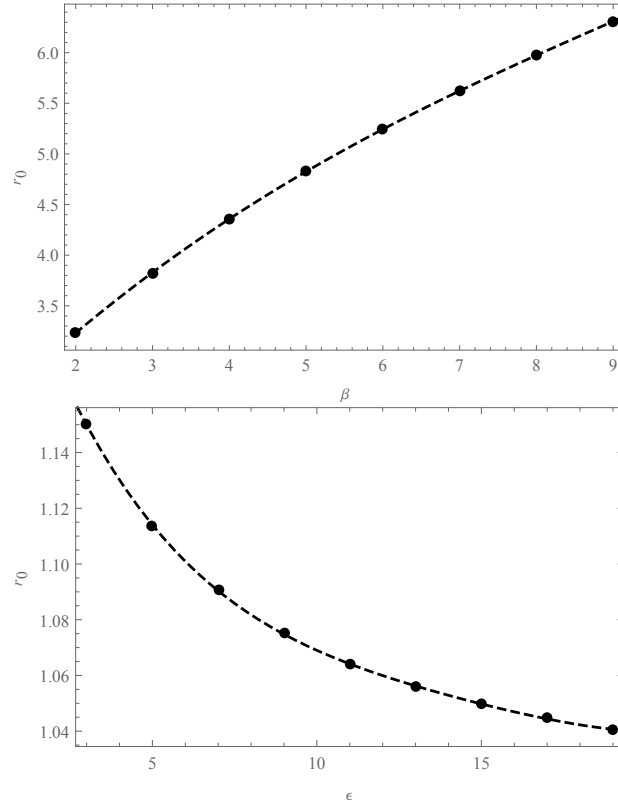


Figure 3.1: *Interpolations of r_0 vs β and of r_0 vs ϵ . The curves have been obtained through Wolfram Mathematica and represent an extrapolation based on the fitting functions $3.03 \cdot 10^{-5}x^4 + 1.13 \cdot 10^{-3}x^3 - 4.65 \cdot 10^{-2}x^2 + 8.01 \cdot 10^{-1}x + 1.79$ and $2.43 \cdot 10^{-6}x^4 - 1.43 \cdot 10^{-4}x^3 + 3.30 \cdot 10^{-3}x^2 - 3.80 \cdot 10^{-2}x + 1.24$ respectively for the left and right plots.*

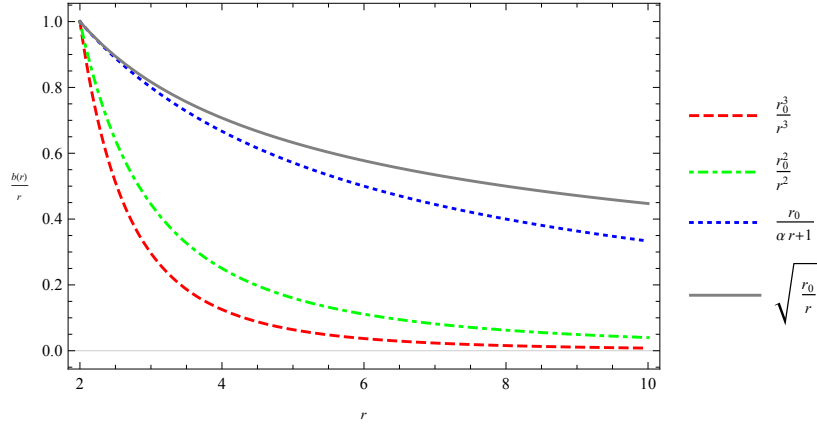


Figure 3.2: Comparison between the shape functions of our models (red and blue lines), the standard approach proposed in [91] (grey line) and the model proposed in [99] (green line). The value of the β parameter chosen for our model (3.3a) is $\beta = 2$. Our Padé expansion better adapts to the standard approach than other phenomenological ansatz.

β	r_0	ϵ
0	$\frac{1275}{128}$	$\frac{1}{5}$
1	no solution	no solution
2	$\sqrt[8]{\frac{5332\epsilon^2+14653\epsilon+150}{96\epsilon-96\epsilon^2}}$	$-2.986 \lesssim \epsilon < -1 \cup 0.965 \lesssim \epsilon < 1$
3	$\sqrt[8]{\frac{2(100\epsilon^2+317\epsilon-14)}{(1-\epsilon)\epsilon}}$	$-3.213 \lesssim \epsilon < -1 \cup 0.800 \lesssim \epsilon < 1$
4	$\sqrt[8]{\frac{89780\epsilon^2+289269\epsilon-9922}{160(1-\epsilon)\epsilon}}$	$-3.256 \lesssim \epsilon < -1 \cup 0.689 \lesssim \epsilon < 1$
5	$\sqrt[8]{\frac{15000\epsilon^2+48455\epsilon-1372}{12(1-\epsilon)\epsilon}}$	$-3.258 \lesssim \epsilon < -1 \cup 0.607 \lesssim \epsilon < 1$
6	$\sqrt[8]{\frac{540988\epsilon^2+1744781\epsilon-42194}{224(1-\epsilon)\epsilon}}$	$-3.249 \lesssim \epsilon < -1 \cup 0.542 \lesssim \epsilon < 1$
7	$\sqrt[8]{\frac{8464\epsilon^2+27216\epsilon-575}{2(1-\epsilon)\epsilon}}$	$-3.236 \lesssim \epsilon < -1 \cup 0.489 \lesssim \epsilon < 1$
8	$\sqrt[8]{\frac{1988100\epsilon^2+6370997\epsilon-119554}{288(1-\epsilon)\epsilon}}$	$-3.223 \lesssim \epsilon < -1 \cup 0.446 \lesssim \epsilon < 1$
9	$\sqrt[8]{\frac{213160\epsilon^2+680759\epsilon-11492}{20(1-\epsilon)\epsilon}}$	$-3.210 \lesssim \epsilon < -1 \cup 0.409 \lesssim \epsilon < 1$

Table 3.1: Wormhole solutions for different values of the β parameter. Here we adopted the parametrization given in Eq. (3.3a). The allowed range values of ϵ are also reported.

ϵ	r_0
0	no solution
2	1.150
4	1.114
6	1.090
8	1.075
10	1.064
12	1.056
14	1.050
16	1.045
18	1.040

Table 3.2: Wormhole solutions for different values of ϵ . Here we adopted the parametrization given in Eq. (3.3b).

These correspond to three wormhole metrics, respectively

1. $ds^2 = e^{r_0/r} dt^2 - \frac{1}{1 - \left(\frac{r_0}{r}\right)^8} dr^2 - r^2 d\Omega^2$;
2. $ds^2 = e^{r_0/r} dt^2 - \frac{1}{1 - \left(\frac{r_0}{r}\right)^9} dr^2 - r^2 d\Omega^2$;
3. $ds^2 = e^{r_0/r} dt^2 - \frac{1}{1 - \left(\frac{r_0}{r}\right)^{10}} dr^2 - r^2 d\Omega^2$.

In the case of metric (3.5), the validity of NEC (3.17) points out that $1 + \epsilon$ must be an integer. For ϵ integer and odd, we found no solutions satisfying also the flare-out condition (3.20). Consequently the only solutions that satisfy all three conditions (3.17), (3.20) and (3.24) are those with ϵ integer and even. Therefore, once the value of ϵ is fixed, we determine the corresponding wormhole throat. The results are summarized in Table 3.2. We note that $\epsilon = 0$, implying GR, leads to no solutions as the NEC is not satisfied. The theoretical consequences of our approach are summarized below.

3.2 Theoretical considerations

We assumed a power-law form for $f(R)$, where GR is recovered for $\epsilon = 0$. From our analyses, it is possible to provide two classes of the shape function

$b(r)/r$. The first possibility, already adopted in literature, represents a class of inverse powers with respect to r [98, 99]. This approach departs significantly from the one provided in the original work by Morris and Thorne [91] as it appears evident from Fig. 3.1. Even though appealing, these possibilities are therefore disfavored than the Padé expansion that we proposed above. The $(0,1)$ Padé polynomial resembles much more the Morris-Thorne shape function and candidates as a suitable approach that turns out to be *model-independent* in reconstructing b/r . The expansion of b/r is constructed by means of rational series. The only dependence from the model occurs as one chooses the order (n, m) . This approach is significantly better than *ad hoc* functions postulated at the beginning over b . In this respect, it is possible to provide two cases summarized in Tabs. I and II. In Tab. I, we consider the case of inverse power law approximation. It appears evident that the case $f \sim R^2$ is not recovered indicating small departures from the Starobinsky scalaron model [52]. The inverse solution, i.e. $1 + \epsilon$ negative, is not excluded. In this case the repulsive effects are stronger than the case of positive $1 + \epsilon$. On the other hand, the Padé approximation excludes GR as well as the previous case but shows very small departures from r_0 , indicating moreover that the Starobinsky scalaron is excluded again. In particular, the energy conditions are not fulfilled in the case of odd ϵ . The results are well-suited in the Padé scenario and candidate to reconstruct the shape function without imposing any *ad hoc* functions. In all the aforementioned cases, it is possible to notice that ϵ is quite small, confirming that only small deviations from GR are permitted as soon as one considers wormholes in extended theories of gravity with vanishing sound speed.

3.2.1 Final remarks

We discovered a class of exact traversable wormhole solutions. There are currently no experiments that can directly observe a wormhole. However, possible tests, similar to those discussed in the previous sections, are being investigated, particularly time delay and gravitational redshift. Our idea is to use the approaches discussed in Ref. [118] to our wormhole solution. Considering that this solution was found in a specific $f(R)$ theory (power-law type), such a test would allow us to fix the $f(R)$ theory constraints in the strong field. As a result, we would be able to conduct a comprehensive test of the theory on every energy scale, combining the results obtainable in the weak field (see Sec. 1.3.2 and Sec. 1.4) with those obtainable in the strong field.

Chapter 4

Experimental tests of gravity

Galileo Galilei described the so-called “scientific method” for the first time in the history of science and philosophy in his 1632 work [119]. Today researchers are still guided by “*sensible experiences and necessary demonstrations*” to understand natural phenomena. Events observation is the first step toward knowledge, followed by mathematical hypothesis formulation. The process culminates in the experimental tests of the theoretical model, allowing for its definitive validation and, therefore, its conversion from hypothesis to natural law. Theory and experiment are, in this sense, two sides of the same coin, two aspects of scientific research that are inextricably intertwined. In other words, one cannot exist without the other.

In this chapter, we look at the final step of the scientific method, focusing on a widely employed technique, in the weak field, in testing the previously examined theoretical models. It is organized as follows. We begin by introducing the LR, which has been for years and still is one of the most reliable methods for getting measurements of theoretical parameters in the Solar System. Following that, we lay a particular emphasis on the optical components of the LR system. We show the last results of optical simulations of the laser retroreflectors implemented in this technique, focusing on two space missions, LARES-2 and MoonLIGHT. Finally, we analyze the data collected so far, which are currently being processed with PEP.

4.1 The Laser Ranging

At the end of the 1950s, a gravitational research group led by R. H. Dicke at Princeton University was developing an experiment to measure possible variations in the gravitational constant G [120]. Thus, the concept of sending laser pulses from ground stations to optical retroreflectors on Earth-orbiting satellites was born. When NASA used ruby lasers to point towards the Beacon Explorer 22 (BE-B) satellite for the first time in 1964, it was clear that this technique, known as LR, could have provided a lot of information if used with artificial satellites as well as natural ones, like the Moon.



Figure 4.1: *Matera LR Observatory of the Italian Space Agency (ASI). Credits: Dr. G. Bianco (ASI - Space Geodesy Center (CGS)).*

In general, the LR technique involves the measurements of the time of flight

(ToF) of short laser pulses fired from International Laser Ranging Service¹ (ILRS) stations on Earth to CCRs placed on a satellite and then retro-reflected back to Earth. If the satellite is the Moon, we refer to it as Lunar Laser Ranging (LLR); otherwise, we refer to it as Satellite Laser Ranging (SLR). LR, then, provides an indirect measure of the distance between the station and the satellite.

We must consider several factors when performing LF measurements. First of all, the atmosphere diverts the laser by a few arcseconds, resulting in a beam that is many kilometers wide when it reaches the satellite. For example, 1 arcsec corresponds to approximately 1.8 km on the Moon. Additionally, the laser beam diverges as it returns to Earth, both due to the atmosphere and the diffraction caused by the CCRs. All of this causes a total enlargement of the order of ten kilometers (in the case of the Earth-Moon, the laser beam will have a diameter of about 15 km, see Fig. 4.2). Furthermore, each laser pulse sent by the stations contains approximately 300 quadrillion photons, but only a fraction will hit the retroreflectors and then return to Earth (about 1 part in 30 million).

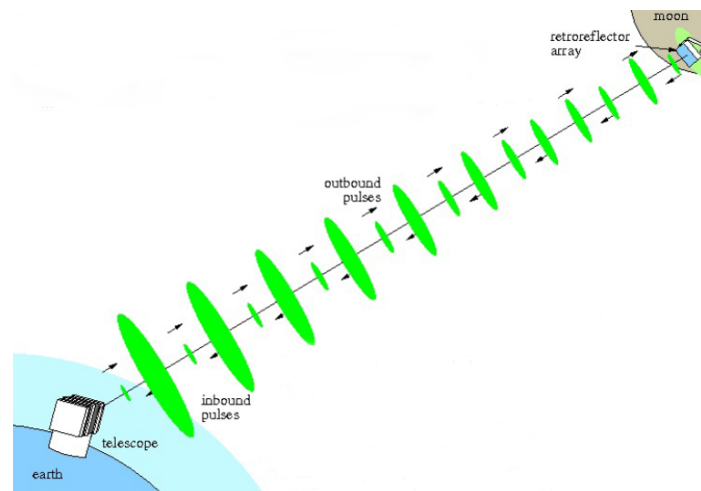


Figure 4.2: *LLR operation diagram.*

¹ILRS was founded in September 1998 to support geodesy, geophysics, and lunar science research programs. It collaborates on the design and construction of retroreflectors for new satellite missions in order to maximize the quality and quantity of data collected, as well as on scientific programs to optimize data collection.

Moreover, if the satellite is natural, its physical characteristics must be considered, such as the effects of librations and regolith motion on the Moon. Finally, the relative motion between the Earth and the satellite causes the VA, see Eq. (2.83). Therefore, improving the accuracy of LR measurements is a challenging but ambitious goal.

4.2 Cube Corner Retroreflectors

In this section, we analyze, in detail, one of the fundamental optical components in realizing the LR: the CCR.

CCRs are devices made up of three perpendicular reflecting surfaces (making a cube angle) that retroreflect light back in the same direction it came. Each reflection inverts a component of the incoming light's velocity vector, with components V_x , V_y , and V_z . After three reflections, the velocity components are $-V_x$, $-V_y$, and $-V_z$, and the light returns to the source (see Fig. 4.3).

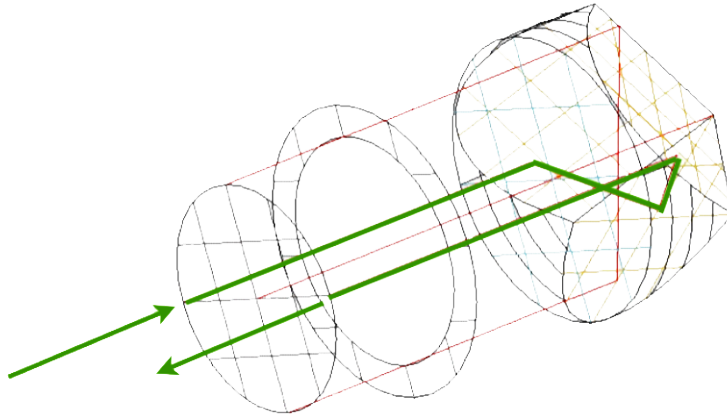


Figure 4.3: *Operation diagram of the light reflection inside the CCR. Credits: SCF_Lab group (INFN - LNF).*

However, we have to emphasize that the reflected beam is precisely (anti) parallel to the incident one only if the CCR is perfect, that is, if the angles between the reflecting surfaces are exactly 90° or, alternatively, if all Dihedral Angle Offsets are zero (DAOs = $(0, 0, 0)$ arcsec). Otherwise, if any

of the DAOs is even slightly different from zero, it will split into two, four, or six beams depending on whether one, two, or all three angles are not 90° [121]. Furthermore, we observe that since a CCR is made up of three reflective faces, a ray must hit each face at least once to be retroreflected, and there are six possible ways to achieve it. This results in six possible ray paths within the CCR, each of which could have different polarization properties [122]. CCRs are typically made of fused silica and are installed in passive, lightweight, maintenance-free, and long-lasting Laser Retroreflector Arrays (LRAs). There are different types of CCRs; however, we will focus on uncoated and coated CCRs. The term *uncoated* CCRs refers to those that do not have a metallic coating on the inside. Their functionality is based on Total Internal Reflection (TIR) since the angle of incidence of a light beam on the CCR's back face exceeds the critical angle between glass and air (or glass and vacuum), which is approximately 45° . This minimizes the possibility of thermal effects that would occur in the absence of TIR, as some of the energy carried by the light would pass through the back faces of the CCR, causing perturbations. Uncoated CCRs have an approximately 17° field of view. The effects of polarization are significant for them: if the incident beam has only one type of polarization, either vertical or horizontal, the one that emerges from the CCR will have both types of polarization. Due to their properties, uncoated CCRs are well-suited for high orbits (as in the Earth-Moon system). Conversely, the CCRs *coated's* main feature is the reflective metallic film that covers their back. As a result, they operate via metallic reflection. This internal coating can absorb some of the laser beam's energy and convert it into heat. Consequently, they are subject to thermal gradients, unlike the previous ones. Coated CCRs have a field of view of approximately 56° , therefore greater than uncoated ones. Additionally, polarization has no effect: the outgoing beam's polarization is identical to that of the incoming laser. Due to these characteristics, coated CCRs are primarily employed in low orbits.

To analyze the optical response of a CCR when hit by a laser beam, we must first introduce some quantities, such as its peak cross-section, and its Far Field Diffraction Pattern (FFDP).

The Optical Cross-section (OCS) of a CCR provides a measure of the maximum amount of radiant energy reflected by the device towards the source. For a CCR with a circular section of area A , illuminated by a laser at a

wavelength λ , the OCS is defined as

$$\text{OCS} = \frac{A^2}{\pi (1.22\lambda)^2}. \quad (4.1)$$

It, therefore, has the dimensions of an area; typically, we express it in million square meters.

Let us consider a λ -wavelength light beam incident perpendicularly on the circular surface of a CCR with a diameter² of D .

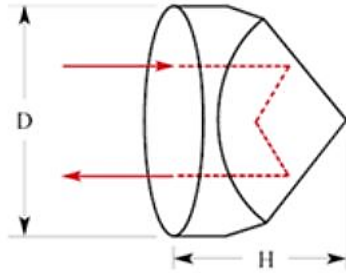


Figure 4.4: Normal incidence on the circular surface of the CCR [123]. Here, D is the diameter of the CCR, H its height. H is related to D by $H = \frac{\sqrt{2}}{2}D$.

Credits: J. J. Degnan.

The cross-section peak [123] is defined as

$$\sigma_{cc} = \frac{\pi^3 \rho D^4}{4\lambda^2}, \quad (4.2)$$

where ρ denotes the reflectivity, which varies depending on the type of CCR considered. To be precise, $\rho = 0.78$ for a coated CCR, and $\rho = 0.93$ for an uncoated one. According to Eq. (4.2), the peak intensity is proportional to the fourth power of the diameter and to the reflectivity for normal incidence. Additionally, it is inversely proportional to the wavelength's square root. This implies that, fixed the reflectivity and the laser beam wavelength, the peak

intensity of CCRs with larger diameters should be much higher.

However, in the case of non-normal incidence, the peak cross-section is reduced by an amount

$$\eta(\theta_{\text{inc}}) = \frac{2}{\pi} \left(\sin^{-1} \sqrt{1 - \tan^2 \theta_{\text{ref}}} - \sqrt{2} \tan \theta_{\text{ref}} \right) \cos \theta_{\text{inc}}. \quad (4.3)$$

Here, θ_{inc} is the incidence angle of the laser beam, while θ_{ref} is the angle of refraction, which is related to the first by Snell's law

$$\theta_{\text{ref}} = \sin^{-1} \left(\frac{\sin \theta_{\text{inc}}}{n} \right), \quad (4.4)$$

² D is also known as the CCR's aperture.

with n the cube index of refraction. In other words,

$$\sigma_{\text{eff}}(\theta_{\text{inc}}) = \eta^2(\theta_{\text{inc}})\sigma_{cc}. \quad (4.5)$$

The FFDP is the angular distribution of the intensity of the returning light (from the CCR towards the source). Since the retroreflector has a circular aperture, the FFDP approaches that of the Airy disk pattern

$$\sigma(x) = \sigma_{cc} \left[\frac{2J_1(x)}{x} \right]^2, \quad (4.6)$$

where the argument x is related to the off-axis angle³ θ by

$$x = \frac{\pi D}{\lambda} \sin \theta. \quad (4.7)$$

Instead, $J_1(x)$ is the Bessel function of order 1

$$J_1(x) = \frac{x}{2} \sum_{m=0}^{\infty} \frac{(-1)^m}{m!(m+1)!} \left(\frac{x}{2}\right)^{2m}. \quad (4.8)$$

In general, the FFDP of an uncoated CCR differs from that of a coated CCR. In fact, we should remember that polarization effects are significant for the former. These effects involve a phase shift between the six paths of the light ray inside the CCR. As a result, the FFDP consists of a central circle surrounded by six lesser-intensity lateral lobes. Indeed, the peak cross-section of each lateral lobe is proportional to σ_{cc} by a factor equal to $1/(2N)^2$, with N the number of cubic angles [123]. Additionally, when a CCR is uncoated, the intensity of the central peak is reduced by 26% compared to the case of a perfectly circular aperture (Airy disk) [124]. A coated CCR, on the other hand, is not sensitive to polarization, hence its FFDP is very similar to that of an Airy disk, with only a central lobe (at most surrounded by rings of lesser intensity).

In conclusion, OCS plot and FFDP are essential for understanding the return of light observed when the laser comes back to the station. However, these must be examined in light of the VA. Indeed, to ensure that as much signal as possible reaches the station, which has moved relative to the satellite by an angle equal to the VA since the laser was sent, we must ensure that there is an optical return to the central peak or at least to the outer rings of the diffraction pattern.

³The off-axis angle of a mirror is the angle between its optical and focal axes.

4.3 Optical simulations with Code V

Optical simulations of CCR response are performed with *Code V*, a software developed by the American company Synopsys. It is used to model, optimize, and investigate optical systems in a multitude of applications. It is particularly useful in the aerospace section, where it provides analyses on the characteristics of

- retroreflectors,
- mirrors,
- IR spectrometers,
- telescopes,
- coronagraphs,
- catadioptrics,
- stellar interferometers,
- optics for CMB experiments.

Besides, one of its most important aerospace applications was the lens correction for the Hubble Space Telescope. Code V features a graphical user interface that enables command entry and simulation execution. However, the software also supports the use of macros written in Macro PLUS programming language⁴. In this way, his basic capabilities can be “expanded”, allowing Code V to investigate many other physical situations.

With the SCF_Lab⁵ group of the Frascati National Laboratories, we specifically deal with the optical simulations of those CCRs implemented in the LR space missions, on which we are currently working. In order to achieve this, we employ the Macro programming language. We initialize each macro by inserting the specifications of the CCR we want to analyze, that is

- diameter (or aperture),
- DAOs,

⁴Macros are written on a text editor and then interpreted by the software.

⁵Satellite/lunar/GNSS laser ranging/altimetry and Cube/microsat Characterization Facilities Laboratory.

- type of polarization,
- laser beam wavelength,
- incidence angle of the laser beam on the CCR's circular surface,
- material,
- reflectivity.

Additionally, the grid's dimensions and spacing are appropriately entered to produce an image with the desired resolution and size. After that, we implement Eqs. (4.2) - (4.6), described in the previous section, in the programming language. Thus, each run produces three plots

1. the average energy distribution,
2. the energy distribution of the total pattern as a function of the VA, integrated over the azimuth⁶,
3. the energy distribution of the total pattern as a function of the azimuth, fixed the VA,

in other words, the OCS plot and the FFDP. This enables us to compare the simulated results, which are based on theoretical predictions, with the experimental tests obtained at the SCF_Lab group laboratory. The combination of optical simulations and laboratory tests enables us to fully understand the CCR's behavior once launched into space.

All simulations performed are summarized in Tab. 4.1 and are available at the SCF_Lab group. In the next sections, we show only some of these, focusing on LARES-2 and MoonLIGHT missions.

⁶The plot is the result of the integration of the intensity plots as a function of the VA for each azimuth angle value $\theta \in [0, 2\pi]$.

CCRs diameters (mm) and corresponding space missions	7.16 (Asteroids/Phobos), 10/12.7 (Earth observations), 25.4 (LARES-2), 38.1 (LAGEOS/LARES), 50/50.8/63.5 (of purely academic interest), 75/76.2 (Earth-Moon L1), 100 (MoonLIGHT).
CCRs Dihedral Angle Offsets (arcsec)	(0.1, 0.1, 0.5), (0.1, 0.5, 0.1), (0.5, 0.1, 0.1), (0.5, 0.5, 0.5), (0.25, 0.25, 0.25), (0.75, 0.75, 0.75), (-0.5, -0.5, -0.5), (-0.25, -0.25, -0.25), (-0.75, -0.75, -0.75), (1, 1, 1), (-1, -1, -1).
CCRs coating	Uncoated, coated.
Laser beam polarization	Linear, circular.
Laser beam wavelenght (nm)	532, 1064.

Table 4.1: *List of simulations available at the SCF_Lab group (INFN - LNF).*

4.3.1 LARES-2

LARES-2 is a new satellite that will be launched into orbit around the Earth. It is an improved version of the previous LARES, LAGEOS⁷, and LAGEOS2 missions. The main goal of LARES-2 is to provide tests of gravitational theories in the Solar System. It was specifically designed, like the previous ones, to measure the Lense-Thirring effect (see Sec. 1.5). Since it is a weak phenomenon in the Solar System, observing it requires a high level of accuracy. LARES-2 has been designed with specific characteristics to achieve this. It is a spherical passive satellite made of a single block of nickel alloy of high density. It is covered with 303 uncoated CCRs of 25.4 mm diameter. The satellite has a diameter of 420 mm and a mass of ~ 395 kg. It will be launched into a nearly circular orbit (eccentricity approximately 0.0025), at an altitude of 5890 km. All of these characteristics aim to minimize the surface to mass ratio and thus the effects of radiation pressure, atmospheric resistance, and thermal anisotropies.

However, perturbations caused by the Earth's deviance from spherical symmetry must be considered as well. The gravitational potential of the Earth

⁷LASer GEOdynamics Satellites.

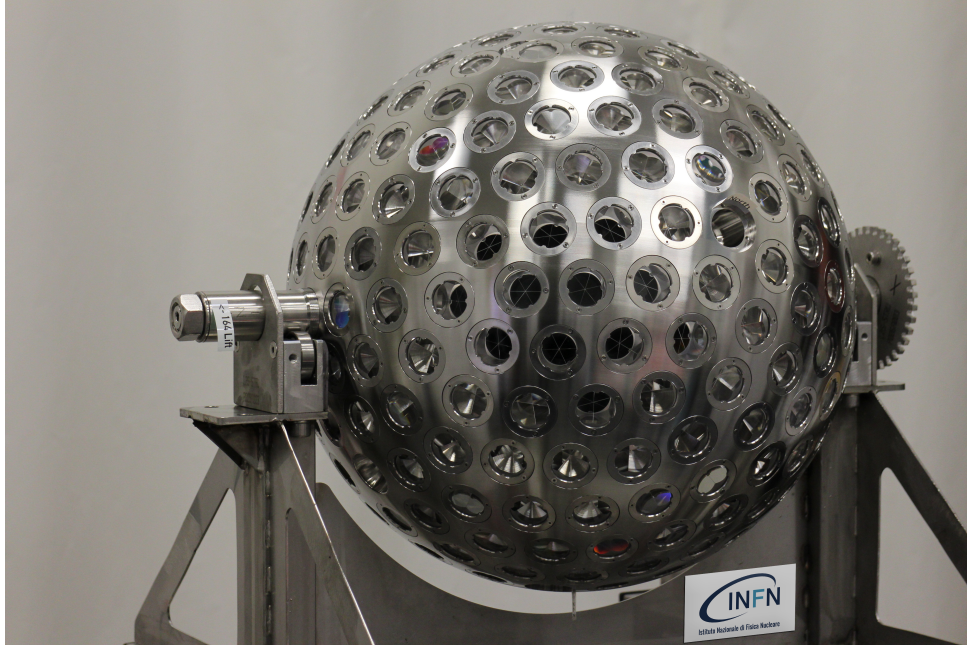


Figure 4.5: *LARES-2*. Credits: *SCF_Lab group (INFN - LNF)*.

can be expressed in zonal spherical harmonics [125, 126],

$$U = \frac{M}{r} \left[1 - \sum_{n=2}^{\infty} J_n \left(\frac{R_E}{r} \right)^n P_n(\sin \theta) \right], \quad (4.9)$$

where R_E is the mean radius of the Earth, P_n the Legendre polynomial of degree n and argument $\sin \theta$, with θ the latitude, and J_n the gravitational field's zonal harmonic coefficients.

Assuming axial symmetry, the precession caused by the first two even terms⁸ of Eq. (4.9) is [127]

$$\begin{aligned} \dot{\Omega}_{\text{class}} = & -\frac{3}{2} \frac{2\pi}{P} \left(\frac{R_E}{a} \right)^2 \frac{\cos I}{(1-e^2)^2} \left\{ J_2 + \right. \\ & \left. + J_4 \left[\frac{5}{8} \left(\frac{R_E}{a} \right)^2 (7 \sin^2 I - 4) \frac{1 + \frac{3}{2}e^2}{(1-e^2)^2} \right] + \dots \right\} + \dots, \quad (4.10) \end{aligned}$$

⁸Remember that only the even terms contribute to the precession

where a is the orbit's major semiaxis, e is the eccentricity, I is the orbital inclination, P is the orbital period, and J_{2n} are the even zonal harmonic coefficients.

A satellite such as LAGEOS has $\dot{\Omega}_{\text{class}} \simeq 126^\circ/\text{year}$, compared to only $\dot{\Omega}_{\text{LT}} \simeq 31$ milliarcsec/year. As a result, the Lense-Thirring phenomenon cannot be observed. Consequently, LARES-2 was designed, which has similar dimensions to LAGEOS but has an additional inclination that causes its classical precession to be the same in magnitude but in the opposite direction. In contrast, the magnitude, and direction of the Lense-Thirring precession will be identical for both satellites. Thus, the Lense-Thirring effect will be quantifiable.

Concerning optics, let us compare the OCS plot and FFDP of a 25.4 mm uncoated CCR (Figs. 4.6 - 4.8) to those of a 38.1 mm uncoated CCR (Figs. 4.9 - 4.11), both under the following conditions

- uncoated,
- null DAOs (perfect retroreflectors),
- linear polarization,
- 532 nm laser,
- normal incidence.

As expected from Eq. (4.2), the central peak intensity is greater for a CCR with a larger diameter. However, in the case of LARES-2, the first local minimum shifts closer to $35 \mu\text{rad}$, which is the VA value of both satellites, see Eq. (2.83). This is critical as we require a return of light also and above all around the VA value since the station experienced an angular displacement of $35 \mu\text{rad}$ relative to the satellite's position during the laser's trip.

In addition to the optical analysis, thermal analysis is required⁹. Thermal gradients within a CCR are generally dependent on the average free path of the light rays: the smaller the dimensions, the less thermal degradation occurs. However, it is necessary to consider the orbit into which the satellite carrying the CCR is launched, since overheating effects may occur if the retroreflector's dimensions are too small.

⁹Thermal simulations are available at the SCF_Lab group. It is not a subject of analysis in this thesis.

In conclusion, optimization is required from both an optical and thermal standpoint. The comprehensive analysis revealed that the 25.4 mm CCRs outperform the 38.1 mm CCRs for this specific mission.

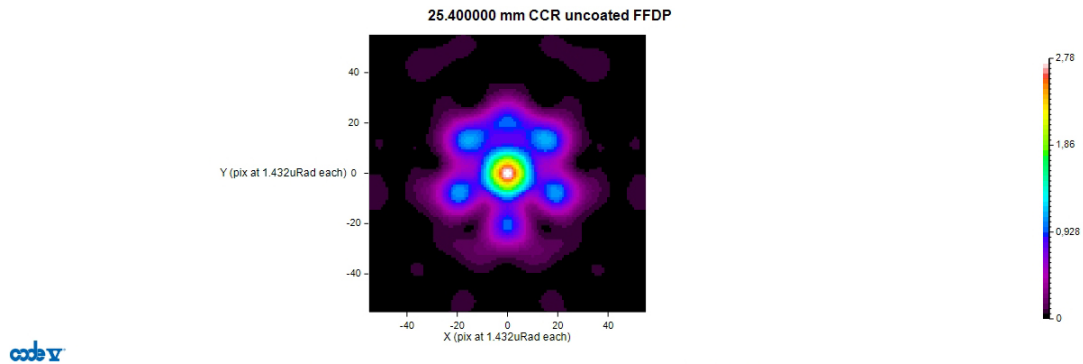
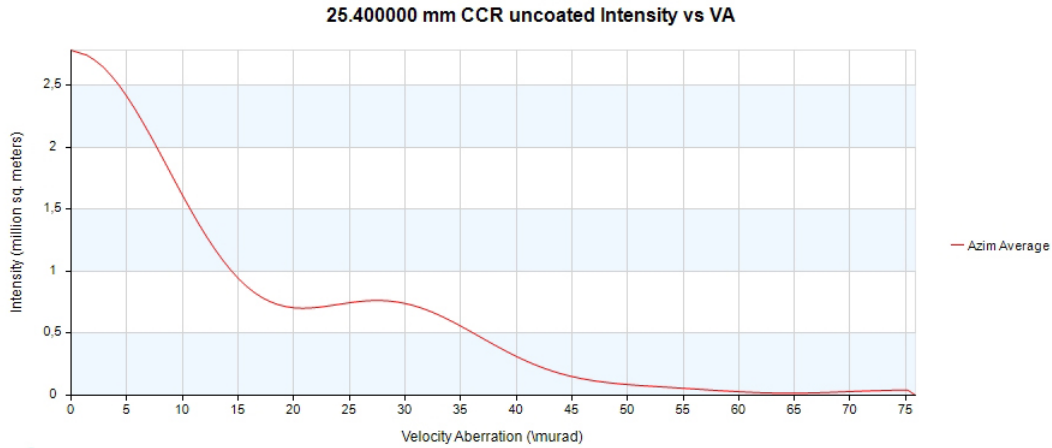
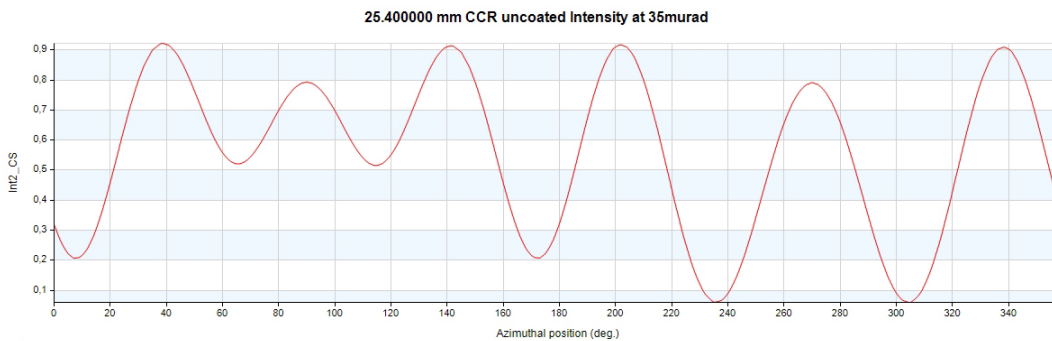


Figure 4.6: *LARES-2*. The FFDP of an uncoated 25.4 mm CCR with null DAOs shows a central lobe with the six lateral ones of lower intensity. The peak intensity turns out to be at 2.78 msm, in perfect agreement with the theoretical expected value of 2.79 msm predicted by Eq. (4.2).



code v

Figure 4.7: *LARES-2. Intensity vs VA plot. Besides the central peak intensity, we see a first minimum (the first dark ring in the diffraction pattern) nearby to $20 \mu\text{rad}$. Additionally, there is a first local maximum at $30 \mu\text{rad}$, that is, at a value close to the VA. In particular, for $\text{VA} = 35 \mu\text{rad}$, the intensity is $\sim 0.56 \text{ msm}$.*



code v

Figure 4.8: *LARES-2. Intensity at VA plot. This is the section of the FFDP that corresponds to $\text{VA} = 35 \mu\text{rad}$. Therefore, we can observe how the intensity changes as the azimuth angle θ varies in the interval $[0, 2\pi]$, when $\text{VA} = 35 \mu\text{rad}$.*

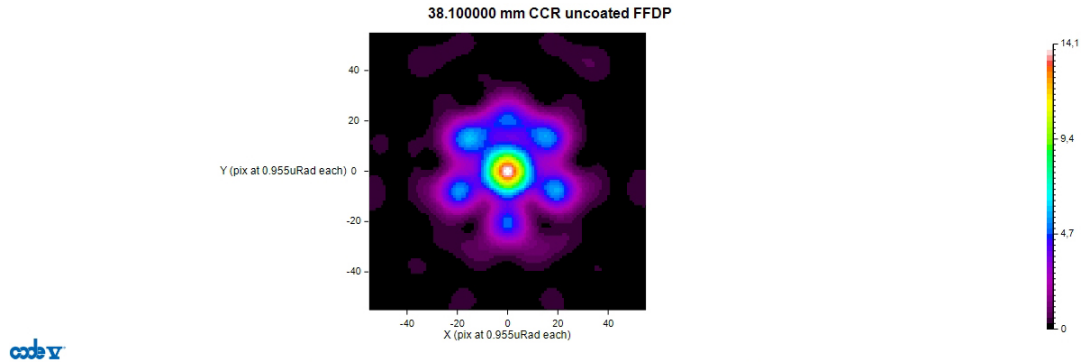


Figure 4.9: *LAGEOS/LARES*. The FFDP of an uncoated 38.1 mm CCR with null DAOs shows a central lobe with the six lateral ones of lower intensity. The peak intensity turns out to be at 14.1 msm, in perfect agreement with the theoretical expected value of 14.2 msm predicted by Eq. (4.2).

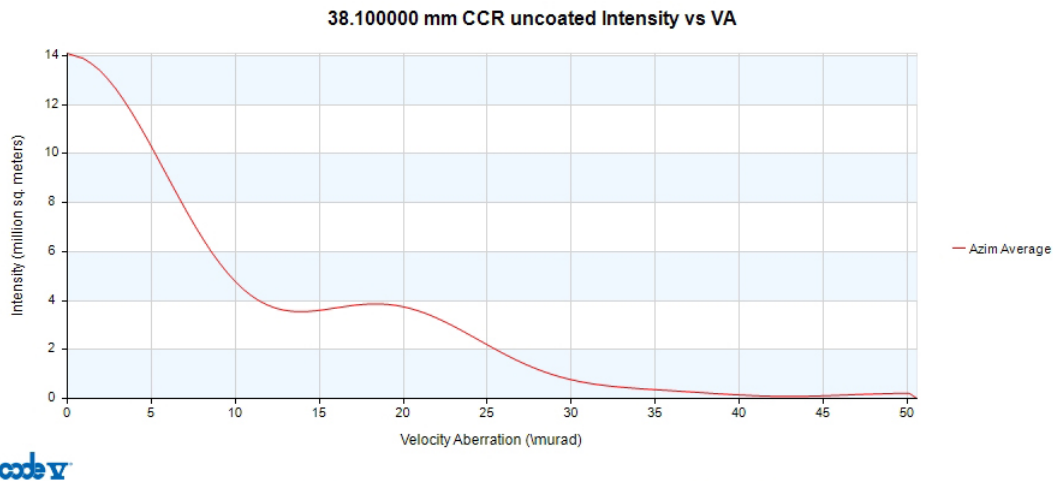


Figure 4.10: *LAGEOS/LARES*. Intensity vs VA plot. Besides the central peak intensity, we see a first minimum (the first dark ring in the diffraction pattern) nearby to 14 μrad . Additionally, there is a first local maximum at 27.5 μrad . In particular, for VA = 35 μrad , the intensity is ~ 0.29 msm.

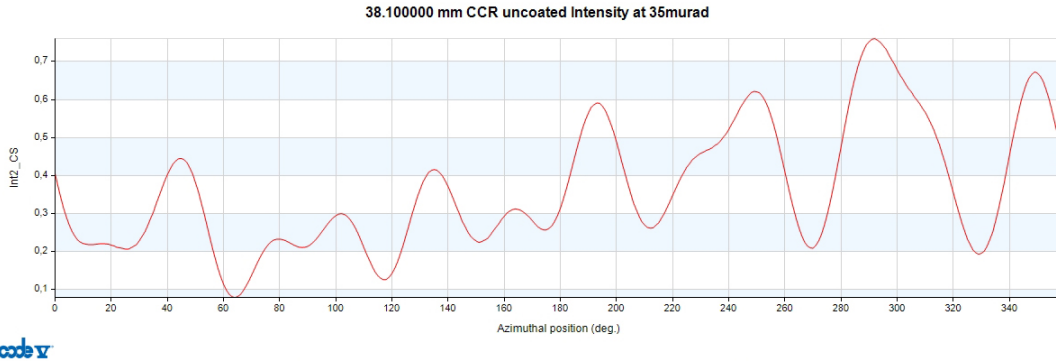


Figure 4.11: *LAGEOS/LARES. Intensity at VA plot. This is the section of the FFDP that corresponds to $VA = 35 \mu\text{rad}$. Therefore, we can observe how the intensity changes as the azimuth angle θ varies in the interval $[0, 2\pi]$, when $VA = 35 \mu\text{rad}$.*

4.3.2 MoonLIGHT

Since 1969, when the first Apollo mission was launched, LLR has been used to determine the distance between an Earth-based laser station and the lunar surface [128]. With laser tracking of the Moon, it is possible to investigate the dynamics of the Earth-Moon system, gravitational physics, geodesy, and the lunar interior. The early experiments used CCRs mounted on LRAs. Currently, there are five of them on the lunar surface: Apollo 11, Apollo 14, Apollo 15, Luna 17, and Luna 21. The first two are made up of 100 CCRs with a 38 mm diameter. Apollo 15 array is larger than the previous ones; it is hexagonal in shape and contains 300 CCRs with a diameter of 38 mm. Due to its dimensions, it is primarily used for LLR measurements. Finally, the two Lunokhod rovers were equipped with small arrays consisting of 14 CCRs organized in a triangular configuration.

As stated in Sec. 4.1, the first issue that must be addressed when conducting these types of measurements is the requirement for a collimated laser beam. Indeed, the atmosphere's turbulence distorts the beam (see Fig. 4.2), resulting in a divergence of about 1 arcsec. On the Moon, since 1 arcsec corresponds to 1.8 km, it has a diameter of about 2 km. The reflected laser, in turn, exhibits a divergence (for Apollo CCRs it is of about 8 arcsec). Thus, the beam's diameter when it reaches the Earth station is approximately 15 km.

Another issue with Apollo arrays is that they are subject to longitudinal lunar librations. During the lunar phase (27 days), the Moon rotates at a slower or faster rate than its orbital motion, depending on whether it is at perigee or apogee, revealing up to 8 degrees of longitude on the opposite side, eastern or western. As a result of this phenomenon, the Apollo arrays are moved so that a corner is several centimeters away from the opposite one, increasing the size of the pulse returning to Earth. The pulse's expansion will be proportional to the array's physical size and to the increase in the Moon - Earth distance (in the position where the libration phenomena are at their maximum). Consequently, the precision of distance measurements cannot be less than a few centimeters (for a single normal point).

To solve these problems, a new CCR was developed whose performance is unaffected by either the lunar librations or the regolith's motion. The SCF_Lab's collaboration with the University of Maryland resulted in the idea of replacing arrays made up of numerous small CCRs with a series of single larger CCRs having a diameter of 100 mm and positioned separately on the lunar surface [129, 130]. MoonLIGHT (Moon Laser Instrumentation for General Relativity High Accuracy Tests) CCR has the same design as the Apollo cubes (circular front face) but is larger in diameter.

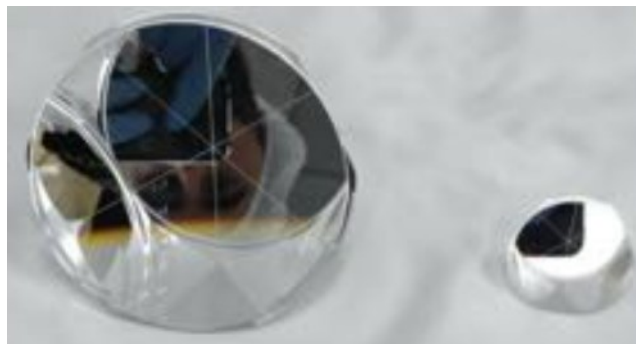


Figure 4.12: *Comparison between MoonLIGHT CCR (on the left) and Apollo CCR (on the right). Credits: SCF_Lab group (INFN - LNF).*

Instead of a single pulse, several short pulses returned with the same dimensions as the incident ones, achieving an accuracy of tens of microns (see Fig. 4.13): the objective is to have a retroreflector with the same optical response as half of the Apollo 15 array.

Each MoonLIGHT CCR is integrated into a protective case. The first model

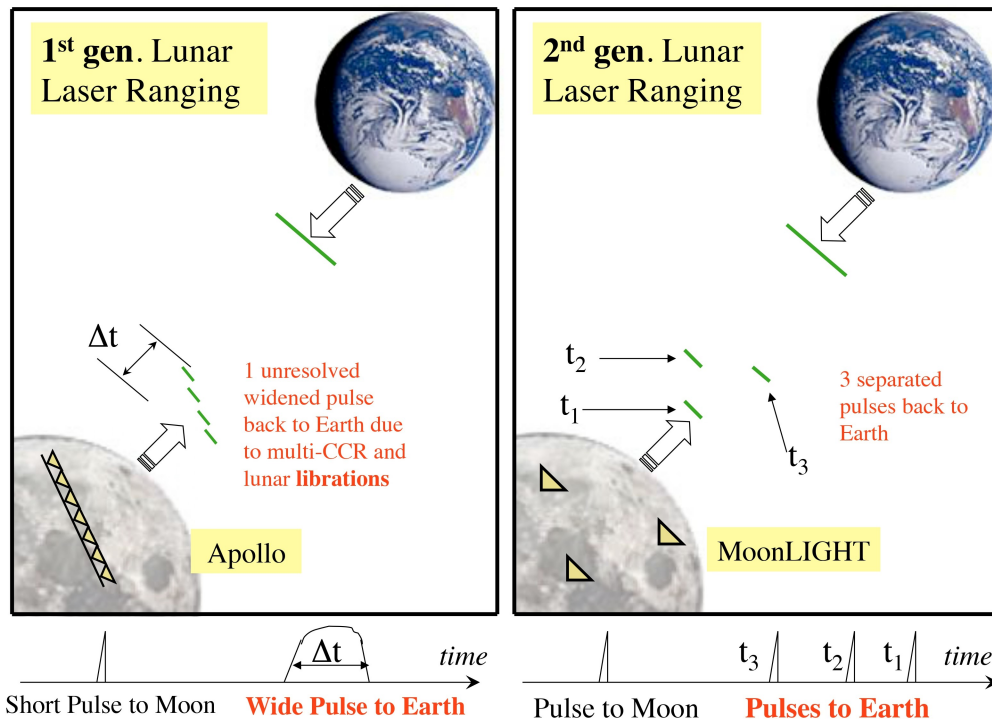


Figure 4.13: Diagram of the operation laser pulses return towards Earth station for the 1st generation LLR (Apollo), on the left, and for the 2nd generation LLR (MoonLIGHT), on the right. Credits: SCF_Lab group (INFN - LNF).

designed is that of “fixed pointing”. A metal case encloses the CCR with the central face facing the Earth. The structure is attached to the host lander. The position of the CCR relative to the expected average flatness of the local landing site is fixed before the launch and cannot be changed. This method, however, is only effective if the landing is very accurate, which is rather unlikely. Therefore, this method is highly dependent on the landing accuracy. Due to the difficulty of landing with high precision, the SCF_Lab group and ESA (European Space Agency) are developing and building MPac (MoonLIGHT Pointing actuator). An electronic system controls the movement of the structure in this new model of the CCR cover. Thus, the retroreflector pointing is adjusted appropriately each time based on the position of the CCR central face relative to the Earth.

MoonLIGHT CCRs, like for LARES-2, are subjected to laboratory tests and optical simulations before being launched into orbit. As is usual, simulations are performed with Code V and every macro’s run generates the FFDP and OCS plots. The simulated results for a 100 mm diameter uncoated CCR with null DAOs, 532 nm laser with linear polarization, and normal incidence are shown in Figs. 4.14 - 4.16. Let us observe that, according to Eq. (2.83), $VA = 4.3 \mu\text{rad}$ in the case of the Earth-Moon system.

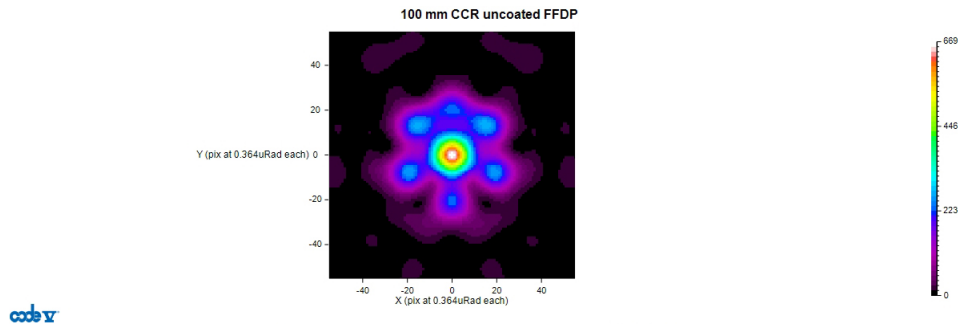
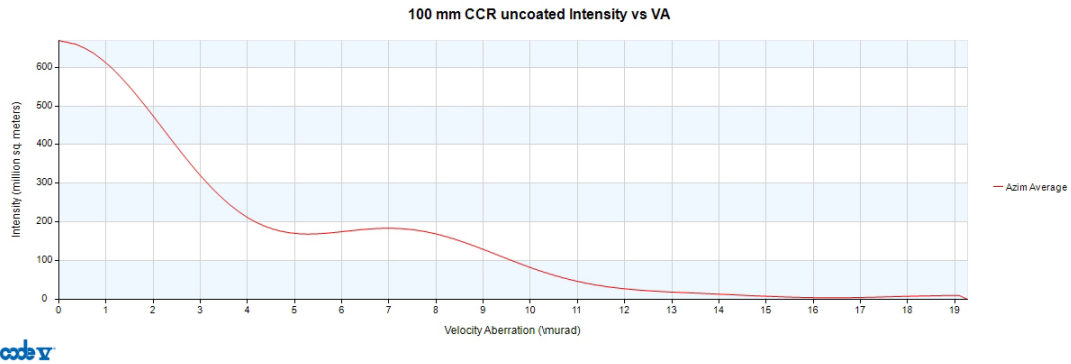
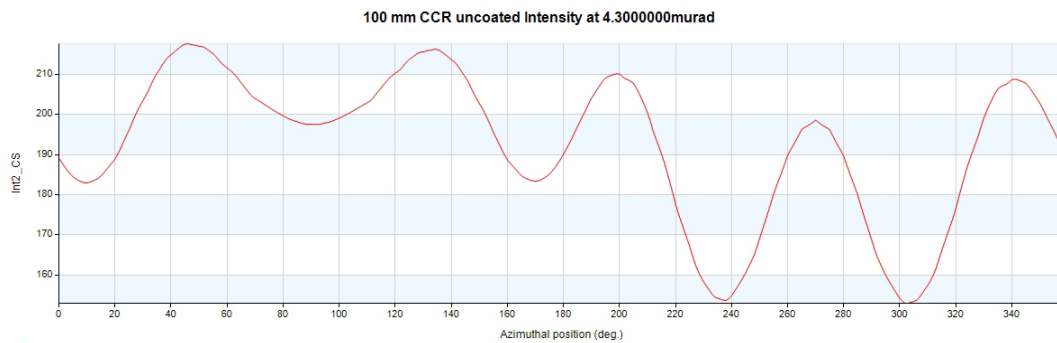


Figure 4.14: *The FFDP of an uncoated 100 mm CCR with null DAOs shows a central lobe with the six lateral ones of lower intensity. The peak intensity turns out to be at 669 msm, in agreement with the theoretical expected value of 672 msm predicted by Eq. (4.2).*



code v

Figure 4.15: *Intensity vs VA plot. Besides the central peak intensity, we see a first local maximum at $7.2 \mu\text{rad}$. In particular, for $VA = 4.3 \mu\text{rad}$, the intensity is $\sim 191 \text{ msm}$.*



code v

Figure 4.16: *Intensity at VA plot. This is the section of the FFDP that corresponds to $VA = 4.3 \mu\text{rad}$. Therefore, we can observe how the intensity changes as the azimuth angle θ varies in the interval $[0, 2\pi]$, when $VA = 4.3 \mu\text{rad}$.*

4.4 Planetary Ephemeris Program

PEP is a software developed by I. Shapiro in the 1960s at the Harvard’s Center for Astrophysics (CfA). Originally designed to generate lunar ephemerids, it was shortly after used for other applications, including comparing GR predictions to observations and predicting the variability of the gravitational constant in the weak field regime.

4.4.1 Installation and Big Test

PEP is written in FORTRAN programming language and can be installed on any POSIX-compliant operating system (such as UNIX, Linux, macOS). To install PEP, we need to download a package of files and copy these files into a new directory called *peptop*. Following that, we create the *bin* directory outside of *peptop*, which will contain the executable files (or links to them). At this point, we execute a series of instructions well reported in Ref [131]. We then proceed with the code setting to ensure that the installation was successful. This setting is accomplished through a procedure known as “Big Test”. This can be achieved using the commands

```
make bigtest
./bigtest
```

After that, we move to the *bigtest* directory and run

```
ls -ln*.verout.
```

This command checks that all files with the extension *.verout* have a size that is compatible with the minimum allowed, which is 1116 bytes [131].

4.4.2 PEP operational method

PEP already contains a set of GR mathematical models for the Solar System, each with its own set of free parameters that can be constrained through the experimental data.

We are particularly interested in using PEP to estimate the parameters achievable via the LR. Since the Cassini spacecraft has already provided an estimate of γ [132], we are only concerned with the β PPN parameter.

Furthermore, we focus on the LLR because it is the only mission for which data is currently available among the LR missions.

To compute the observables, PEP

- integrates and solves the equations of motion to determine position and velocity of the Sun, planets, and the Earth-Moon system barycenter;
- determines the displacement of the lunar reflector relative to the Moon's center of mass;
- determines the ranging station's displacement relative to the Earth's center of mass.

Moreover, PEP calculates all these quantities in the Solar System Barycenter, chosen as the reference frame by the software itself.

These estimates are based on data provided as *normal points*¹⁰. A normal point (NP) is an alphanumeric string that contains information such as

- date (day, month, year, hour, minute, and second);
- ToF (in 10^{-13} s);
- ToF error (in ps);
- array (Apollo 11, Apollo 14, Apollo 15, Luna 1, Luna 2);
- LR station;
- number of photons;
- laser wavelength.

Each run of PEP generates three upper bounds for the β parameter, which are inherent to the maximum sensitivity that the software can determine¹¹.

These bounds values are conventionally denoted by δ_1 , δ_2 , and δ_3 .

δ_1 is the sensitivity of the first convergent systematic run after the Big Test.

δ_2 takes the results of the first simulation and improves them and, finally, δ_3

takes the results of the second simulation and improves them again.

We calculate the mean value, the standard deviation, the maximum value,

¹⁰In the standard version provided by Nasa JPL.

¹¹PEP does not yet provide the mean values.

the minimum value, and the normal error for these bounds. The mean value μ_i of δ_i for β is given by

$$\mu_i = \frac{1}{N} \sum_{j=1}^N \delta_{ij}, \quad (4.11)$$

where N denotes the total number of available data for each run, while δ_{ij} are the values of δ_i ($i = 1, 2, 3$) obtained for each run $j = 1, \dots, N$. After calculating the mean value, we can determine the standard deviation σ_i

$$\sigma_i = \sqrt{\frac{\sum_{j=1}^N (\delta_{ij} - \mu)^2}{N}}. \quad (4.12)$$

As a result, we calculate the normal error ϵ_i using

$$\epsilon_i = \sqrt{\frac{\sum_{j=1}^N (\delta_{ij} - \mu)^2}{N - 1}}. \quad (4.13)$$

In this case, $N - 1$ appears in the denominator, rather than N as in the standard deviation, because we cannot get an estimate from a sample with length $N = 1$ since it has no internal variation. The presence of $N - 1$ in the denominator reflects this impossibility, and thus we require at least $N = 2$ data for the equation to work correctly.

4.4.3 Results

In this section, we present the latest upper bounds that we have obtained for β . These were achieved through the data provided by the LLR Astronomical Observatories at McDonald, Haleakala, Grasse, Apollo, Wettzell, and Matera, see Fig 4.17. Most of this data spans the years 1969 to 2016; only a small part is dated until 2018, therefore not much significant in calculating the upper bounds. The final results are summarized in Tab. 4.2, where we report the mean value, the maximum value M , the minimum value m , the standard deviation, and the normal error for δ_1 , δ_2 , and δ_3 .

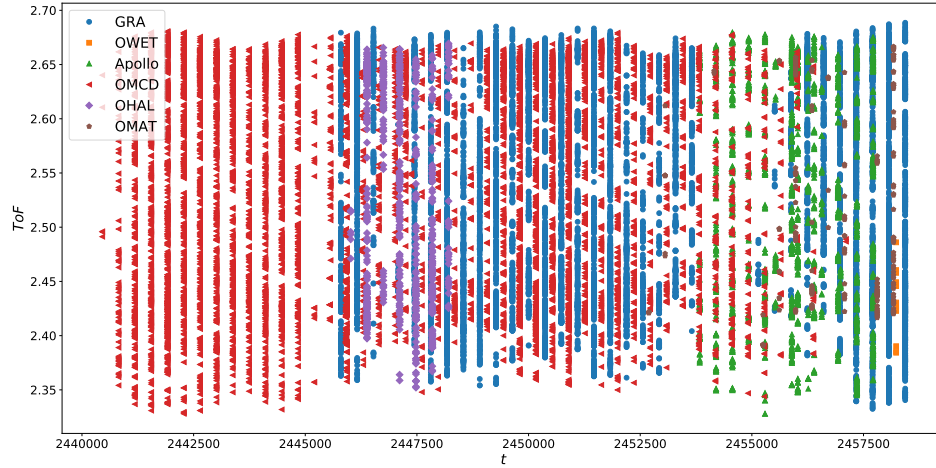


Figure 4.17: *LLR data from 1969 to 2018. The plot represents the ToF as a function of time. Here, ToF is expressed in units of 10^{-13} s, while time in Julian Date. Each marker denotes a distinct Astronomical Observatory from which data are collected.*

	δ_1	δ_2	δ_3
μ	$1.39 \cdot 10^{-5}$	$1.36 \cdot 10^{-5}$	$1.29 \cdot 10^{-5}$
σ	$1.63 \cdot 10^{-7}$	$4.23 \cdot 10^{-7}$	$5.93 \cdot 10^{-7}$
M	$1.42 \cdot 10^{-5}$	$1.41 \cdot 10^{-5}$	$1.40 \cdot 10^{-5}$
m	$1.37 \cdot 10^{-5}$	$1.30 \cdot 10^{-5}$	$1.21 \cdot 10^{-5}$
ϵ	$1.79 \cdot 10^{-7}$	$4.63 \cdot 10^{-7}$	$6.50 \cdot 10^{-7}$

Table 4.2: *Upper bounds δ_1 , δ_2 , and δ_3 for the β PPN parameter.*

Conclusions

A rigorous test of a gravitational theory requires the formulation of a theoretical framework, followed by the realization of experimental verification. For this reason, the thesis work has been divided mainly into two parts: the mathematical treatment of the physical phenomenon and the experimental setting. An accurate theoretical model must take into account that gravity manifests itself differently according to the gravitational scales. Therefore, to provide an adequate phenomenological examination, we divided the theoretical treatment into three chapters, each of which proposes tests suitable for distinct regimes.

The first concerns low gravity. This is undoubtedly the most explored regime, given that the earliest proofs of the GR's validity came from measurements within the Solar System. Not only that but most of the satellites orbiting the Earth were designed with the primary goal of measuring frame-dragging, one of Einstein's predicted effects. Nevertheless, so far only GR was extensively tested in the weak field. Therefore, our aim is to begin studying weak effects even in alternative gravity theories. To do this, we reviewed the PPN formalism, which is the most suitable in the description of low gravity, and applied it to a number of alternative metric theories. We started with Horndeski's theory, the most general extension of GR with scalar fields and second-order equations. Indeed, the scalar-tensor theory, as well as the Brans-Dicke and $f(R)$ theories, can be reproduced from it. The PPN formalism of vector tensor theories was also studied after that. Then, we determined the equations of motion for these new theoretical models in the PPN formalism using Will's rules. This is an important step in the testing process because most of the software used to analyze data from the Solar System's space missions, including PEP, is based on integrations of the equations of motion. Finally, for each of the different (non-vector) theories presented, we estimated the Lense-Thirring precession in order to take advantage of the already planned

space missions. This framework is only appropriate for the weak field. The goal, however, should be to find a theory that can be used on any scale. Thus, in the second chapter of the thesis, we suggest a test that is applicable in three different gravity regimes: low, intermediate, and high. We evaluated the red and blue shifts for distinct astrophysical and cosmological sources. Specifically, we characterized two spacetimes, the first inspired by astrophysical configuration, exploring the consequences of the Zipoy-Voorhees metric on NS and WD. The second based on cosmological consideration, using the Schwarzschild-de Sitter spacetime. By varying the free parameters that enter the two metrics, we got feasible red and blue shift intervals and interpreted our expectations in view of current experiments and limits. The Zipoy-Voorhees metric, used to characterize NS and WD, showed that at the level of Solar System, the δ free term is unbounded. Analogously, the Schwarzschild-de Sitter solution, where we fixed the Λ Planck's value, indicated that general relativistic effects are clearly disfavored. In fact, even the Λ value predicted by the Planck satellite cannot fully reproduce the expected intervals of $z_{1,2\pm}$ that LR experiments estimate. On the other side, bearing in mind the maximally - rotating configurations for NS and WD, we got suitable red and blue shift intervals. We therefore concluded the most suitable approximations for NS and WD objects could be performed involving high quadrupole moments. The same happened for the cosmological constant, besides the Solar System regime, showing a good agreement with current bounds and indicating the goodness of Planck Λ measurements. Moreover, possible experimental designs for improving the quality of our results have been naively proposed. We discussed coarse - grained approaches to build up likely experimental configurations and setups with the aim of refining the current accuracy over the red and blue shift. To this end, we propose to adopt the binary system composed by Mars-Phobos to improve $z_{1,2\pm}$ measurements using the satellite LR technique. As red and blue shifts can be used to test the equivalence principle and/or sometimes to check the validity of particular classes of models, we intend to contrive new experiments that will be able to construct bounds over Λ , instead of postulating it. In so doing, as perspective we expect to work out a back - scattering procedure, different from the one here developed.

In the third chapter, we focused on the high gravity regime, examining worm-holes, one of the most intriguing structures in the Universe. It is a theoretical model that enables us to investigate the properties of alternative theories of gravity in the strong field.

We here considered the class of $f(R)$ theories. Postulating a generic power-law form $f(R) = f_0 R^{1+\epsilon}$, we investigated two possible approaches to characterize the shape function and in particular the ratio $b(r)/r$. The first attempt was a phenomenological inverse power law, recovered from widely-investigated approaches in the literature. The second has been proposed considering the numerical pathology of the ratio $b(r)/r$ within the throat. We thus introduced the use of Padé approximant to characterize the shape function in a model-independent way. Our strategy to decide the Padé orders was straightforward: we singled out the simplest approximant that resembles a first order Taylor expansion. To do so, we encountered two possibilities, i.e. the (1,0) and (0,1) expansions. The first coincides with pure Taylor expansion and was unable to guarantee that $b \rightarrow 0$ as $r \rightarrow \infty$. The second possibility, namely (0,1), fulfilled our requirement. Thus, we worked out the wormhole solution under this ansatz, adding the additional requirement of stable geometrical fluids, whose perturbations are negligible inside the throat. To do so, we employed the sound speed to vanish in analogy to cosmological contexts in which the sound speed is associated to the fluid evolution for a given system. Finally, we constrained the set of coefficients (β, ϵ, r_0) . We noticed that in all the analyzed cases as GR is recovered, exotic matter is still needed as expected. Future works will extend such a scenario. In particular, we will wonder whether extended versions of Padé approximants can be used to characterize the shape function. We will therefore show what would happen by changing the background theory of gravity, involving different paradigms with respect to the $f(R)$ case. In particular, we would like to extend this analysis to the Horndeski model, which we have only looked at so far in the weak field. In this way, we might be able to find the theory's constraints in both low and high gravity.

The concluding chapter of the thesis is dedicated to the experimental method. We concentrated on LR, which has been used for years to estimate the parameters characterizing the theoretical models of the weak field. Before launching a space mission, it is crucial to conduct a series of tests to ensure its success; one of these concerns the optical component of the experiment, namely the CCR. In particular, we attempt to understand what a CCR's light return will be once in orbit by running optical simulations with the Code V software. To get a survey that is as broad as possible and representative of real conditions, we generally investigate several situations. However, here, we have shown just the simulations of the CCRs employed in the two space missions on which we are currently working with the SCF Lab group in Frascati.

We are talking about perfect uncoated CCRs (null DAOs), with a normal incidence of the laser beam (at 532 nm, since this is the most often utilized wavelength by Earth stations) and linear polarization. Other optical simulations, which take into account non-zero DAOs, non-normal incidence, lasers with different wavelength values, circular polarization, and coatings, are available at the SCF Lab group. We have been working on improving the code in recent years, and it now allows us to get accurate results that match the theoretical values. We are now extending the code in order to simulate a CCRs array, as LARES-2. Finally, we presented the PEP software results in analyzing LR data from several ground stations. Our future work will first be to improve the FORTRAN code to ensure the accuracy of these results. Furthermore, we would like to modify it to include the equations of motion of the alternative metric theories of gravity, calculated in the previous sections. This would be an important step in testing gravitational models beyond GR in the Solar System's context, i.e. in the weak field.

In the meantime, we look forward to the launch of LARES-2, which will presumably take place in the spring of 2022, and that of MoonLIGHT scheduled for 2024. Not by chance, when he landed on the Moon, Neil Armstrong said *“that’s one small step for [a] man, but a giant leap for mankind”*.

Bibliography

- [1] A. Einstein, Sitzung. der Preuss. Ak. der Wissens., 844-847 (1915).
- [2] A. Einstein, Ann. der Phys. **354** (7), 769-822 (1916).
- [3] F. W. Dyson, A. S. Eddington, C. Davidson, Phil. Trans. R. Soc. Ser. **220** A, 291-330 (1920).
- [4] R. V. Pound, G. A. Rebka Jr, Phys. Rev. Lett. **3** (9), 439–441 (1959).
- [5] R. V. Pound, G. A. Rebka Jr, Phys. Rev. Lett. **4** (7), 337–341 (1960).
- [6] R. V. Pound, J. L. Snider, Phys. Rev. Lett. **13** (18), 539–540 (1964).
- [7] I. I. Shapiro, Phys. Rev. Lett. **13** (26), 789–791 (1964).
- [8] I. I. Shapiro et al., Phys. Rev. Lett. **20** (22), 1265–1269 (1968).
- [9] B. P. Abbott et al., Phys. Rev. Lett. **116** (6), 061102 (2016).
- [10] S. Perlmutter et al. [SNCP Collaboration], Astrophys. J. **517**, 565 (1999); A. G. Riess et al. [Supernova Search Team Collaboration], Astron. J. **116**, 1009 (1998).
- [11] D. N. Spergel et al. [WMAP Collaboration], Astrophys. J. Suppl. **148**, 175 (2003); Astrophys. J. Suppl. **170**, 377 (2007).
- [12] E. Komatsu et al. [WMAP Collaboration], Astrophys. J. Suppl. **180**, 330 (2009).
- [13] E. Komatsu et al. [WMAP Collaboration], Astrophys. J. Suppl. **192**, 18 (2011).

-
- [14] M. Tegmark et al. [SDSS Collaboration], Phys. Rev. D **69**, 103501 (2004); U. Seljak et al. [SDSS Collaboration], Phys. Rev. D **71**, 103515 (2005).
- [15] D. J. Eisenstein et al. [SDSS Collaboration], Astrophys. J. **633**, 560 (2005).
- [16] B. Jain, A. Taylor, Phys. Rev. Lett. **91**, 141302 (2003).
- [17] S. Weinberg, Rev. Mod. Phys. **61**, 1 (1989).
- [18] Planck Collaboration, A&A **594**, A13 (2016).
- [19] E. J. Copeland, M. Sami, S. Tsujikawa, Int. J. Mod. Phys. D **15**, 1753-1936 (2006).
- [20] C. Kiefer, Annal. Phys., **15**, 129 (2005).
- [21] M. Albers, C. Kiefer, M. Reginatto, Phys. Rev. D, **78**, 064051 (2008).
- [22] D. Giulini, C. Kiefer, Lect. Notes Phys., **721**, 131 (2007).
- [23] D. N. Page, C. D. Geilker, Phys. Rev. Lett., **47**, 979 (1981).
- [24] B. Schulz, *Review on the quantization of gravity*, ArXiv[gr-qc]: 1409.7977 (2014).
- [25] G. Calcagni, *Quantum gravity and gravitational-wave astronomy*, ArXiv[gr-qc]: 2012.08251 (2020).
- [26] S. Carlip, Class. Quant. Grav., **25**, 154010 (2008).
- [27] S. Capozziello, M. De Laurentis, Phys. Rept. **509**, 167 (2011).
- [28] K. Bamba, S. Capozziello, S. Nojiri, S. O. Odintsov, Astrophys. Space Sci. **342**, 155 (2012).
- [29] S. Nojiri, S. D. Odintsov, V. K. Oikonomou, Phys. Rept. **692**, 1 (2017).
- [30] T. P. Sotiriou, V. Faraoni, S. Liberati, Int. J. Mod. Phys. D **17**, 399-423 (2008).
- [31] S. Capozziello, V. F. Cardone, A. Troisi, Mon. Not. Roy. Astron. Soc. **375**, 1423-1440 (2007).

-
- [32] G. J. Olmo, *Int. J. Mod. Phys. D* **20**, 413-462 (2011).
- [33] C. W. Misner, K. S. Thorne, Wheeler J. A., *Gravitation* (Princeton University Press, 2017).
- [34] U. Le Verrier, *C. R. Acad. Sci.* **49**, 379–383 (1859).
- [35] C. M. Will, *Liv. Rev. Relativ.* **17**, 4 (2014).
- [36] R. M. Wald, *General Relativity*, (The University of Chicago Press, 1984).
- [37] F. W. Dyson, A. S. Eddington, C. Davidson, *Phil. Trans. R. Soc. Lond.* **220A**, 291-333 (1920).
- [38] H. C. Ohanian, R. Ruffini, *Gravitation and Spacetime* (Cambridge University Press, 3rd ed., 2013).
- [39] S. Weinberg, *Gravitation and Cosmology: Principles and Applications of the General Theory of Relativity* (John Wiley & Sons, Inc. 1972), pp. 688.
- [40] J. D. Toniato, D. C. Rodrigues, Á. O. F. de Almeida, N. Bertini, *Phys. Rev. D* **96**, 064034 (2017).
- [41] J. D. Toniato, D. C. Rodrigues, A. Wojnar, *Phys. Rev. D* **101**, 064050 (2020).
- [42] C. M. Will, *Theory and Experiment in Gravitational Physics* (Cambridge University Press, 2018), pp. 380.
- [43] S. Chandrasekhar, *Astrophys. J.* **142**, 1488 (1965).
- [44] B. Altschul et al, *Adv. Space Res.* **55**, 501-524 (2015).
- [45] M. Hohmann, *Phys. Rev. D* **92**, 064019 (2015).
- [46] T. Kobayashi, M. Yamaguchi, J. Yokoyama, *Prog. Theor. Phys.* **126**, 511-529 (2011).
- [47] S. Capozziello, M. De Laurentis, *Phys.Rept.* **509**, 167-321 (2011).
- [48] S. Capozziello, V.F. Cardone, A. Troisi, *JCAP* 0608 (2006) 001.

-
- [49] S. Capozziello, R. D'Agostino, O. Luongo, *Int. J. Mod. Phys. D* **28**, 101930016 (2019).
- [50] T. P. Sotiriou, V. Faraoni, *Rev. Mod. Phys.* **82**, 451-497 (2010).
- [51] I. L. Buchbinder, S. D. Odintsov, I. Shapiro, *Effective Action in Quantum Gravity* (IOP Publishing, Bristol, 1992).
- [52] A. A. Starobinsky, *Phys. Lett. B* **91**, 99 (1980).
- [53] T. P. Sotiriou, V. Faraoni, S. Liberati, *Int. J. Mod. Phys. D* **17**, 399 (2008).
- [54] A. De Felice, S. Tsujikawa, *Liv.Rev. Rel.* **13**, 3 (2010).
- [55] S. Capozziello, *Int. J. Mod. Phys. D* **11**, 483 (2002).
- [56] S. Capozziello, A. Stabile, A. Troisi, *Class. Quantum Grav.* **25**, 085004 (2008).
- [57] S. Capozziello, A. Troisi, *Phys. Rev. D* **72**, 044022 (2005).
- [58] S. Capozziello, C.A. Mantica, L. G. Molinari, *Int. J. Geom. Meth. Mod. Phys.* **16**, 1950008 (2018).
- [59] S. Capozziello, C.A. Mantica, L. G. Molinari, *Gen. Rel. Grav.* **52**, 36 (2020).
- [60] S. Capozziello, A. Stabile, A. Troisi, *Mod. Phys. Lett. A* **21**, 2291-2301 (2006).
- [61] R. Ruffini, C. Sigismondi, *Nonlinear Gravitodynamics: the Lense-Thirring Effect* (World Scientific Publishing Company, 2003).
- [62] I. Ciufolini, R. Matzner, V. Gurzadyan, R. Penrose, *Eur. Phys. J. C* **77**, 819 (2017).
- [63] T. B. Bahder, *Phys. Rev. D* **68**, 063005 (2003); L. Buoninfante, G. Lambiase, A. Stabile, *Eur. Phys. Jour. C* **80**, 122 (2020); M. Caputo, *The Gravity Field of the Earth* (Academic Press, N. Y., 1967); N. Ashby, J. J. Spilker, *Introduction to Relativistic Effects on the Global Positioning System, in Global Positioning System: Theory and Applications*, B. W.

- Parkinson and J. J. Spilker, eds., vol. I and II (P. Zarchan, editor-in-chief), Progress in Astronautics and Aeronautics, vol. 163 and 164 (Amer. Inst. Aero. Astro., Washington, D.C., 1996).
- [64] A. Herrera - Aguilar, U. Nucamendi, Phys. Rev. D **92**, 045024 (2015).
- [65] R. Becerril, S. Valdez-Alvarado, U. Nucamendi, Phys. Rev. D **94**, 124024 (2016).
- [66] D. C. Wilkins, Phys. Rev. D **5**, 814 (1972).
- [67] J. M. Bardeen, Press W. H., Teukolsky S. A., Astrophys. J. **178**, 347 (1972).
- [68] U. Nucamendi, M. Salgado, D. Sudarsky, Phys. Rev. D, **63**, 125016 (2001).
- [69] G. Lukes-Gerakopoulos, Phys. Rev. D. **86**, 044013 (2012).
- [70] J.A. Arrieta-Villamizar, J.M. Velasquez-Cadavid, O.M. Pimentel, F.D. Lora-Clavijo, A.C. Gutiérrez-Pineros, Class. Quant. Grav., **38** 1, 015008 (2021).
- [71] O. Luongo, H. Quevedo, Phys. Rev. D **90**, 084032 (2014); O. Luongo, H. Quevedo, *Toward an invariant definition of repulsive gravity*, Contribution to: MG 12, 1029-1031, ArXiv[gr-qc]: 1005.4532, (2010).
- [72] R. Giambò, O. Luongo, H. Quevedo, Phys. dark univ. **30**, 100721 (2020); O. Luongo, H. Quevedo, Found. Phys. **48**, 1, 17-26 (2018).
- [73] K. Boshkayev, O. Luongo, M. Muccino, Eur. Phys. Jour. C, **80**, 964 (2020).
- [74] I. Ciufolini et al, Eur. Phys. J. Plus **132**, 336 (2017); A. Paolozzi et al, Journ. of Geod. **93**, 2437-2446, (2019).
- [75] G. Allemandi, M. Francaviglia, M. L. Ruggiero, A. Tartaglia, Gen. Rel. Grav. **37**, 1891-1904 (2005).
- [76] V. Kagramanova, J. Kunz, C. Lämmerzahl, Phys. Lett. B **634**, 465-470 (2006).

- [77] G. Allemandi, M. L. Ruggiero, *Gen. Rel. Grav.* **39**, 1381 (2007).
- [78] P. L. Bender et al, *Science* **182**, 229-238 (1973).
- [79] J. G. Williams, S. G. Turyshev, D. H. Boggs, *Int. J. Mod. Phys. D* **18**, 1129-1175 (2009).
- [80] I. Ciufolini et al, *Eur. Phys. J. Plus* **126**, 72 (2011).
- [81] S. G. Turyshev et al, *Exp. Astron.* **28**, 209–249 (2010).
- [82] J. M. Lattimer, M. Prakash, *Phys. Rept.* **442**, 109-165 (2007).
- [83] J. B. Holberg, T. D. Oswalt, M. A. Barstow, *The Astron. Jour.* **143**, 68 (2012).
- [84] M. Visser, *Lorentzian wormholes: from Einstein to Hawking*. (AIP Press., 1996).
- [85] D. C. Dai, D. Stojkovic, *Phys. Rev. D* **100**, 083513 (2019).
- [86] J. Maldacena, L. Susskind, *Fortsch. Phys.* **61**, 781 (2013).
- [87] J. Gratus, P. Kinsler, M. W. McCall, *Found. Phys.* **49**, 330-350 (2019).
- [88] A. Ovgun, K. Jusufi, I. Sakalli, *Phys. Rev. D* **99**, 024042 (2019).
- [89] K. Jusufi, A. Ovgun, *Phys. Rev. D* **97**, 024042 (2018).
- [90] A. Einstein, N. Rosen, *Phys. Rev.* **48**, 73-77 (1935).
- [91] M. S. Morris, K. S. Thorne, *Am. J. Phys.* **56**, 395 (1987).
- [92] S. Capozziello, F. S. N. Lobo, J. P. Mimoso, *Phys. Rev. D* **91**, (2015).
- [93] M. Li, Li X.D., S. Wang, Y. Wang, *Front. Phys.* **8**, 828-846 (2013).
- [94] E. J. Copeland, M. Sami, S. Tsujikawa, *Int. J. Mod. Phys. D* **15**, 1753 (2006).
- [95] D. Hochberg, T. W. Kephart, *Phys. Rev. Lett.* **70**, 2665-2668 (1993).
- [96] K. Bamba, S. Capozziello, S. Nojiri, S. O. Odintsov, *Astrophys. Space Sci.* **342**, 155 (2012).

-
- [97] V. De Falco, E. Battista, S. Capozziello, M. De Laurentis, Phys. Rev. D **101**, 104037 (2020).
- [98] S. Capozziello, T. Harko, T. S. Koivisto, F. S. N. Lobo, G. J. Olmo, Phys. Rev. D **86**, 127504 (2012).
- [99] J. L. Rosa, J. P. S. Lemos, F. S. N. Lobo, Phys. Rev. D **98**, 064054 (2018).
- [100] C. Gruber, O. Luongo, Phys. Rev. D **89**, 103506 (2014).
- [101] H. Wei, X. P. Yan, Y. N. Zhou, J. Cosm. Astrop. Phys. **1401**, 045 (2014).
- [102] S. G. Krantz, H. R. Parks, *A primer of real analytic functions* (Birkhauser, 1992).
- [103] H. Padé, Ann. Sci. Ecole Norm. Sup. **9**, 3-93 (1982).
- [104] V. Nestoridis, J. of Contemp. Math. Anal. **47**, 168-181 (2012).
- [105] M. Della Morte et al., JHEP **1203**, 055 (2012).
- [106] A. V. Astashenok, S. Capozziello, S. D. Odintsov, V. K. Oikonomou, Phys. Lett. B **811**, 135910 (2020).
- [107] S. Capozziello, M. De Laurentis, R. Farinelli, S. D. Odintsov, Phys. Rev. D **93**, 023501 (2016).
- [108] D. Hochberg, M. Visser, Phys.Rev.D **58**, 044021 (1998).
- [109] M. S. Linton, A. Pourtsidou, R. Crittenden, R. Maartens, JCAP **04**, 043 (2018).
- [110] S. Capozziello, M. De Laurentis, O. Luongo, A. C. Ruggeri, Galaxies **1**, 216-260 (2013).
- [111] O. Luongo, M. Muccino, Phys. Rev. D **98**, 103520 (2018).
- [112] F. Hassani, B. L'Huillier, A. Shafieloo, M. Kunz, J. Adamek, JCAP **04**, 039 (2020).
- [113] M. Kunz, Phys.Rev.D **80**, 123001 (2009).

- [114] O. Luongo, H. Quevedo, *Int. J. Mod. Phys. D* **23**, 1450012 (2014).
- [115] K. Boshkayev, T. Konysbayev, E. Kurmanov, O. Luongo, M. Muccino, *Galaxies* **8**, 74 (2020).
- [116] S. Capozziello, P. Jovanovic, V. Borica Jovanovic, D. Borica, *JCAP* **1706**, 044 (2017).
- [117] S. Capozziello, P. Martin-Moruno, C. Rubano, *Phys. Lett. B* **664**, 12 (2008).
- S. Capozziello, R. D'Agostino, O. Luongo, *Gen. Rel. Grav.* **51** 1, 2 (2019).
- M. Calza, A. Casalino, O. Luongo, L. Sebastiani, *Eur. Phys. J. Plus* **135** 1, 1 (2020).
- [118] V. De Falco, E. Battista, S. Capozziello, M. De Laurentis, *Phys. Rev. D* **103**, 044007 (2021).
- [119] G. Galilei, *Dialogo sopra i due massimi sistemi del mondo*, (1632).
- [120] P. L. Bender et al, *Science* **182**, 4109 (1973).
- [121] D. Arnold, SAO Special Report **382**, (1979).
- [122] K. Crabtree, R. Chipman, *Appl. Opt.* **49**, 5882-5890 (2010).
- [123] J. J. Degnan, *A tutorial on Retroreflectors and Arrays for SLR*, ILRS workshop, (2012).
- [124] T. W. Murphy Jr., S. D. Goodrow, *Appl. Opt.* **52**, 117-126 (2013).
- [125] P. H. Nguyen, *Measuring frame-dragging with LARES, and other topics in gravity*, University of Texas at Austin, (2017).
- [126] D. G. King-Hele, C. J. Brookes, G. E. Cook, *Geophys. J. Int.* **64**, 3 – 30 (1981).
- [127] I. Ciufolini, *Phys. Rev. Lett.* **56**, 278 (1986).
- [128] S. Dell'Agnello et al., *Nucl. Instrum. and Meth. in Phys. Res. A* **692**, 275-279 (2012).

-
- [129] S. Dell’Agnello et al., *Journ. of Appl. Math. and Phys.* **3**, 218-227 (2015).
- [130] M. Martini et al, *Planet. Space Sci.* **74**, 276-282 (2012).
- [131] N. H. Johnson, *High-Precision Lunar Ranging and Gravitational Parameter Estimation With the Apache Point Observatory Lunar Laser-ranging Operation*, University of California San Diego (2015).
- [132] B. Bertotti, L. Iess, P. Tortora, *Nature* **425**, 374–376 (2003).